Real-time x-ray scattering studies on organic thin films

Dissertation

der Mathematisch-Naturwissenschaftlichen Fakultät

der Eberhard Karls Universität Tübingen

zur Erlangung des Grades eines

Doktors der Naturwissenschaften

(Dr. rer. nat.)

vorgelegt von

Christian Hermann Frank

aus Bad Mergentheim

Tübingen

2014

Tag der mündlichen Qualifikation:	20.11.2014
Dekan:	Prof. Dr. Wolfgang Rosenstiel
1. Berichterstatter:	Prof. Dr. Frank Schreiber
2. Berichterstatter:	Prof. Dr. Martin Oettel

Contents

1 Introduction **1**

2 Organic thin film growth **5**
2.1 Introduction to thin film growth . . . 5
2.2 Atomistic nucleation . . . 8
2.2.1 Atomistic, two dimensional nucleation . . . 10
2.2.2 Atomistic, three dimensional nucleation . . . 12

3 Materials **15**
3.1 Pentacene (PEN) . . . 15
3.2 Perfluoropentacene (PFP) . . . 17
3.3 Diindenoperylene (DIP) . . . 18
3.4 Buckminsterfullerene C_{60} (C_{60}) . . . 19

4 Methods **21**
4.1 Organic molecular beam deposition (OMBD) . . . 21
4.2 X-ray reflectivity (XRR) . . . 22
4.2.1 Dynamical theory . . . 23
4.2.2 Kinematical theory . . . 25
4.2.3 Characteristic shape of x-ray reflectivity curves . . . 26
4.3 Growth oscillations . . . 27
4.4 Grazing incidence small angle x-ray scattering (GISAXS) . . . 28
4.5 Grazing incidence diffraction (GID) . . . 31
4.6 Synchrotron radiation . . . 31
4.7 Detector specifications . . . 32
4.8 Atomic force microscopy (AFM) . . . 32

5 Results and discussion **35**
5.1 Real-time GID measurements on pristine PFP and PFP:PEN blends . . . 36
5.1.1 Growth conditions and sample preparation . . . 37

5.1.2 Calculation of the experimental resolution 37
5.1.3 Results and discussion of pure PFP thin films 39
5.1.3.1 Characterization of the morphology 40
5.1.3.2 Post-growth analysis of the molecular structure 43
5.1.3.3 Real-time analysis of the in-plane structure 45
5.1.4 Results and discussion of PFP:PEN blends 49
5.1.5 Summary and conclusion 51
5.2 Post-growth GISAXS measurements on pristine DIP 52
5.2.1 Growth conditions and sample preparation 53
5.2.2 Results and Discussion 54
5.2.2.1 Discussion of the reciprocal space maps 55
5.2.2.2 Modeling the GISAXS profiles 57
5.2.2.3 Discussion of the GISAXS profiles 59
5.2.2.4 Fitting the GISAXS profiles 61
5.2.3 Conclusion 65
5.3 Real-time GISAXS measurements on pristine DIP 66
5.3.1 Growth conditions and sample preparation 67
5.3.2 Results and discussion 68
5.3.2.1 Analysis of the out-of-plane structure 69
5.3.2.2 Analysis of the in-plane morphology 72
5.3.2.3 Estimation of effective activation energies 75
5.3.3 Summary and conclusion 76
5.4 GID-GISAXS measurements on DIP:C60 blends 77
5.4.1 Growth conditions and sample preparation 78
5.4.2 Results and Discussion 78
5.4.2.1 Post-growth analysis of the structure and morhology . . . 78
5.4.2.2 Real-time analysis of the in-plane structure 81
5.4.3 Summary and Conclusion 85

6 Summary and Conclusion 87
6.1 Results of pristine PFP- and blended PFP:PEN films 87
6.2 Results of pristine DIP films 88
6.3 Results of blended DIP:C60 films 91
6.4 Outlook 92

7 Appendix 93
7.1 Form factors for simple island shapes 93
7.1.1 Form factor of a full sphere 94
7.1.2 Form factor of a cylinder 95
7.2 MATLAB codes 96
7.3 Anti-Bragg fits 100
7.4 GISAXS line profiles 101

List of Acronyms and Nomenclature **103**

Bibliography **107**

List of Publications **124**

Chapter 1

Introduction

Since the discovery of organic solids as a new class of semi-conducting materials during the early 20th century [1, 2], a lot of attention has been attracted in the scientific community [3–6]. Unlike conventional inorganic semiconductors, organic materials can form solids primarily by Van-der-Waals dispersion forces giving rise to crystalline structures and related to charge carrier transport [7,8]. Since the associated mobilities are still orders of magnitudes below that of conventional semiconductors [9], the basic idea behind the use of such materials is not to replace existing silicon-based technologies, but rather to complement and extend the range of potential applications. Additional advantages due to the unique physical properties related to this class of materials include high degree of molecular flexibility allowing for twisting and bending, biodegradability, light weight, and cheap mass production of electronic devices using ink-jet printing technologies.

However, understanding the non-trivial intermolecular interactions associated mostly with the anisotropic molecular shape, is key to decipher the manifold physical aspects behind the growth and function of organic solids [10–14]. An illustration of the complexities involved, and moreover, of how the different research topics and the specific keywords are linked to each other, is sketched in the flow-chart in Fig. 1.1. The entire process starting from the initial growth of organic thin films to their characterization and finally to the development of new innovative applications poses challenges [6, 15–17]. Some of the applications are listed in Fig. 1.1, in which they are classified into organic-photovoltaic (OPV) and organic-molecular-semiconductor (OSC) type of devices. OPV devices harvest the sunlight and convert it into electrical power. Thus, current studies aim to increase the internal quantum efficiency by varying the architecture and the materials employed in the solar cells, while focusing on cheap manufacturing techniques suited for mass production [18, 19]. OSC type of devices render several electronic applications. Organic-light-emitting-diodes (OLEDs) and organic-field-effect-transistors (OFETs) are emerging technologies, which have currently been implemented in many different products on the market, for instance in cellular phones and televisions [17]. Though there is still a lot of ongoing research trying to optimize these OSC's, particularly with regard to their efficiency and lifetime, the next generation of OSC-based devices are being focused towards organic spintronics [15, 20] and molecular storage units [21, 22], which provide

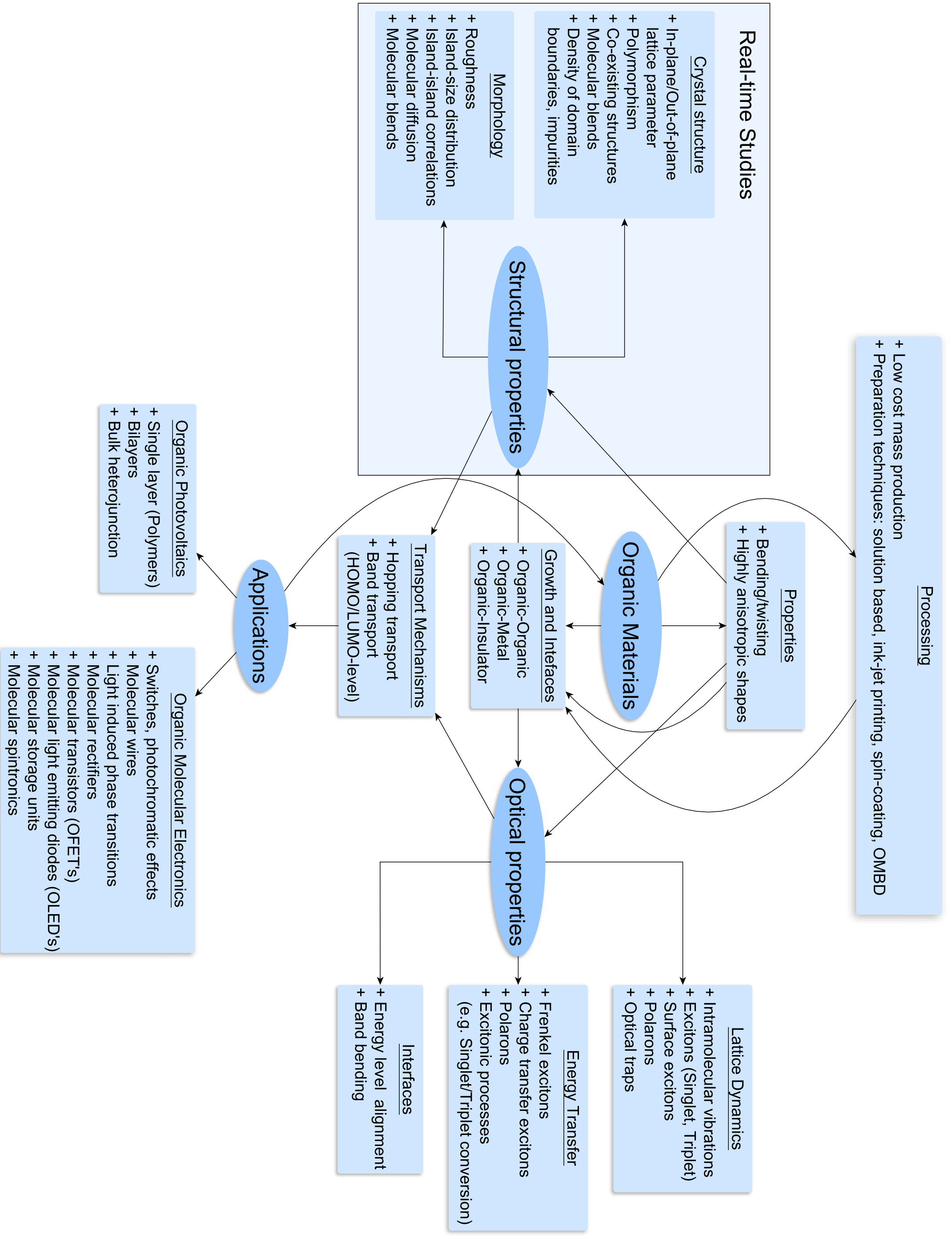

Figure 1.1: Flow-chart to illustrate the connections between the different keywords and topics of research specific to the physics of organic materials. In this thesis, we focus our investigations on the structural properties of organic thin film growth corresponding here to the block highlighted in blue.

interesting perspectives.

The sophisticated engineering and the design of devices, like the ones previously discussed, require detailed knowledge of how organic materials grow. The growth itself involves many complicated kinetic processes (see Chap. 2), and depending on the preparation technique and experimental environment (i.e. vacuum conditions, substrate type, substrate temperature etc.) the observed structures and the optical characteristics can vary substantially. Consequently, it is essential to first study the optical and structural properties of the organic films. Figure 1.1 aims to provide an idea of the most important issues relevant in the context of the film characterization. The optical characterization of the organic thin films involves basically studies with spectroscopic techniques, such as infrared/Raman spectroscopy, x-ray photo-electron spectroscopy (XPS) or ultra-violet photo-electron spectroscopy (UPS), and provides information on the intrinsic lattice dynamics and energy transfer, which are relevant in combination with multiple OSC materials (e.g. in organic pn-junctions) as well. The field of lattice dynamics describes the interaction mechanisms occurring within an organic crystal (e.g. emerging from a crystal-photon interaction), and investigates mainly intra-molecular vibrations, excited states (singlet/triplet excitons), and optical traps, all of which influence the electronic transport properties strongly. The actual energy transfer mechanism within the organic solid involves primarily these types of interactions. For instance, in the case of an OPV device, photons excite Frenkel or charge-transfer excitons, which can transfer the energy of electron-hole pairs towards their respective electrode where they are eventually collected [7,8]. Obviously, optical studies such as the ones previously discussed are required in order to build and optimize organic devices.

However, knowledge of the structural conformation of organic materials (and composition in the case of organic mixtures) are even more fundamental [23], particularly when measurements are performed in real time [24, 25]. Moreover, understanding the structure is essentially a key feature in order to classify and interpret the optical properties. Therefore, it is our prime objective to acquire first knowledge of the structure of the organic thin films (as is described in Fig. 1.1). Specifically, the crystal structure contains information of the ordering at the intermolecular length-scale and is investigated by probing the molecular lattice planes, which allows to characterize samples in terms of their polymorphism or simultaneous occurrence of different structural phases [26,27]. Both are commonly-observed phenomena, particularly appearing in mixed films [28, 29]. The morphology characterizes the ordering of the film surface on length-scales corresponding to several 100 nm and yields information of the film roughness, the island-size distribution, and the island-islands correlations. One of the key methods to obtain such features is real-time x-ray scattering, which not only performs a full statistical averaging of the sample surface (within the coherent scattering volume) but also allows a non-invasive probing of the film structure, i.e. without an interference of the measurement with the growth process.

In this thesis we study primarily the growth kinetics of both pristine and blended organic materials. Using real-time diffuse x-ray scattering measurements, we analyze the temporal evolution of the film structure and morphology. Based on our results we discuss

the effect of the molecular shape anisotropy on atomistic growth theories, particularly for the case of rod-like molecules. We expect that the findings presented in our studies can be of significant relevance for the understanding and processing of prospective OSC technologies [30–33]. The thesis is organized as follows: Chapter 2 gives a short introduction to the growth of organic thin films. Subsequently, we briefly review some of the atomistic growth theories employed for the interpretation of the results in Chap. 5. Chapter 3 summarizes the materials used in the experiments along with their crystal structure and relevant literature. The experimental methods employed in this work, particularly, the sample preparation, the scattering techniques, and the use of synchrotron radiation are briefly summarized in Chap. 4. Chapter 5 contains the experimental results and discussions and is basically organized in three parts:

- Part I discusses time-resolved measurements performed on perfluoropentacene (PFP) thin films and blended thin films consisting of perfluoropentacene and pentacene (PEN). The prime objective in this section is to study the different kinetics of grain formation for the pristine and mixed films. Specifically, we will address the following issues: How does the molecular lattice depend on the substrate temperature? Is there evidence for a molecular re-orientation in the lattice? In the blended films what is the impact of the mixing ratio on the nucleation of the different, co-existing crystal structures?

- Part II investigates the growth of ultra-thin films ($\leq$ 6 monolayer) of pristine diindenoperylene (DIP). Of particular relevance will be the following issues: What is the actual shape of the DIP-islands? How does it depend on the amount of deposited material, i.e. the film thickness? How is it related to kinetic growth aspects, such as molecular diffusion, island size evolution, and island-island correlation?

- Part III studies mixtures of DIP:C_{60} (C_{60} buckminsterfullerene) as a “real” model system for OPV applications. We will investigate how the morphology and structure are affected by the choice of the materials or, rather, on their mixing ratio. Of particular importance will be the kinetics of phase separation, i.e. the observation of a top-bottom asymmetry within the mixed layers.

Finally, Chap. 6 will summarize the most important results and provide an outlook to prospective studies involving the open issues, which were beyond the scope of this thesis.

Chapter 2

Organic thin film growth

In this chapter we will provide a brief description of atomistic growth theories. This will be of importance for the discussions in Chap. 5, where we primarily use real-time x-ray scattering techniques to study the growth and structure of thin films consisting of small organic molecules. In this context, a very important consideration is the applicability of such atomistic growth models to organic molecules, particularly because in most cases there is a distinct shape anisotropy, with implications for the structure formations.

2.1 Introduction to thin film growth

In general, the emergence of thin (organic) crystalline structures from the vapor-phase grown on inert substrates, such as silicon oxide (SiO_x), involves many kinetic processes. Some of these include, for instance, diffusion, nucleation, adsorption, desorption, etc., all of which are inherently connected to the dynamic aspects of thin film growth. Obviously, one has to precisely understand and analyze such entities to grasp the essence of growth. We will discuss this in more detail in the subsequent sections. In this section we rather restrict ourselves to the static situation observed post growth, i.e. assuming thermal equilibrium once the growth has been stopped.

A liquid-droplet model (see Fig. 2.1) is quite useful to explain the wetting behavior in heterogrowth, i.e. a material of type A is grown on a substrate of type B, at least from a qualitative perspective. Assuming thermal equilibrium, a droplet is in contact with a structure-less substrate, i.e. a substrate which has no surface potential for surface diffusion in the first approximation [35]. In this case, the contact angle θ defined between the droplet surface and the substrate plane, is given via Young's equation [34, 35]

$$\cos\theta = \frac{\sigma_{sv} - \sigma_{sa}}{\sigma_{av}} \ . \tag{2.1}$$

Here, σ_{sv}, σ_{sa}, and σ_{av} denote the surface tension (or specific surface energy of the free surface) between the substrate-vapor, substrate-adsorbate and adsorbate-vapor interfaces. Interestingly, in the case of a solid material grown on a solid substrate, e.g. lead deposited on graphite, this relation is not a bad approximation [34]. More generally for heterogrowth,

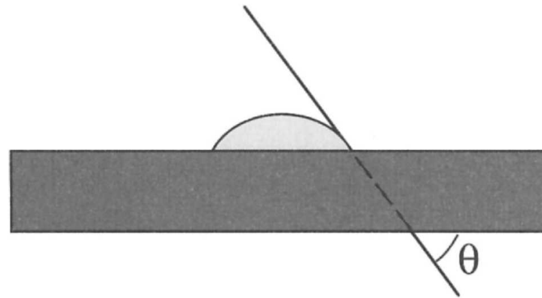

Figure 2.1: Liquid droplet on a structure-less substrate gives rise to contact angle θ. Image taken from Ref. [34].

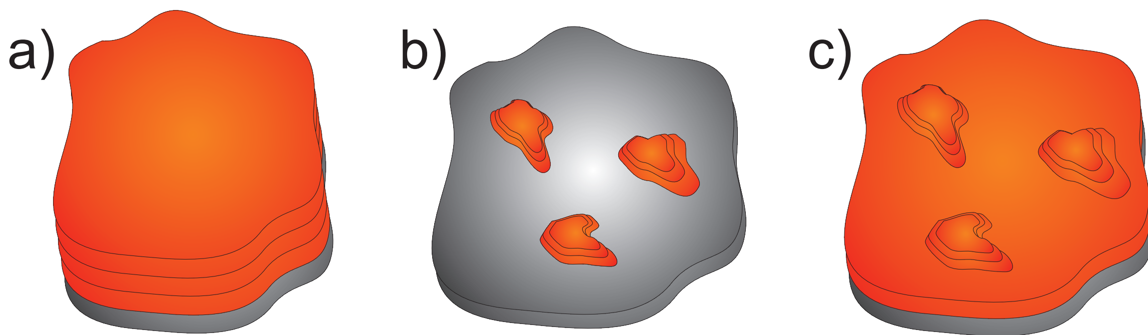

Figure 2.2: In OMBE-type of experiments there are usually three growth scenarios that can be observed. (a) Frank-Van der Merwe or layer-by-layer (lbl) growth. (b) Vollmer-Weber (VW) growth. (c) Stranski-Krastanov (SK) growth.

either for inorganic or organic materials, there are three types of scenarios summarized in the following:

- Frank-Van der Merwe (layer-by-layer, lbl) growth. In this scenario the substrate is completely wetted by the material, i.e. the growth progresses primarily in the lateral direction (2D), and the first layer is completely finished before the subsequent layer grows on top of it (see Fig. 2.2a).

- Vollmer-Weber growth. Here, mounds grow mainly in the vertical direction, i.e. the growth of the second layer sets in before the first layer is finished. The growth in the vertical direction is also referred to as 3D-growth. (see Fig. 2.2b).

- Stranski-Krastanov growth. In this situation the substrate is completely wetted by the film, i.e. the growth starts off similarly to a lbl-growth scenario. Suddenly, the growth type changes to a 3D-growth. This happens when one or more layers are completely filled and the influence of the substrate on the growth kinetics of the adsorbates, i.e. the adsorbate-substrate interaction, is shielded by the wetting layers (see also Fig. 2.2c).

When considering the previously introduced simple model of liquid droplets, it becomes clear from Eq. (2.1) that one can compare these growth scenarios to the following two extreme cases:

- In the first case we find that $\sigma_{sv} < \sigma_{av} + \sigma_{sa}$. Obviously this is related to the Vollmer-Weber type of growth, where 3D growth sets in from the very beginning of the film growth.
- Additionally, one finds that Eq. (2.1) does not work if $\sigma_{sv} > \sigma_{av} + \sigma_{sa}$, since this would imply that $\cos\theta > 1$. Therefore, we can relate this case to the situation of Frank-Van der Merwe growth.

In the case of a liquid droplet, one finds indeed that the surface tension is isotropic. In order to extend this picture to the more general situation of epitaxial growth (i.e. a crystalline film is grown on a crystalline substrate corresponding to the experiments performed in this thesis) we need to get rid of the idea of a structure-less substrate. This leads to the concepts of elasticity and commensurability. The discussion of the influence of the elasticity on the growth is not within the scope of this short introduction and can, for instance, be found in [36]. The latter one is illustrated in Fig. 2.3.

If the in-plane lattice planes of the substrate and the adsorbate do not match we expect that the structure of the substrate is superimposed on the structure of the first monolayer. This leads to lattice misfits and dislocations. The situation is illustrated for the first monolayer in the top panel of Fig. 2.3, either for krypton grown on graphite leading to a commensurate structure or for argon grown on graphite giving rise to an incommensurate structure. As the growth progresses, the adsorbate gradually tries to compensate for the misfits and adjusts to its own lattice spacing. Thus, the influence of the substrate is shielded by the molecular layers close to the substrate (see bottom panel of Fig. 2.3).

We can accept that the previous concepts and, more specifically, the answer to the question, “What exactly drives heterogrowth?” are, in a more general sense, strongly related to the interaction potentials between the participants [34, 35]. In fact, the case in which an adsorbate of type A is grown on a substrate of type B primarily depends on the relation of adsorbate-adsorbate interaction to adsorbate-substrate interaction. Both can be expressed by Hamiltonians H_{aa} and H_{as}. If the growth is dominated by the first one, where the adsorbates (atoms, molecules) experience a strong affinity, the incommensurate structure is energetically favored. On the other hand, the case that the latter interaction is significantly stronger leads to a stabilization of the commensurate structure.

The situation becomes even more complex in the case of organic materials, which will be within focus in this thesis. It becomes clear from Fig. 2.4 that the shape anisotropy of the molecules leads to additional orientational degrees of freedom, implying that, in most cases, both the molecules and the substrate will have very different in-plane lattice parameters. This gives rise to an incommensurate type of growth. In this case, the dominant structural orientation (lying or standing molecules) depends critically on the difference between the molecule-substrate and molecule-molecule interaction. For rodlike

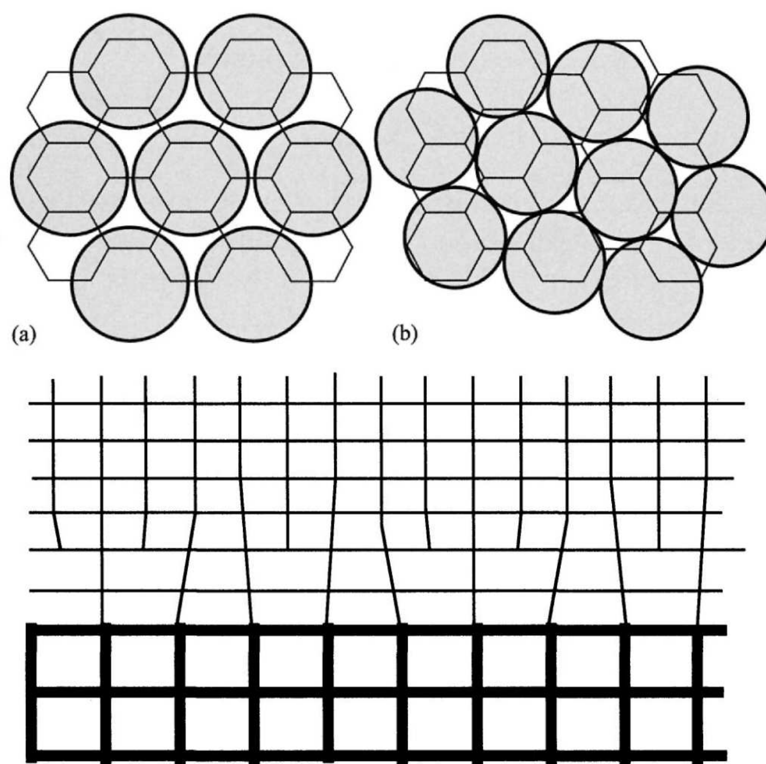

Figure 2.3: Top panel: (a) Commensurate structure of krypton grown on graphite. (b) Incommensurate structure of argon grown on graphite. Bottom panel: Schematic illustration on how the growth progresses, if the lattice spacing of the substrate (thick lines) and the adsorbate (thin lines) are incommensurate. Figures in the top and bottom panel were taken from Ref. [34].

molecules such as pentacene (see Chap. 3) and similar polycyclic aromatic hydrocarbones, the inter-molecular interaction is usually quite strong due to inter-molecular coupling of the π-orbitals. If such molecules are grown on inert substrates (weak molecule-substrate interaction) and the temperature of the substrate is sufficiently high to allow for molecular diffusion processes, the standing orientation is usually energetically favored.

2.2 Atomistic nucleation

The complicated situation of growth (involving all the kinetic effects illustrated in Fig. 2.5a is mirrored in a typical growth-scenario occurring in an ultra-high vacuum (UHV) surrounding of the sample. It can be explained in the following way: Adatoms (or molecules) are deposited with a flux F onto a substrate, which has a certain temperature T, providing the adatoms kinetic energy. Once the adatoms reach the surface they randomly migrate (owing to their kinetic energy) until events of the following kind take place:

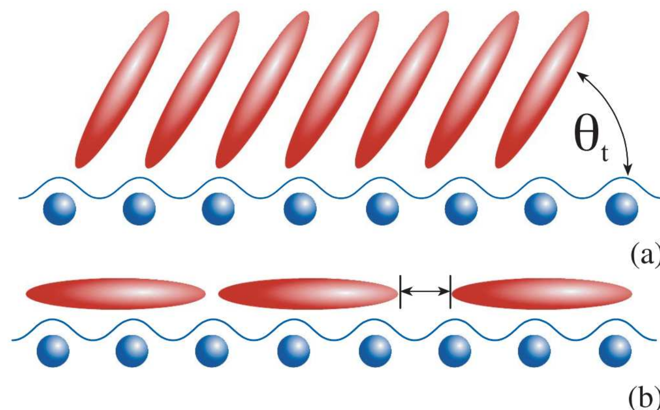

Figure 2.4: Rodlike molecules deposited on inert, isotropic substrates (surface potential of the substrate indicated by sinusoidal lines) can grow in different structural orientations. (a) If the molecule-molecule interaction dominates the growth, molecules can stand up, while forming an angle θ_t with respect to the substrate plane. (b) If the molecule-substrate interaction dominates, molecules can lie down. Figure taken from Ref. [37].

- Two adatoms can meet, leading to the nucleation of a new dimer.
- A dimer may either dissolve into two freely diffusing adatoms, or a trimer may be formed by aggregation of a new adatom.
- A trimer can, again, be converted into a dimer (by separating one adatom) or into a nucleus consisting of four adatoms (by incorporating one more adatom).
- Events involving clusters of $s \geq 4$ adatoms occur.

Aggregation of new adatoms successively leads to an enlargement of the existing nuclei, which finally coalesce into bigger islands. The scenario may then be repeated for the subsequent layers, i.e. each layer is completely filled before new-layer islands nucleate on top of the closed layer, corresponding to the case of a layer-by-layer type of growth. We can connect this to the absence (or very weak presence) of the Ehrlich-Schwoebel-Barrier (ES-Barrier) [40, 41], which is an additional energy barrier that has to be overcome by adatoms migrating from the top of an island to the island below, i.e. adatoms crossing an island step-edge (see Fig. 2.5b). More precisely, if the ES-Barrier is very weak, adatoms that arrive on top of an island can diffuse downwards easily. Consequently, the presence of such an ES-Barrier practically limits the inter-layer transport and contributes to the formation of new nuclei on top of an existing island, leading to 3D growth. Notably, all of these processes happen with a certain probability depending, *inter alia*, on the temperature T, the binding energy of the adatoms, the intra-layer diffusion D and inter-layer diffusion D', which can all be taken into account via different kinetic rates. Note that in this picture all the kinetic effects including intra-layer and inter-layer diffusion are thermally activated. Depending on the situation whether the growth mainly occurs in

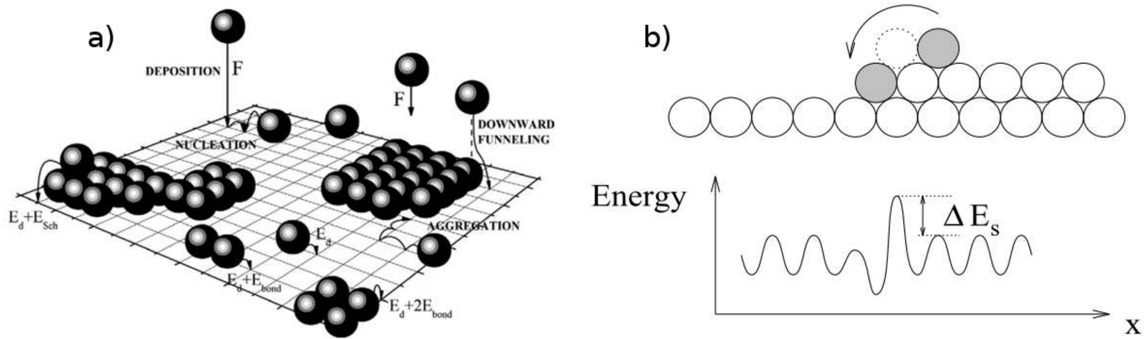

Figure 2.5: (a) Schematic illustration of the kinetic processes occurring during the deposition and subsequent assembling of the adsorbate layer (see Ref. [38] for a full description of all processes and parameters involved). (b) The crossing of a step-edge involves an additional energy barrier, ΔE_S, which is superimposed on the surface potential. Fig. (a) taken from Ref. [38] (Copyright Plenum Press,1997) and Fig. (b) taken from Ref. [39].

the lateral or in the vertical direction, the theoretical growth model and the assumptions made change. Therefore, the next section gives a brief review on the two-dimensional nucleation theory, followed by the case of a 3D growth in Sect. 2.2.2.

2.2.1 Atomistic, two dimensional nucleation

In general, as pointed out in the last section, the different kinetic effects are taken into account by rates leading to a set of coupled ordinary differential equations, whose derivation shall be illustrated here for the simple case of first layer nucleation in the very low coverage regime. This is shown explicitly in full detail and in the perspective of a more general overview (including most of the prevailing growth-theories) in Refs. [36, 39]. The nucleation of the second layer involves an additional step-edge barrier to confine the vertical migration of adatoms; therefore, we will only treat the case of the simpler, first-layer nucleation in this section. The starting point in classical nucleation kinetics, in the sense of a mean-field approach, considers the concentration n_s of clusters, which are composed of s adatoms. Assuming that the diffusion of large clusters is negligible, i.e. clusters only grow by aggregation, one can express the change of n_s in terms of a net-rate Γ_s describing the emergence of $s+1$-clusters from s-clusters, i.e.

$$\frac{dn_s}{dt} = \Gamma_{s-1} - \Gamma_s \quad (s \geq 2) \tag{2.2}$$

$$\Gamma_s = \sigma_s^c D n_1 n_s - \gamma_{s+1} n_{s+1} \ . \tag{2.3}$$

Γ_s is defined by the detachment rate γ_s (for clusters composed of s adatoms), n_1 accounts for the density of monomers (adatoms) and σ_s^c is the capture number. Using the assumption that desorption of adatoms from the surface is negligible, which is also referred to as *complete condensation limit* in the literature [39], one can express the change in the

monomer density by

$$\frac{dn_1}{dt} = F - 2\Gamma_1 - \sum_{s\geq 2} \Gamma_s \ . \tag{2.4}$$

Note that this set of equations (Eq. (2.2)–Eq. (2.4)), though giving a full description of the growth in terms of the kinetic rates, is not well-suited for computation. It depends on many different parameters, which are usually not known explicitly. In particular, the capture number σ_s^c describing the probability of an s-cluster to incorporate a new adatom depends on the cluster size and the environment around the cluster. It would, therefore, require a self-consistent implementation of a diffusion equation [39]. The solution of such rate-equation models requires a parametrization of the following type: One assumes that clusters below a critical size $i^\star$ of adatoms are considered unstable, i.e. they are allowed to dissociate, while clusters containing $i^\star$ or more adatoms are stable. This concept implies, on the one hand, that $\gamma_{s\geq i^\star} = 0$, and requires, on the other hand, that the separation of adatoms maintains thermal equilibrium, which means that $\Gamma_s = 0$ for $1 \leq s \leq i^\star - 1$. The total density of clusters is

$$N = \sum_{s=i^\star+1}^{\infty} n_s \ , \tag{2.5}$$

so one can rewrite (Ref. [39,42,43]) the previously-introduced set of equations (Eq. (2.2)–Eq. (2.4)) into

$$\frac{dN}{dt} = \sigma_{i^\star}^c D n_1 n_{i^\star} \tag{2.6}$$

$$n_s \approx (n_1)^s e^{E_s/k_B T} \quad (2 \leq s \leq i^\star) \tag{2.7}$$

$$\frac{dn_1}{dt} = F - \sigma_{i^\star}^c D n_1 n_{i^\star} - \bar{\sigma}^c D n_1 N \ , \tag{2.8}$$

where the binding energy per cluster E_s, and the average capture number of stable islands $\bar{\sigma}^c$ is introduced as

$$\bar{\sigma}^c = N^{-1} \sum_{s=i^\star+1}^{\infty} n_s \sigma_s^c \ . \tag{2.9}$$

For solving this set of equations we refer, again, to Ref. [36, 39], in which a detailed description of the atomistic growth theories is presented. Consequently, we would rather provide the final solution here. Owing to the fact that in most cases $\sigma_{i^\star}^c$ and $\bar{\sigma}^c$ can be considered as slowly-varying functions, which are usually approximated by scalar numbers, one can generally distinguish the following two *temporal growth regimes*:

- The *transient nucleation regime* (in the very early stages of growth) is characterized by the assumption that the loss terms in Eq. (2.8) are basically negligible. Introducing the *total deposited coverage* Θ, one finds that

$$\Theta = Ft \tag{2.10}$$

$$N \propto \Theta^{i^\star+2} \ . \tag{2.11}$$

- In the *steady-state nucleation regime* the loss terms cancel out each other, and the aggregation of adatoms at stable clusters is not negligible, anymore. In this case, one obtains

$$N \approx \Theta^{1/(i^\star+2)} \left(\frac{F}{D}\right)^{\frac{i^\star}{i^\star+2}} e^{E_i^\star/(i^\star+2)/k_B T} \; . \tag{2.12}$$

Equation (2.12) further implies that $N \propto \left(\frac{F}{D}\right)^{\chi}$, which is also known as the *scaling relation* with the *scaling exponent* $\chi = i^\star/(i^\star + 2)$. In both regimes the island density increases when the coverage is increased, thus Eq. (2.11) – Eq. (2.12) correspond all to the low coverage regime. However, due to different exponents the island density increases much faster in the *transient nucleation regime* compared to the *steady state nucleation regime*.

There are two remarks worthwhile mentioning before concluding this section. First, cluster mobility is neglected in this discussion implying that the island density can only decrease by means of island-coalescence [39]. The beginning of the coalescence regime is, in this sense, usually characterized by a maximum of the island density. Second, the equations valid in the *steady-state nucleation regime* will be adapted for our data-analysis presented in Sect. 5.3, in which the growth kinetics of the organic semiconductor diindenoperylene is investigated in real time. In this context it is surprising that the scaling relation works reasonably well, even if the island density is investigated not exactly in the low coverage regime. This becomes more obvious in Sect. 5.3, where the analysis is employed in a relatively large coverage range.

2.2.2 Atomistic, three dimensional nucleation

It is commonly accepted that the presence of a step-edge barrier, which imposes the condition that $D' < D$, leads to growth instability and manifests itself in the formation of 3D-mounds or *wedding-cakes* on the surface [39, 44]. Therefore, the consideration of a step-edge barrier is in complete contrast to the assumption of Sect. 2.2.1, where growth progresses only in the lateral direction. The more general description is necessitated to take such a step-edge barrier into account. One of the extreme cases in this context is an infinite step-edge barrier, where $D' = 0$, and in which the inter-layer mass-transport is completely suppressed. More precisely, one assumes that adatoms stay on the terrace on which they have been deposited. Once diffusing on the terrace they only contribute to the growth of the succeeding layer on top of it. This implies that inter-layer mass-transport and lateral mass-transport occurring between the mounds are neglected, which is only a first approximation. In the literature this is also known as *statistical growth (Poisson growth)* or the *random deposition limit*, whose equations will be provided shortly in the following (see Ref. [36, 39] for detailed explanation). Following the idea of Sect. 2.2.1, a simple set of equations can be derived based on a rate-equation approach. One considers the relative coverage θ_n of layer n whose value per definition lies in the interval $[0, 1]$ ($\theta_n = 0$ accounts for an empty layer and $\theta_n = 1$ for a completely filled layer). The *exposed coverage*, i.e. the free area of a layer which is not covered by the succeeding layer above,

can be defined as

$$\phi_{n-1} = \theta_{n-1} - \theta_n \ , \tag{2.13}$$

and is directly proportional to the flux (or rate) F

$$\frac{d\theta_n}{dt} = F\phi_n \ . \tag{2.14}$$

This set of ordinary differential equations (Eq. (2.14)) describes the continuous, temporal evolution of the coverages of the respective layers and can be solved with the boundary condition $\theta_0 \equiv 1$ (the substrate-layer is “full”) and the initial conditions $\theta_{n\geq 1}\,(t=0) \equiv 0$ (all remaining layers are “empty” when the growth starts). This leads to the solution

$$\theta_n = 1 - e^{-\Theta} \sum_{k=0}^{n-1} \frac{\Theta^k}{k!} \tag{2.15}$$

$$\Theta = \sum_{n=1}^{\infty} \theta_n = Ft \ . \tag{2.16}$$

In this set of equations Θ is the *total deposited coverage* [39]. The exposed coverage for layer n can thus be expressed as a Poisson distribution

$$\phi_n = \frac{e^{-\Theta}\Theta^n}{n!} \ , \tag{2.17}$$

of the parameter Θ. Hence, using the representation of the surface roughness σ

$$\sigma^2 = \sum_{n=0}^{\infty} (n-\Theta)^2 \, \phi_n \ , \tag{2.18}$$

one finds the important result that

$$\sigma = \sqrt{\Theta} \ . \tag{2.19}$$

Poisson growth basically provides an upper limit for the surface roughness, in the case of a complete absence of inter-layer diffusion, similar to the situation of an infinite step-edge barrier. The presence of a weak step-edge barrier, on the contrary, promotes a smoother film surface, which can be summarized with the following statement: While the inter-layer diffusion is the mechanism to decrease the surface roughness, the intra-layer diffusion only has an impact on the lateral material transport [39].

Chapter 3

Materials

In recent years organic materials have attracted much attention, particularly due to their applicability in active thin-film electronic devices. Although, the charge carrier mobility of such materials is, in general, still a few orders of magnitudes less than that of commercial, inorganic, silicon-based semiconductors, their intrinsic properties open an entirely new branch of potential applications. On the one hand organic materials offer the perspective of low-cost mass production, e.g. ink-jet printing of electronic circuits. On the other hand they provide unique physical properties not found with inorganic materials. These can comprise, for instance, extremely short carrier transit distances leading to very fast electronic response-times or, if deposited on a flexible substrate, they can easily resist mechanical deformations like bending and twisting [5].

In general, we can divide organic semiconductors into two classes of materials – polymers and small molecule OSCs [8]. The polymer-based thin films can have a relatively large degree of disorder resulting in less mobility as compared to crystalline materials. However, they are usually very cost efficient and easy to process using solution based preparation techniques such as spin-coating. In contrast, small organic molecules can have a relatively high degree of crystallinity associated with a mobility of up to $\mu \approx 1\,\mathrm{cm}^2/\mathrm{Vs}$ [45] making them in particular attractive for OPV applications. In this thesis we will only focus on the latter class. The following sections provide a short description of the materials studied in this thesis, as well as how the molecules are expected to grow, along with their relevant crystal structures.

3.1 Pentacene (PEN)

Pentacene ($C_{22}H_{14}$, PEN), or “2,3,6,7-dibenzoanthracene” as named according to the International Union of Pure and Applied Chemistry (IUPAC) is composed of five benzene rings, which are arranged in a linear structure.

In recent years pentacene (see Fig. 3.1) has not only been used as a model system to understand the growth behavior of organic thin films [47–50], but also exhibits a lot of promising electronic characteristics, which are relevant to the developing of organic semi-conducting devices and OPV applications [51].

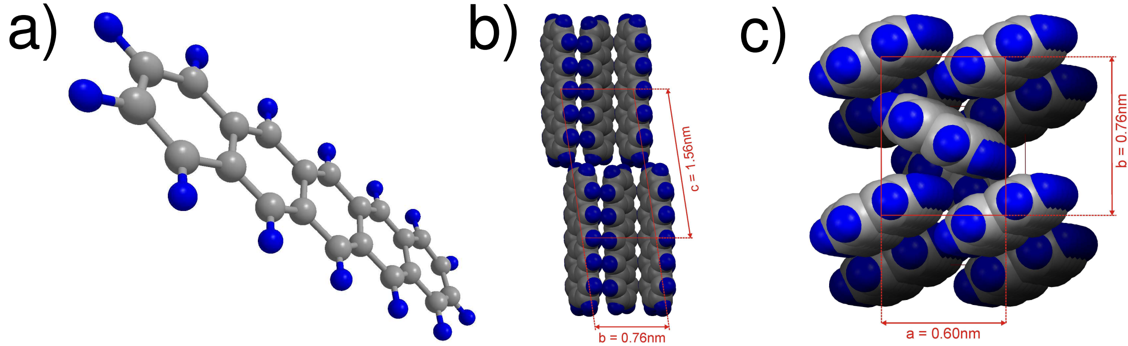

Figure 3.1: (a) Structural composition of pentacene. At 300 K, pentacene occurs within the triclinic thin-film phase with two molecules in the unit cell arranged in a herringbone-like structural conformation. Molecular orientations are shown along the $a^{\star}$-axis, i.e. perpendicular to the *bc*-plane (b) and along the $c^{\star}$-axis, i.e. perpendicular to the *ab*-plane (c). Atom positions were taken from Ref. [46].

	a [nm]	b [nm]	c [nm]	α [°]	β [°]	γ [°]	$d(001)$ [nm]
Bulk phase (BP)	0.6266	0.775	1.4530	76.475	87.682	84.684	1.412
Bulk phase (BP)	0.6485	0.7407	1.4745	77.25	85.72	80.92	1.437
Thin-film phase (TF)	0.5958	0.7596	1.561	81.25	86.56	89.80	1.54

Table 3.1: Comparison of unit-cell parameters for different polymorphs adopted by pentacene grown on SiO_x substrates. Lattice parameters taken from Ref. [52] for the bulk phases (BP), and from Ref. [46] for the thin-film phase (TF).

Pentacene is known to grow in at least three different polymorphs [52, 53], which can even exist simultaneously. It has been observed that the presence of the polymorphs depends not only on the choice of the substrate (molecule-substrate interaction), but also on the film thickness and the growth temperature. The different polymorphs can be distinguished by means of their out-of-plane lattice parameter $d_{(001)}$. A summary of the different polymorphs observed on SiO_x substrates is given in Tab. 3.1. It has been reported that the thin-film phase [54–56], i.e. substrate-induced phase, corresponding to $d_{(001)} = 1.54$ nm, predominates the film structure below a critical-film thickness ($\lesssim 30$ ML at $T_{\text{sub}} \approx 300$ K). Above that critical thickness a polymorph known as the bulk phase appears ($d_{(001)} = 1.44$ nm), which has been reported to occur early, at elevated substrate temperatures also [52].

Later studies, however, suggest that starting from the first monolayer, the bulk phase nucleates (though with less probability) along with the thin-film phase. As the growth progresses the thin-film phase is gradually suppressed by the bulk phase leading, to a saturation of the thickness of the thin-film phase [57]. The thin-film phase plays an important role for the development of OFETs because the field-induced conductivity occurs primarily within the first few monolayers. [10].

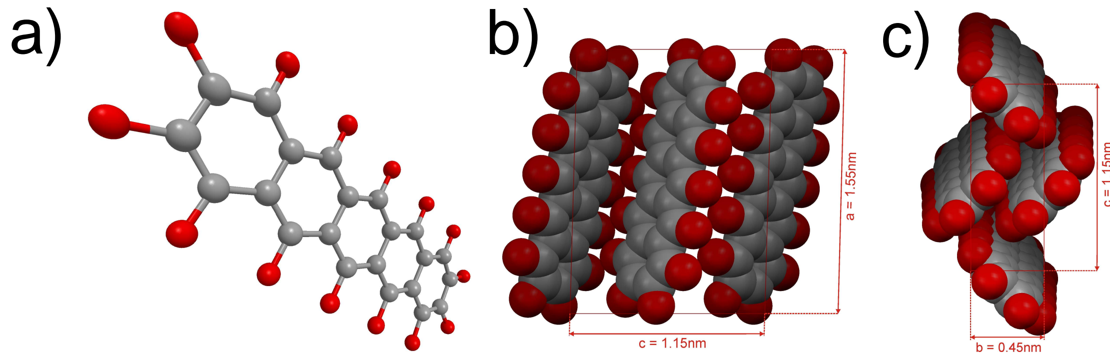

Figure 3.2: (a) Structural composition of perfluoropentacene. At 173 K, PFP occurs within the monoclinic bulk phase with two molecules in the unit cell arranged in a herringbone-like structural conformation. The corresponding molecular orientations are shown along the $b^\star$-axis, i.e. perpendicular to the *ac*-plane (b) and along the $a^\star$-axis, i.e. perpendicular to the *bc*-plane (c). Atom positions were taken from Ref. [58].

3.2 Perfluoropentacene (PFP)

According to the IUPAC-notation perfluoropentacene ($C_{22}F_{14}$, PFP) is also labeled as "1,2,3,4,5,6,7,8,9,10,11,12,13,14-tetradecafluoropentacene". Similarly as with PEN, PFP is composed of five linearly-arranged benzene rings, whose hydrogen atoms are, however, replaced by fluorine [14] (see also Fig. 3.2).

Recent time-dependent density-functional calculations illustrate that fluorination of π-conjugated organic molecules not only leads to improved stability of the material even after exposure to air, but more importantly, fluorination may provide an efficient method to convert the material into an n-type OSC [59]. Moreover, due to the similarity of the molecular dimensions and lattice parameters with those of PEN, both molecules can be considered sterically compatible. All of this offers interesting perspectives. On the one hand, the combination of PFP (acting as an acceptor (A) material) and PEN (acting as a donor (D) material) either grown as a bulk or as a planar heterojunction, allows design of different types of OSC applications [23, 58, 60]. On the other hand, molecular blends consisting of the two compounds with different molecular fractions can be explored from a structural point of view to investigate the general mixing behavior of π-conjugated molecules. This has been thoroughly investigated in previous studies [28, 61]. It was shown that, in particular, the two compounds PFP and PEN feature a strong signature of intermixing on the molecular level, i.e. the formation of mixed phases is favored. This is true even for different compounds as long as the sterical compatibility is satisfied [62]. However, the degree of molecular ordering may, in fact, exhibit an anisotropic behavior [29]. In contrast, sterically-incompatible compounds demonstrate a strong tendency to phase-separate [32].

Understanding the dynamic aspects of the thin-film growth is equally important, also

	a [nm]	b [nm]	c [nm]	α [°]	β [°]	γ [°]	$d(100)$ [nm]
Bulk phase (BP)	1.551	0.449	1.145	90.0	91.6	90.0	1.58
Thin-film phase (TF)	1.575	0.451	1.148	90.0	90.4	90.0	1.575

Table 3.2: Comparison of the unit cell parameters for the different polymorphs adopted by perfluoropentacene grown on SiO_x substrates. The lattice parameters are taken from Ref. [58, 63] for the bulk phase (BP) and from Ref. [61] for the thin-film phase (TF).

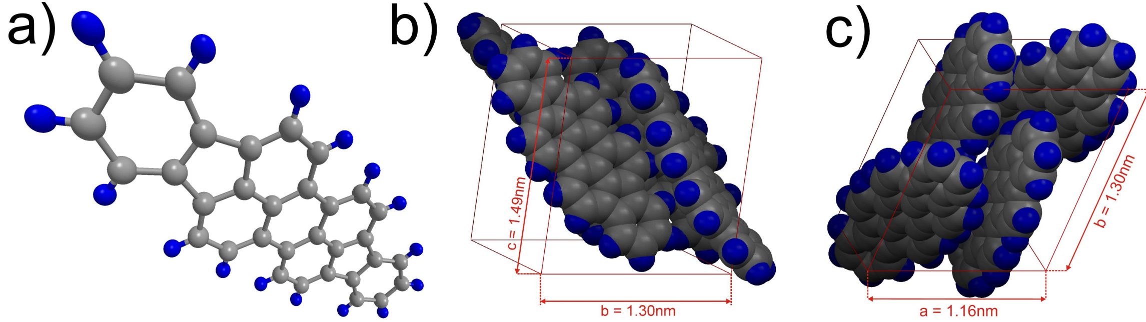

Figure 3.3: (a) Structural composition of diindenoperylene. At 298 K DIP occurs within the triclinic low temperature α-phase. Molecular orientations are shown along the $a^\star$-axis, i.e. perpendicular to the bc-plane (b) and along the $c^\star$-axis, i.e. perpendicular to the ab-plane (c). Atom positions were taken from Ref. [26].

with regard to the design of heterojunctions. Therefore, in this thesis we mainly investigate the growth dynamics of PFP thin films with respect to the in-plane structure [33]. This is complementary to previous studies, where the evolution of the out-of-plane structure was in the focus [64].

The bulk phase of PFP (grown on SiO_x substrates) was first reported in Ref. [58, 63]. The unit cell, just like in the PFP single crystal structure (see Tab. 3.2), contains two molecules arranged in a herringbone-like conformation, i.e. similar to PEN. Later studies have revealed the existence of the PFP thin-film phase [61]. Note that in our notation, which is based on Ref. [58], and which we will use throughout this thesis, the long unit-cell axis is assigned to the a-axis, though the molecules are nearly upwardly oriented with respect to the sample surface.

3.3 Diindenoperylene (DIP)

Diindenoperylene ($C_{32}H_{16}$, DIP) is also known with the IUPAC-notation “diindeno[1,2,3-cd:1’,2’,3’-lm]perylene”. It is composed of a perylene core linearly connected to several benzene-rings (see Fig. 3.3).

Similarly to other OSC materials, different polymorphs have been observed for DIP. Temperature-dependent x-ray diffraction experiments on DIP single crystals reveal that at low temperatures ($T \leq 403$ K) DIP grows in the low temperature α-phase. Here,

	a [nm]	b [nm]	c [nm]	α [°]	β [°]	γ [°]
α-phase ($T = 403\,$K) (SC)	1.16592	1.30102	1.4966	98.440	98.023	114.548
β-phase ($T = 423\,$K) (SC)	0.71709	0.85496	1.6798	90.0	92.416	90.0
σ-phase ($T = 403\,$K) (TF)	0.709	0.867	1.69	90.0	92.2	90.0

Table 3.3: Comparison of the unit cell parameters for the different polymorphs adopted by diindenoperylene. The lattice parameters are taken from Ref. [26] for the single crystal phases (SC) and from Ref. [24] for the thin-film phase (TF). Note $d(100) = 1.66\,$nm for the thin-film phase.

molecules are confined to a triclinic unit cell with four molecules arranged in a herringbone structure. At higher temperatures (observed at $T \geq 423\,$K) the unit cell is different in the sense that the structure is monoclinic with two molecules in the unit cell also arranged in a herringbone conformation [26]. This is also known as the β-phase.

DIP thin films deposited on SiO_x can grow either in the σ-orientation, with the long molecular axis orientated perpendicular to the sample surface, or in the λ-orientation, with the long molecular axis oriented parallel with respect to the sample surface. At room temperature the σ-orientation prevails during the initial stages of the growth because the λ-phase favors the nucleation on top of the σ-oriented crystallites [65]. The structure of the σ-phase has been determined in Ref. [24]. It was shown that at $T = 403\,$K the thin film σ-orientation is essentially very similar to the high-temperature single-crystal phase and, accordingly, very different from the single crystal phase at the same temperature, which has four molecules in the unit cell. The different polymorphs are listed in Tab. 3.3.

Particularly relevant in the context of the growth physics are some of the rather complex processes observed during the deposition of DIP. These include kinetic effects like a post-growth structural re-organization on the surface [66, 67], a rapid roughening of the film surface [68, 69], or the competition of different structural orientations [26, 65]. All of these effects are interconnected to the molecular flux, the kinetic energy of the molecules and the molecular diffusion. Remarkably, it was reported that in combination with different materials, DIP either favors a thickness dependent phase separation (in the case of sterically incompatible materials) [32] or an anisotropic ordering behavior (in the case of sterically compatible materials) [29]. These properties, along with the reported ambipolar charge carrier transport in donor:acceptor blends [70] of DIP clearly offer interesting perspectives in the development of OSC applications.

3.4 Buckminsterfullerene C_{60} (C_{60})

Another prominent organic semiconductor is buckminsterfullerene C_{60} (C_{60}) (see Fig. 3.4), which is also known in the IUPAC notation as"(5,6)fullerene-C60-Ih".

For various reasons, C_{60} is considered an interesting material. On the one hand the spherical and buckyball-like shape of the molecule [73–75] provide an interesting model system to study the growth mechanisms of isotropically shaped materials. This becomes

	a [nm]	b [nm]	c [nm]	α [°]	β [°]	γ [°]
HCP ($P6_3/mmc$)	1.0009	1.0009	1.6338	90.0	90.0	120.0
FCC ($Fm\bar{3}m$)	1.4156	1.4156	1.4156	90.0	90.0	90.0
SC (Low Temp.)	1.404	1.404	1.404	90.0	90.0	90.0

Table 3.4: Comparison of unit cell parameters for different single-crystal structures of buckminsterfullerene C_{60}. Crystal structures were observed to occur at room temperature either in a hexagonal closest packing (HCP) or a face centered cubic (FCC) lattice. At low temperatures ($T = 249\,\mathrm{K}$) a simple cubic (SC) phase is observed. Lattice parameters taken from Refs. [71, 72].

even more important in conjunction with molecules that differ chemically – allowing to reveal some of the manifold and complex aspects of thin film growth of organic blends [32, 76]. On the other hand one can take advantage of intrinsic electronic properties such as C_{60}'s applicability as an acceptor material for developing of OSC devices [77–79].

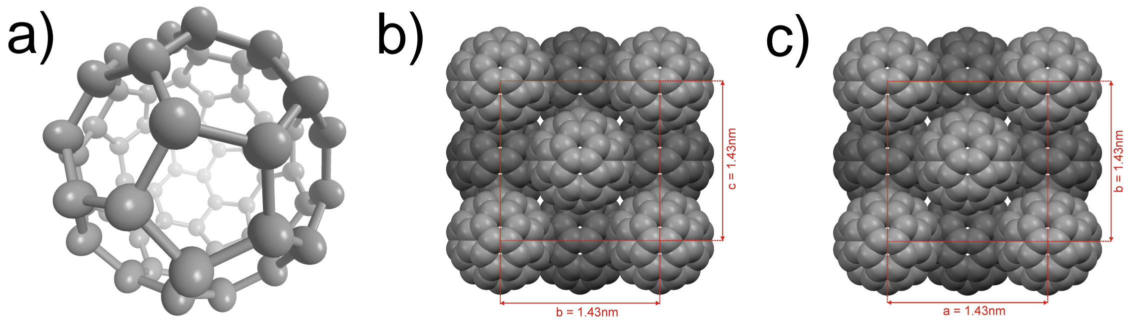

Figure 3.4: (a) Structural composition of buckminsterfullerene C_{60}. C_{60} single crystals can be grown from solution resulting in a FCC structure. Molecular orientations (at room temperature) are shown along the $a^{\star}$-axis, i.e. perpendicular to the bc-plane (b) and along the $c^{\star}$-axis, i.e. perpendicular to the ab-plane (c). Atom positions taken from Ref. [80].

In the single crystal, C_{60} grows either in the hexagonal (HCP), or in the face centered cubic (FCC) phase as shown in Tab. 3.4. At low temperatures, i.e. $T = 249\,\mathrm{K}$, a molecular arrangement corresponding to a simple-cubic (SC) structure with four molecules per unit cell is observed [71, 72].

Note that when grown on SiO_x, C_{60} growth is polycrystalline with a low structural order in the out-of-plane direction (see also measurements in Sect. 5.4). Therefore, a Bragg reflection in the out-of-plane direction is usually not observed on SiO_x.

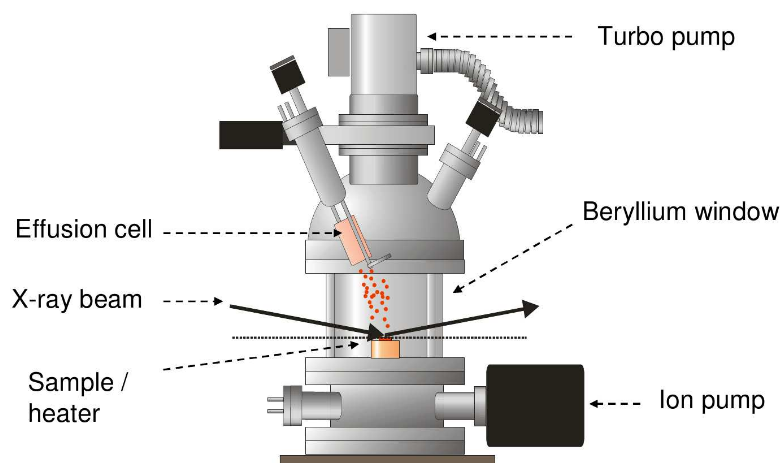

Figure 4.1: Portable UHV-chamber, in which the samples are prepared and probed with x-rays. Image taken from Ref. [50]

Chapter 4

Methods

In this chapter we will briefly review some of the experimental techniques used to prepare and measure our samples.

4.1 Organic molecular beam deposition (OMBD)

As previously mentioned in Chap. 3, there are multiple techniques to grow organic thin films. In this thesis we have used exclusively samples prepared via the organic molecular beam deposition (OMBD) method. On the one hand it allows one to grow highly crystalline films, and on the other hand the growth parameters can be controlled precisely. Moreover, to grow the films in an UHV surrounding a rather sophisticated experimental setup is required. Figure 4.1 shows the portable UHV-chamber employed in the lab and during the beam-times, to prepare the samples and to obtain *in situ* x-ray measurements (while providing an evacuated environment) [81]. The vacuum in the chamber is main-

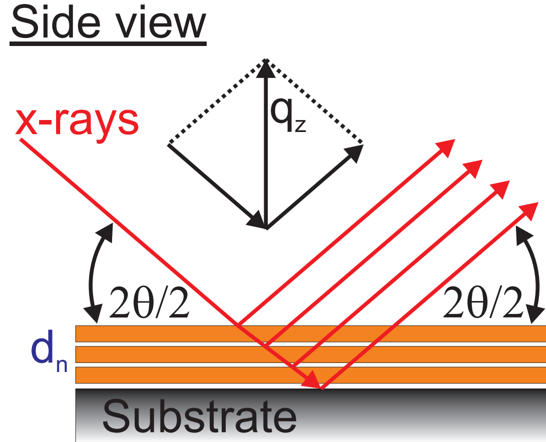

Figure 4.2: Side view of a stratified sample, which is probed with the XRR technique. The incidence and the exit angle are scanned during measurement, maintaining the condition $\alpha_i = \alpha_f = 2\theta/2$. Accordingly, the scattering intensity is obtained as a function of the z-component of the momentum transfer (see scattering-triangle on top). The scattering of x-rays on the different layers (with thicknesses d_n) gives rise to interference phenomena, which are apparent in the XRR scattering profile (see also Fig. 4.4a).

tained via the coupling of a membrane-, turbo-molecular, and ion pump, yielding a base pressure of the order of $\simeq 10^{-10}$ mbar. Using a temperature-controlled sample stage, the substrate temperature can either be heated up to $\simeq 600$ °C (completely blowing off the organic layers), or by using liquid nitrogen it can be cooled down to $\simeq -130$ °C (for low temperature growth experiments). Furthermore, the chamber is equipped with two Knudsen effusion-cells, which can be simultaneously used to grow organic binary mixtures. A Beryllium window allows for monitoring the film growth with x-rays in real time.

4.2 X-ray reflectivity (XRR)

One of the major techniques to study the structural and morphological properties of (organic) thin films is x-ray scattering. The out-of-plane structure is of high importance, particularly for the processing of optoelectronic devices. In this context, x-ray reflectivity (XRR) has been proven to be a very powerful tool. Figure 4.2 shows a sketch of the scattering geometry, generally employed in XRR type of experiments. The orientation of the scattering plane, in which the angular positions of the incoming x-ray beam (the incidence angle α_i) and of the detector (exit angle α_f) can be changed simultaneously during data acquisition, is perpendicular to the substrate plane. The reflectivity of the sample is then obtained by measuring the reflected intensity as a function of the scattering angle 2θ, while maintaining the condition $\alpha_i = \alpha_f = 2\theta/2$, i.e. by only scanning the specular rod in the reciprocal space. Consequently, the z-component of the momentum transfer (q_z) is obtained, yielding only out-of-plane structural information of the sample.

In the case of a multilayer sample, depicted in Fig. 4.2, the reflected intensity comes from the coherent superposition of the diffracted waves emerging from the respective layers n. Note that, generally, there are two different approaches to calculate the reflected intensity. We will briefly touch upon both. The following two sections aim to summarize some of the chapters from Ref. [82]. More information on XRR can be found in Ref. [83–87], for instance.

4.2.1 Dynamical theory

In *dynamical scattering theory* we solve the Maxwell equations describing the propagation of light, here in the case of a stratified medium (see Fig. 4.2). Consequently, one has to take into account all the reflected and transmitted waves, which arise at each interface of the multilayer sample. More precisely, each layer of thickness d_n gives rise to a phase difference of the penetrating waves. To obtain the reflected intensity one has to sum over all the partial waves, taking the respective phase differences into account. This implies that, per definition, on the one hand all the multiple scattering and absorption effects most dominant when incidence angle α_i or exit angle α_f are very close to the critical angle α_c are accounted for. On the other hand, knowing all the parameters describing our stratified medium (see Fig. 4.2) means we obtain an exact solution of how the sample looks like in the out-of-plane direction. In this sense, one of the central results in dynamical theory for calculating the specular intensity in the out-of-plane direction is the Parratt formalism. One can conveniently motivate the derivation by considering the following models:

Reflection from perfectly sharp, flat interface
Based on laws describing the propagation of light, a difference in the indices of refraction at the interface splits the incoming ray of light into a reflected and a transmitted ray (see Fig. 4.3a). Thus, in the case of x-rays one can define a complex index of refraction

$$n \equiv 1 - \delta + i\beta \ , \qquad (4.1)$$

with δ describing the dispersion and β describing the absorption. Forcing continuity at the interface renders the Fresnel equations for the reflected and transmitted amplitudes (r, t) of the electric field vector

$$r = \frac{\alpha - \alpha'}{\alpha + \alpha'} \ , \qquad t = \frac{2\alpha}{\alpha + \alpha'} \ . \qquad (4.2)$$

Note that in this representation the angles of incidence and reflection ($\alpha_i = \alpha_r \equiv \alpha$) are defined between the incoming ray of light and the interface, while the angle of transmission (α') is defined between the interface and the transmitted ray. Owing to the complex index of refraction the angle of transmission is defined to be complex, as well

$$\alpha' \equiv Re(\alpha') + iIm(\alpha') \ . \qquad (4.3)$$

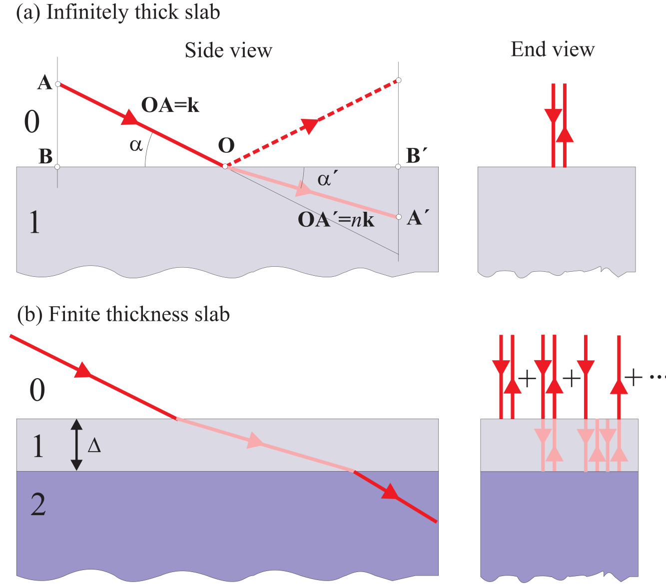

Figure 4.3: At interfaces the incoming x-ray wave splits into a reflected and transmitted beam. (a) In the case of an infinitely thick slab the total reflectivity can be calculated using the Fresnel equations. (b) For a slab of finite thickness Δ an infinite number of reflections occurs. The total reflectivity is in this case obtained by summing up all the partial reflections. Figure (a)–(b) taken from Ref. [82]

The Fresnel reflectivity R_F is obtained from the absolute square of the reflected amplitude, i.e. $R_F = |r|^2$, and it can be shown that it decays with $R_F \propto q_z^{-4}$.

Reflection from a homogeneous slab

The previous discussion of one interface (or, equivalently, an infinitely thick slab) can easily be extended to the situation of a slab of finite thickness Δ (single layer) sitting on top of an infinitely thick slab (substrate), i.e. we have to take two interfaces into account (see Fig. 4.3b):
$0 - 1$(air – slab of thickness Δ) ; $1 - 2$ (slab of thickness Δ – infinitely thick slab). This gives rise to the following multiple scattering effects:

1. Reflection: r_{01} (air - thin slab).
2. Transmission t_{01} (air - thin slab) + reflection r_{12} (thin slab - infinite slab) + transmission t_{10} (thin slab - air) modulated with a phase factor ($p = e^{ik \sin \alpha \Delta} \equiv e^{iq_z \Delta}$), which takes into account the phase shift a wave with wave-number k experiences when propagating through the thin slab of thickness Δ, leading to: $t_{01} r_{12} t_{10} p^2$.
3. Multiple reflections on both interfaces.

The reflected intensity at the interface (air - thin slab) is then obtained by an infinite

summation of all multiply scattered amplitudes, leading to a geometric series, which can be expressed as

$$r_{\mathrm{slab}} = \frac{r_{01} + r_{12}p^2}{1 + r_{01}r_{12}p^2} \ . \tag{4.4}$$

Reflection from multilayer structures
In view of the preceding discussion a stratified medium can be considered as a stacked multilayer system consisting of N slabs of finite thickness Δ_n. It is now straightforward to show that the reflected intensity of such a stacked system can be obtained by iteratively calculating the reflected amplitude of each slab. One basically starts from the substrate, which has no multiple reflections due to its infinite thickness, and progresses iteratively in calculating the reflected amplitude for each slab. This method is also known as the *Parratt-formalism* [84]. In this sense, the *Parratt-formalism* is as an exact recursive-matrix method to calculate the reflectivity of a stacked multilayer system, while taking all the multiple scattering events into account.

4.2.2 Kinematical theory

Kinematical scattering theory is based on the first-order Born approximation (BA). This implies that multiple scattering effects are not accounted for and limits the validity of this theory to regions where $\alpha \gg \alpha_c$ (or, equivalently, $q_z \gg q_{z,c}$). Although, the *dynamical scattering theory* provides an exact calculation of the specular intensity, there are situations in which it is more illustrative to use the latter approach. *Kinematical scattering theory* allows, for instance, to directly relate the electron density profile $\rho(z)$ of the sample to the scattered intensity.

Reflectivity from graded interfaces
One uses a similar approach as in the case for the multilayer system, i.e. assuming that an infinitesimally thin slab at a depth z can be expressed as

$$\delta r(q_z) = -i\frac{q_{z,c}^2}{4q_z}\rho(z)dz \ , \tag{4.5}$$

one can derive an expression for the reflectivity observed at a graded interface (by an integration over the graded interface)

$$R(q_z) = R_F(q_z)\left|\int_0^\infty \left(\frac{d\rho}{dz}\right) e^{iq_z z}dz\right|^2 \ , \tag{4.6}$$

which is also known as the *master equation.* Note that $R_F(q_z)$ is the previously-introduced Fresnel reflectivity and $\rho(z)$ is a function satisfying $\rho(z) \to 1$ as $z \to \infty$. It is now quite instructive to show that in the case of a graded interface having the width σ, which,

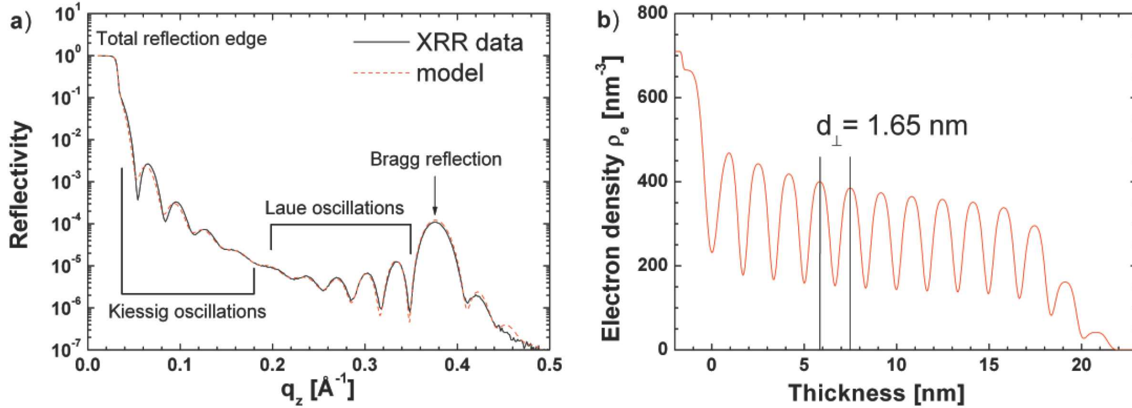

Figure 4.4: (a) 20 nm DIP grown on SiO_x along with a fit based on Parratt-model. (b) Corresponding electron density profile obtained from Parratt-fit in (a). From the oscillation period of the electron density profile, one can infer to the out-of-plane lattice spacing $d_\perp$. (a–b) taken from Ref. [76].

for instance, can be modeled using the error function $\rho(z) = \text{erf}\left(\frac{z}{\sqrt{2}\sigma}\right)$, the reflectivity becomes

$$R(q_z) = R_F(q_z)e^{-q_z^2\sigma^2} \; . \tag{4.7}$$

Note that the exponential factor on the right hand side of Eq. (4.7) is sometimes in the literature also referred to as *Névot-Croce factor*. In this sense, the grading of the interface leads to an exponential decrease of the Fresnel reflectivity.

4.2.3 Characteristic shape of x-ray reflectivity curves

Figure 4.4a shows a typical XRR curve of 20nm DIP deposited on SiO_x along with a fit-model based on the Parratt formalism (see Sect. 4.2.1). The angular dependence of the intensity transforms into reciprocal space according to

$$q_z = \frac{4\pi}{\lambda}\sin\left(\frac{2\theta}{2}\right) \; . \tag{4.8}$$

It becomes clear from the previous discussion that in XRR type of experiments we basically observe interference phenomena, which happen on different length-scales. Accordingly, we can distinguish different regions in Fig. 4.4a containing different information on the out-of-plane structure of the sample. We will discuss this briefly in the following:

Total-reflection edge
Below the critical angle α_c of the material we observe that the incoming x-rays are totally reflected from the surface. Once we approach the critical angle, x-rays start to penetrate the material and the reflectivity decreases. From the position of the critical angle we can

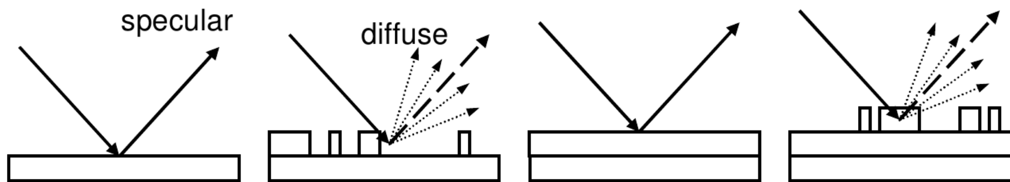

Figure 4.5: Subsequent filling of individual layers in periodic manner increases and decreases the film roughness, giving rise to periodic oscillations of the specular and diffuse scattering intensity. Image taken from Ref. [50]

infer the dispersive part of the index of refraction, which is related to the mean electron density of the material, i.e.

$$\alpha_c = \sqrt{2\delta} = \frac{\sqrt{4\pi\rho r_0}\lambda}{2\pi} \,, \tag{4.9}$$

$r_0 = 2.82 \times 10^{-5}$ Å being the classical radius of an electron.

Kiessig oscillations
Kiessig fringes emerge from an interference of x-rays, which are reflected from the top-layer and the substrate. Accordingly, one can relate the *total film thickness* d_{tot} to the period Δq_z of the oscillation via $d_{\mathrm{tot}} = \frac{2\pi}{\Delta q_z}$.

Laue oscillations
Laue fringes emerge from a coherent scattering of x-rays on crystallites. From the period of the oscillations Δq_z one can infer to the coherent crystallite size in the out-of-plane direction, d_{coh}, via $d_{\mathrm{coh}} = \frac{2\pi}{\Delta q_z}$.

Bragg reflections
Bragg reflections arise from the coherent scattering of x-rays on the lattice-planes in out-of-plane direction. One can relate the out-of-plane lattice spacing d_n to the position of the Bragg peak q_z via $d_n = \frac{2\pi n}{q_z}$, n being the order of the Bragg reflection.

For a detailed description of the XRR-technique and the interpretation of the XRR line profiles we, again, refer to Ref. [82, 86, 87].

4.3 Growth oscillations

Following the discussion of different growth types in Sect. 2.1 it becomes clear that in a real-time scattering experiment, where, for instance, the reflectivity of a sample is monitored during the growth's progress, the dependence of the scattered intensity on the growth time is not simply a constant function, but rather changes during the growth.

Moreover, one can analyze such behavior under the specular and diffuse measurement conditions, both leading to *growth oscillations*.

In the case of a layer-by-layer type of growth (see also Fig. 4.5), where the coverage of the top layers increases ($\theta \in [0, 1]$), the film roughness changes periodically from a minimum (completely filled layer) to a maximum (half filled layer), and again to a minimum (completely filled layer). When the roughness exhibits a minimum one observes a maximum in the specular intensity. When the roughness is maximal one finds greater intensity in the diffuse channels. Moreover, since the overall number of scattered photons does not change in a first approximation (when neglecting absorption) a strong diffuse scattering signal leads to weaker intensity in the specular channel. Consequently, an oscillation in the intensity of the specular and the diffuse channels is measured. In contrast, in the case of 3D growth the film roughness increases monotonously as the growth progresses, and we observe the damping of *growth oscillations* in the specular and the diffuse scattering regimes.

Specular *growth oscillations* can be well-described using the *kinematical scattering theory*. In particular, one finds for the functional dependence of the scattering intensity [25, 31, 88]

$$I(t) = \left| A_{\mathrm{sub}}(q_z) e^{i\phi} + c \sum_n \theta_n(t) e^{-inq_z d} \right|^2 , \tag{4.10}$$

with the scattering amplitude A_{sub}, the phase shift ϕ, the layer form factor c, the layer coverage θ_n of layer number n, the out-of-plane component of the momentum transfer q_z, and the out-of-plane lattice parameter d. Multiple scattering events and absorption effects are neglected in this equation implying that the specular intensity is not properly reproduced very close to the critical angle. It becomes clear from Eq. (4.10) that additional assumptions on how the film coverage evolves in the respective layers are required. In the literature there are many different approaches to predict the evolution of the film growth [25, 36, 43, 89–92]. We will analyze the specular *growth oscillations* in larger detail in Sect. 5.3.2, primarily based on the Trofimov growth-model [93–96]. Diffuse *growth oscillations* are not trivial to simulate. However, we will qualitatively discuss it in Chap. 5, as well.

4.4 Grazing incidence small angle x-ray scattering (GISAXS)

Grazing incidence small angle X-ray scattering (GISAXS) is used in Chap. 5 as one of the major methods to probe and characterize the morphologies of different samples. This is done either post growth, or in real time studies, where the film growth is monitored. The geometry typically employed in GISAXS experiments is sketched in Fig. 4.6a. The x-ray beam impinges the sample under an incidence angle α_i and the scattered GISAXS signal is measured on an area detector (see Sect. 4.7) very close to the origin in reciprocal

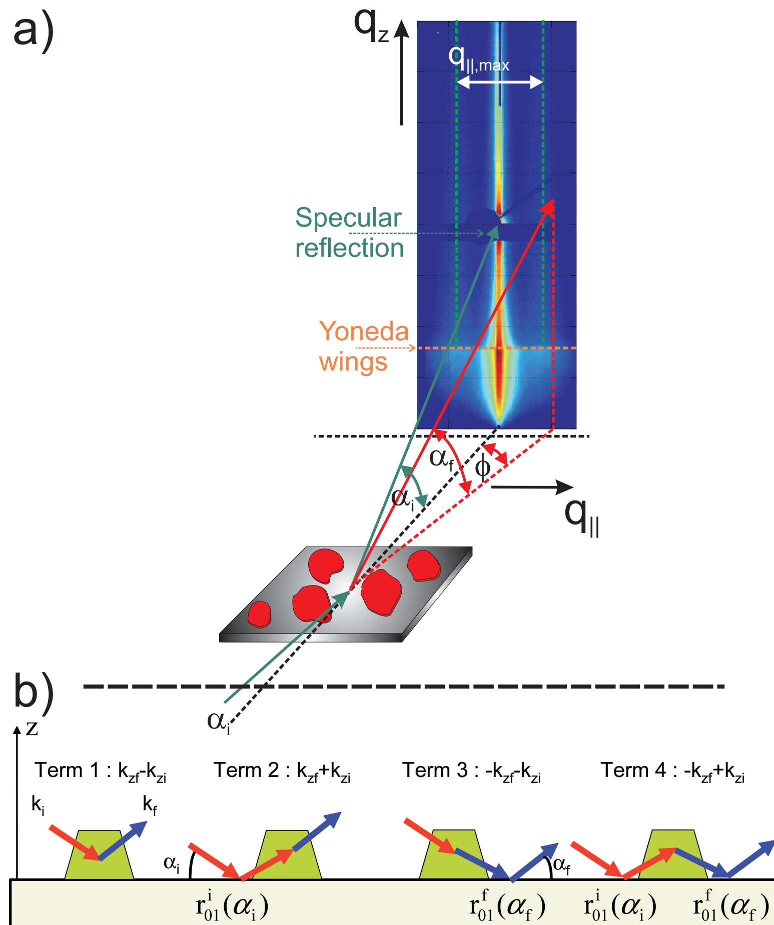

Figure 4.6: (a) Scattering geometry used in GISAXS experiments. Image taken from Ref. [30]. (b) Illustration of multiple scattering events taken into account in DWBA theory. The DWBA island form factor depends on the four depicted island form factors (in the Born approximation), evaluated for the different vertical components of the momentum transfer and the Fresnel reflection coefficients for the four scattering events. Image taken from Ref. [85].

space. Accordingly, the scattering intensity varies with the exit angle α_f and the in-plane scattering angle ϕ. In particular, one finds the relations between the three scattering angles and the momentum transfer

$$q_x = k\left[\cos\alpha_f \cos\phi - \cos\alpha_i\right] \tag{4.11}$$
$$q_y = k\left[\cos\alpha_f \sin\phi\right] \tag{4.12}$$
$$q_z = k\left[\sin\alpha_f + \sin\alpha_i\right] \ . \tag{4.13}$$

During measurement α_i is usually fixed very close to the critical angle α_c. This implies that an evanescent wave-field is created, whose penetration depth can be controlled by varying α_i in order to probe the (organic) layer only. Thus, scattering coming from

the substrate is mainly suppressed, making GISAXS an ideal surface-sensitive scattering technique. Moreover, GISAXS allows one to probe the morphology of the samples. The variation of the electron density is measured on large length-scales, yielding information on island sizes, inter-island distances and island-island correlations. Hence, GISAXS can be compared directly to AFM. In Fig. 4.6a one observes the GISAXS signal for a thin DIP-layer grown on a SiO_x-substrate, whose typical features will be discussed in the following. More general information on the GISAXS technique can be found, for instance, in Refs. [85, 97–100].

Specular reflection

Specular reflection corresponds to the case where ($\alpha_i = \alpha_f$, $\phi = 0$). The intensity observed in this spot is usually several orders of magnitude higher than that of the diffuse scattering around. The finite dynamic range of the detector requires one to shield the specular intensity with a beamstop (round shadow in Fig. 4.6a) in order to resolve the diffuse intensity.

Yoneda wings

Yoneda wings are observed in the region close to the critical angle, i.e. ($\alpha_f = \alpha_c$, ϕ). These features cannot be explained using the first-order Born approximation, i.e. using the *kinematical approximation*. A modification of the theory is required, leading to the distorted wave Born approximation (DWBA) [98]. DWBA is a first-order perturbation theory describing the propagation of light, when taking into account the multiple scattering events occurring close to the critical angle (see Fig. 4.6b). The unperturbed, i.e. exact state, is given by the solution of the Fresnel equations and the perturbation comes from the coherent scattering of the islands on top of the surface. In DWBA, the Yoneda-wings arise from the coherent superposition of the four scattering events (depicted in Fig. 4.6b), which can involve a reflection from both the incident and the scattered wave on the surface. Consequently, the diffuse signal has a maximum [85].

Specular rod

The specular rod corresponds to the case where (α_f, $\phi = 0$) and is characterized by a strong scattering signal. The intensity is proportional to both the number of scatterers N in the scattering volume and the mean island DWBA form factor $\mathcal{F}$ at the origin [85]. Thus,

$$I_{\mathrm{coh}} \propto N \langle \left| \mathcal{F}(q_{||} = 0, k_{i,z}, k_{f,z}) \right|^2 \rangle \delta(q_{||}) \ , \tag{4.14}$$

$\delta(q_{||})$ being the Kronecker-delta function. In practice, all the sources, contributing to the loss of coherence (energy-/angular-resolution, detector-acceptance and microscopic sample-curvatures) increase the (finite) width of the specular rod [85]. It is, therefore,

difficult to provide an exact reproduction of the intensity in this angular regime, at least in most cases.

Vertical intensity maxima
In all the samples we analyze in this work we typically observe two vertically distributed intensity maxima centered around $q_{||} = 0$. The distance between the maxima carries information about the preferred nearest-neighbor distance contained in the sample morphology. We will discuss this in more detail in Chap. 5.

4.5 Grazing incidence diffraction (GID)

The scattering geometry in grazing incidence diffraction (GID) experiments is similar to that shown in Fig. 4.6(a). The penetration depth of the evanescent wave-field is controlled by varying the incidence angle α_i very closely to the critical angle α_c, allowing one to obtain a surface-sensitive depth-resolved scattering signal in which the contribution from the substrate can be suppressed. In contrast to GISAXS, the in-plane angle ϕ is usually chosen as much larger, particularly $\phi \gtrsim 5°$. Consequently, GID is used to probe lattice planes in the in-plane direction. In this sense XRR and GID can be considered complementary techniques, since the first probes the lattice planes only in the out-of-plane direction, while the second probes them only in the in-plane direction. In Chap. 5 we analyze the GID profiles mainly in terms of the position and the width of the Bragg peaks. The position yields the in-plane distance between lattice planes, while the width can be related to the coherent in-plane crystallite size, in the associated direction. GID measurements were performed post growth and in real time. More information on GID can be found in Refs. [82, 87, 97], for instance.

4.6 Synchrotron radiation

Synchrotron radiation is not only required to provide the high beam intensity necessary for the diffuse scattering techniques employed in Chap. 5, but also to yield a large coherence length of the x-ray photons. All are crucial for resolving the morphology of the samples, which can comprise of length-scales of several 100 nm.

Figure 4.7 illustrates the working principle of a 3$^{\text{rd}}$ generation synchrotron facility. Electrons are accelerated in an evacuated storage-ring to kinetic energies of several GeV. Large magnets mounted along the ring-side force the electron beam into curved pathways, leading to the creation of synchrotron radiation. The radiation's energy and coherence can be controlled precisely by the magnetic field. Depending on the experiment, the such-obtained x-ray beam is monochromized and focused by beamline optics. Such a beam is then delivered to the experimental hutch. More detailed descriptions can be found in Ref [82, 101], for instance.

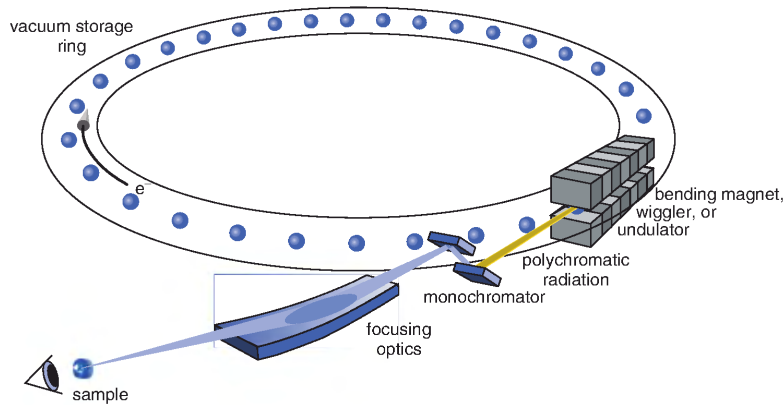

Figure 4.7: Working principle of a 3rd generation synchrotron facility. Image taken from Ref. [101].

4.7 Detector specifications

Photon detection with different types of area detectors used in this work is either based on the charged-coupled-device (CCD) or on the single-photon-counting (SPC) principle [101]. In the first case, photons are detected by individual scintillator elements and, using optical fibers, are subsequently guided to single CCD- semiconductor chips. The active area is composed of several CCD-chips arranged in a 2D matrix. In single photon counting detectors the charge generated in each pixel, due to an absorbed x-ray photon, is amplified and subsequently compared to a threshold level. In the case that the signal is larger than the threshold, the detected event counts as a photon and the respective counting unit (connected to that pixel) is incremented. The advantages of SPC compared to CCD detectors are extremely good signal-to-noise ratio, fast read-out time and a high dynamic-range. Furthermore, one can easily filter fluorescence radiation by changing the threshold level. A detailed introduction to the working principle of the different detector types can be found in Ref. [101]. Table 4.1 provides a short comparison of the technical specifications.

4.8 Atomic force microscopy (AFM)

Atomic force microscopy (AFM) is a versatile technique allowing one to locally probe virtually any kind of surface [102]. These include soft, liquid, and solid surfaces as they can occur, for instance, in soft condensed-matter science [103, 104]. The spatial resolution in the vertical direction is usually in the sub-nanometer range, while in the in-plane direction it spans several tenths of nanometers [105]. Measurements are performed in real space allowing for direct inspection of the surface morphology. In contrast to x-ray techniques one of the major drawbacks of AFM is that one can not follow the growth in real-time since the measurement itself would interfere with the deposition process. Additionally, in-

	MAXIPIX[a,b]	PILATUS 1M[a,b]	MARCCD[a]
working principle	SPC	SPC	CCD
pixel pitch	55×55 [µm^2]	172×172 [µm^2]	~ 80 [µm]
image dimension	1296×256 [px]	981×1043 [px]	2048×2048 [px]
active area	71.3×14.1 [mm^2]	169×179 [mm^2]	133 [mm] (diameter)
dynamic range	2×10^5 [cnts/sec/px]	2^{20} [cnts/px]	–
data output time	$\simeq 0.99$ [msec]	3.6 [msec]	~ 15 [sec]
beam energy	$\sim$ 5–25 [keV]	$\sim$ 3–30 [keV]	–
max. count rate	$\sim 10^8$ [cnts/sec/mm^2]	$> 2 \times 10^6$ [cnts/sec]	–

Table 4.1: Comparison of the technical specs for the different types of area detectors employed in the experiments. For some of the parameters no information could be found.

[a] *http://www.esrf.eu*
[b] *http://www.dectris.com*

terpretation of the data can be difficult under certain conditions. In principal, one needs to take into account all the effects induced by the tip, which can lead to distortions of the image if the sample has a complex morphology. Furthermore, measurements have to be performed on many different sample spots in order to get the same meaningful, statistical significance as those of x-ray studies. However, in most cases, such a measurement strategy would be rather time-consuming. Beside the characterization of the surface morphology the AFM probe can be modified to determine, for instance, the conductivity or the interaction potential of the tip with the sample surface.

AFM measurements shown in this thesis, are performed on a JPK Nanowizard II instrument and subsequently analyzed with the software package Gwyddion [106]. More specific information on the AFM technique can be found in Ref. [102, 104, 105], for instance.

Chapter 5

Results and discussion

The main results of the thesis are presented in this chapter. The central goal is to provide real-time x-ray measurements on different organic systems using a combination of state-of-the-art area detectors (see Sect. 4.7) and highly brilliant 3rd generation synchrotron radiation. Measurements were performed either in the wide-angle or in the small-angle regime, thus delivering (time-resolved) information on different length-scales. This shall demonstrate the capability and importance of real-time X-ray scattering techniques [50], particularly in the frame of organic growth. Depending on the thin-film preparation, the substrates used (exclusively wafers of native SiO_x in this thesis), and the materials involved the samples may exhibit a rather complex structural composition of different molecular phases [76]. Hence, following the growth evolution on microscopic and macroscopic length-scales not only allows for an optimization of the intended thin-film application but also to relate experimental data to available atomistic growth theories and the involved surface physics.

The organization of Chap. 5 is the following: Part I (Sect. 5.1) of this chapter focuses on real-time GID measurements on multilayer films of PFP and blended films (consisting of PFP_x:PEN_{1-x}) grown at different substrate temperatures. A key question is, in this context, the dependence of the molecular lattice on the growth temperature and a potential re-arrangement of the molecules involved. Part II (Sect. 5.2) investigates the post growth GISAXS pattern of a set of DIP samples, which differ only in film thicknesses. Here, the morphology of the samples is analyzed with theory from small angle scattering, using the form factors of a cylinder, a cone, and a truncated sphere. The results are finally compared with AFM measurements on the same sample set. Most importantly, such analysis provides the actual shape of the DIP islands and how it evolves as a function of deposited monolayers. Sect. 5.3 investigates the time dependence of the GISAXS signal of the DIP thin-films. For that purpose *in situ* measurements of the DIP thin-film growth were performed at the synchrotron source. We mainly focus on the investigation of kinetic growth aspects such as molecular diffusion and structural evolution. Part III (Sect. 5.4) uses methods, which have been introduced in the preceding sections. As a model system for a typical OPV-application (namely mixed compositions of DIP:C_{60}), we investigate how the morphology and structure depend on the choice and mixing ratio of

the materials.

5.1 Real-time GID measurements on pristine PFP and PFP:PEN blends

This section contains results, most of which are published in Ref. [33][1] and reports on real-time scattering investigations of growth of thin films of Perfluoropentacene (PFP) and its dependence on the substrate temperature, ranging between −120 °C and 60 °C. All films were grown up to 50 nm on silicon oxide. Additionally, measurements of PFP_x:PEN_{1-x} blends are presented in Sect. 5.1.4.

In recent years, significant effort has been made to investigate structural and optical properties of organic materials with potential for device applications [23, 107]. In this context, perfluoropentacene (PFP, $C_{22}F_{14}$) is a promising n-type organic semiconductor [108–112]. Relative to its hydrogenated counterpart pentacene (PEN, $C_{22}H_{14}$) [113], PFP may serve as an electron acceptor [114, 115]. In particular, shifting the HOMO/LUMO energy levels via fluorination may provide an efficient way to tailor electronic properties, such as the electron injection barrier [59, 116–121]. In the developing field of organic electronics, this offers interesting possibilities to combine such p- and n-type semiconductors either in heteroplanar [60, 122] or mixed [28, 62] structural configurations. However, while PEN has been thoroughly studied [58, 114, 123], reports on the structure of PFP are still scarce [14, 25, 63, 64, 104, 124–128].

The investigation of structure and morphology of PFP is of prime importance, since the electronic and steric compatibility with PEN offers interesting perspectives. Real-time X-ray studies have been proven to be an extremely powerful, non-invasive technique to study the growth of inorganic and organic materials [129], in particular when utilizing new detector technologies combined with high brilliance synchrotron radiation. For devices based on thin films, the degree of crystallinity significantly influences the charge carrier mobility of organic semiconductors [130]. To optimize this for possible device applications it is important to be able to tune the crystallinity of PFP, which is strongly connected to diffusion processes during growth, by changing the substrate temperature. In this section, the effect of the substrate temperature on the structure of PFP films prepared by OMBD is investigated. Generally, OMBD is a non-equilibrium and dynamic process. Molecules may reorganize even after impinging on the sample surface and transient structures may arise [13, 37, 39]. This dynamic nature already implies the need for time-resolved studies to obtain a full understanding of how different growth parameters influence the thin-film properties, structurally as well as optically or electronically [25, 64, 125, 131, 132].

One of the crucial parameters controlling the growth dynamics, which may also lead to polymorphism, is the substrate temperature [133–137]. The scope of this work is to

[1] C. Frank, J. Novák, A. Gerlach, G. Ligorio, K. Broch, A. Hinderhofer, A. Aufderheide, R. Banerjee, R. Nervo, and F. Schreiber, J. Appl. Phys. **114**, 043515 (2013): *Real-time X-ray scattering studies on temperature dependence of Perfluoropentacene thin film growth.*

follow the structural evolution of PFP thin films at different substrate temperatures, by using X-ray scattering techniques in a wide angle regime and in real-time (i.e. with a sub-mono-layer resolution) during growth. The results are complemented by atomic force microscopy (AFM) studies.

5.1.1 Growth conditions and sample preparation

The substrates were cleaned using an ultrasonic bath with acetone, iso-propanol and ultra-pure water. Purified PFP ($\geq$ 99 %) was purchased from Kanto Denka Kogyo Co. and deposited on commercial silicon oxide (SiO_x) wafers with a native oxide layer. PFP films were grown via OMBD in a portable UHV-chamber (base pressure $< 8 \times 10^{-9}$ mbar) [81]. The growth rate was approximately 3 Å/min and verified by a water-cooled quartz crystal micro-balance. The substrate temperature was changed in a wide range from −120 °C to 60 °C. A beryllium window allows entry and exit of X-rays, which facilitates following the growth in real time. Using synchrotron radiation, reciprocal space maps (RSMs) in the grazing incidence diffraction (GID) regime and post-growth scans were measured either with a point detector or with a Pilatus-II detector, *in situ* at the ID10B end station (λ = 1.0754 Å) at the European Synchrotron Radiation Facility in Grenoble. *Ex situ* samples were characterized in our in-house laboratory via AFM, X-ray reflectivity (XRR) and rocking-scans. AFM images were measured in tapping mode with a JPK Nanowizard II instrument and post processed with the free software package Gwyddion [106]. XRR and rocking-scans were measured with a GE XRD3003 diffractometer ($CuK_{\alpha 1}$).

5.1.2 Calculation of the experimental resolution

An important consideration in X-ray diffraction experiments is the influence of the resolution function on the measurements. Thus, analyzing the data without applying a proper correction can be misleading. The optimization of the experimental resolution, very often turns out to be quite challenging. For example, the resolution can be improved by choosing the x-ray wavelength λ used in the experiment. However, depending on the exposure time many organic systems may seriously suffer from beam-damage at low X-ray energies, thus influencing the growth, especially if followed in real-time. Alternatively, the sample-to-detector distance L may be increased or, additionally, smaller primary and secondary slits can be used. In this experiment, the maximum sample-to-detector distance was limited by the maximum weight load onto the detector arm, and smaller slit sizes are usually traded for a worse signal-to-background ratio. To obtain still a good estimate of the in-plane coherent island size d_s (see Sect. 5.1.3) we have to correct the real-time data of the area detector. The resolution function, as in a first approximation determined in the following, assumes that the full width at half maximum (FWHM) of the (012)-Bragg peak of the (high-resolution) post-growth obtained GID-scans (measured with the point-detector) represents the real island size of the system, i.e. accounts for "perfect" resolution. The peak width recorded with the area-detector is then corrected by de-convoluting the peak's line-profile with that obtained by the point-detector. Assuming

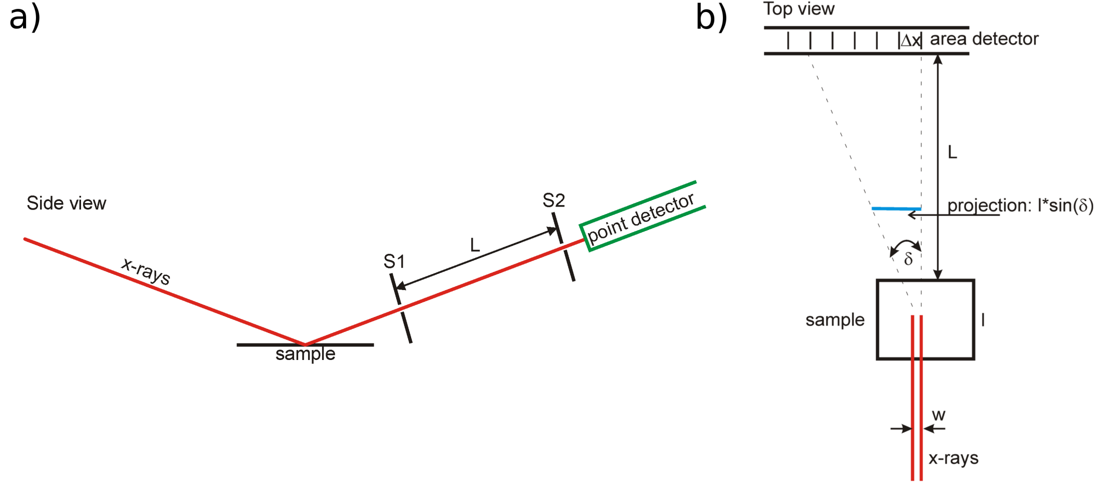

Figure 5.1: Slit configuration for the point-detector (a) and the area-detector (b).

in a first approximation that the resolution function of the point detector locally behaves like a delta-function, i.e. representing experimentally the best achievable resolution, the coherent island size in the in-plane direction is obtained via $d_s = 2\pi/\Delta q_{||}$ (see Sect. 5.1.3), where $\Delta q_{||}$ is now corrected according to

$$\Delta q_{||} = \sqrt{{\Delta q^r_{||,\mathrm{area}}}^2 - {\Delta q^r_{||,\mathrm{res}}}^2}\,, \tag{5.1}$$

with the FWHM's of point- $\Delta q^r_{||,\mathrm{res}}$ and area detector $\Delta q^r_{||,\mathrm{area}}$.

Furthermore, it is important to know the resolution limit, i.e. the maximum island-size, which can be experimentally resolved with each detector configuration for given experimental setup. Figure 5.1a shows the scattering geometry for the post growth measurements, where a point detector was used. An exact determination of the device's resolution function is often non-trivial. Instead, one can obtain a relatively precise estimation of the resolution limit using a Taylor expansion of the resolution function (parallel to the sample plane, with the in-plane scattering angle δ) in an angular range Δ, which lies in the vicinity of the respective Bragg-peak[2]

$$q_{||} = f(\delta) \Rightarrow q_{||}(\delta + \Delta) = q_{||}(\delta) + \frac{dq_{||}(\delta)}{d\delta}\Delta\bigg|_\delta + \frac{d^2 q_{||}(\delta)}{d\delta^2}\Delta^2\bigg|_\delta + \ldots \tag{5.2}$$

It follows then, that

$$\Delta q^r_{||} = q_{||}(\delta + \Delta) - q_{||}(\delta) = \frac{dq_{||}}{d\delta}\Delta\bigg|_\delta \tag{5.3}$$

[2]The estimation of the resolution limit, as provided in the following, was derived with contribution from Jiri Novák.

Using the parallel component of the wave vector transfer [97]

$$q_{||} = \frac{2\pi}{\lambda}[2 - 2\cos(\delta)]^{1/2} \ , \tag{5.4}$$

the resolution limit of the point-detector, parallel to the sample plane is then obtained via

$$\Delta q^r_{||} = \frac{2\pi}{\lambda}\cos\left(\frac{\delta}{2}\right)\Delta \ . \tag{5.5}$$

In this equation, the angular acceptance is determined by the width $s_1 = 0.3\,\text{mm}$ and $s_2 = 0.3\,\text{mm}$ of the slits and the distance $L = 340\,\text{mm}$ between them, i.e. $\Delta = (s_1 + s_2)/L = 0.0018\,(\text{rad})$. Accordingly, the experimental resolution parallel to the sample plane and in the vicinity of the (012)-Bragg peak is limited to a horizontal island size of $r_{\text{max}} = 2\pi/\Delta q_{||} = 604\,\text{Å}$ for the point detector configuration.

For the real-time measurements, i.e. the evolution of the FWHM of the (012)-Bragg reflection, a 2D area detector was used. Similarly, the resolution limit is estimated using the Taylor expansion in Eq. (5.2). Figure 5.1b shows the scattering geometry for the area-detector configuration. Here, the angular acceptance is defined by the pixel width Δx acting as a slit, the size of the beam w and the projection of the sample onto the detector (given by the sample length l and the in-plane scattering angle δ). Therefore, $\Delta = (\Delta x + \Delta B)/l$, where $\Delta B = \max(w, l\sin\delta)$. In our configuration (i.e. $\Delta x = 80\,\mu\text{m}$, $w = 0.3\,\text{mm}$, $L = 420\,\text{mm}$, and $l = 20\,\text{mm}$) the angular acceptance is $\Delta = 0.0145(\text{rad})$. The resolution limit for the area detector is estimated using Eq. (5.5), while δ has to be related to the horizontal pixel number, i.e.

$$\Delta q^r_{||} = \frac{2\pi}{\lambda}\cos\left[\frac{(\delta' \cdot \text{CPD} + x_0 - x)\pi}{\text{CPD} \cdot 360}\right] \tag{5.6}$$

In this equation δ' is the horizontal detector position, x_0 the position of the direct beam (while the detector is centered at $\delta' = \gamma' = 0$) and x the actual pixel position of the (012)-Bragg peak. In particular, with $\text{CPD} = 122\,\text{px/deg}$, $x_0 = 1610\,\text{px}$ and $x = 471\,\text{px}$ the resolution limit for the area detector is estimated at the (012)-Bragg reflection as $r_{\text{max}} = \frac{2\pi}{\Delta q^r_{||}} = 75\,\text{Å}$.

5.1.3 Results and discussion of pure PFP thin films

In post-growth AFM studies we observed that changing the substrate temperature results in very different film morphologies, see Fig. 5.2 showing AFM images of 50 nm PFP grown at 60 °C and −20 °C, respectively. At a substrate temperature of 60 °C PFP forms long needle-like crystallites several micrometers in length. The Root Mean Square (RMS)-roughness is $\sim$7 nm, i.e. relatively smooth compared to the final nominal film thickness of 50 nm. The corresponding height-distribution of the crystallites is shown in the inset of Fig. 5.2a. The distribution has a sharp maximum at a height of $z \approx 28\,\text{nm}$ and has a

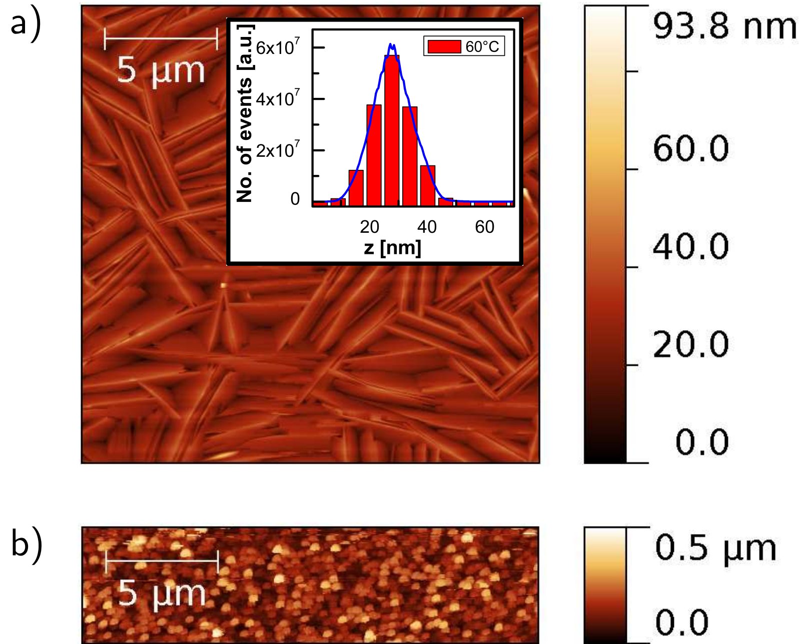

Figure 5.2: AFM images of 50 nm PFP grown at a substrate temperature of (a) 60 °C and (b) −20 °C. The images cover a scan area of $20 \times 20\,\mu\text{m}^2$ and $20 \times 5\,\mu\text{m}^2$, respectively. The inset shows the corresponding height-distributions at 60 °C.

Full Width at Half Maximum (FWHM) of $\Delta_z \approx 15\,\text{nm}$. Similar morphologies have been reported in previous studies [61,64,123], where PFP was grown either at high temperatures or close to room temperature. In contrast, for the growth at −20 °C (Fig. 5.2b) the thin film is formed by small mounds with heights up to 500 nm and diameters up to 500 nm. (Note that a smaller scan-area is shown, which does not display artifacts caused by the film morphology). The film is very jagged and a precise quantification of the film surface parameters is beyond the capabilities of the employed AFM. Hence, the AFM images already suggest a better ordering of PFP molecules in films grown at high temperatures.

5.1.3.1 Characterization of the morphology

In view of the the discussion of the AFM images in Fig. 5.2, an useful tool to characterize the surface of the PFP films (post-growth) is the height-height correlation function (HHCF). The one dimensional discrete HHCF, which is usually calculated along the fast scanning axis, can, for instance, be found in Ref. [106]

$$H_x(\tau_x) = \frac{1}{N(N-m)} \sum_{l=1}^{N} \sum_{n=1}^{M-m} (z_{n+m,l} - z_{n,l})^2 \ , \tag{5.7}$$

where l, m denote the column-, row-index and N, M the total number of columns, rows. The HHCF is a measure for the probability to find the difference in height between two

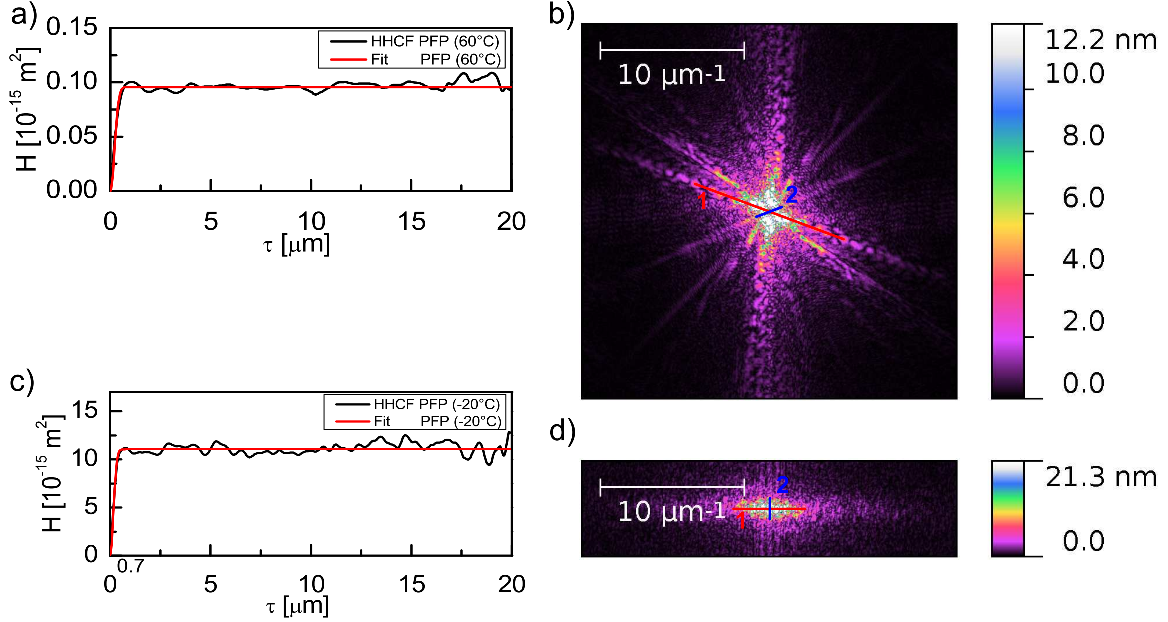

Figure 5.3: HHCF obtained from AFM-images for 60 °C (a) and −20 °C (c). 2D-FFT obtained from AFM-images for 60 °C (b) and −20 °C (d). Red and blue lines mark the length scales with the highest occurrence for the long and short crystallite axis.

points x and x', which are separated by a distance $\tau = x - x'$. Consequently, it can be used to estimate the mean island radius from the first maximum of the HHCF for circular shaped domains, which however (due to the shape anisotropy), is not a good estimate for the needle-like crystallites of PFP grown at 60 °C. More importantly, assuming a Gaussian representation the HHCF can be fitted according to

$$H_x(\tau_x) = 2\sigma^2 \left[1 - \exp\left(\frac{\tau_x^2}{T^2}\right)\right] , \tag{5.8}$$

which allows to extract the surface roughness σ and the surface correlation length T. Figure 5.3a and 5.3c show the HHCF for 60 °C and −20 °C obtained from the AFM-images in Fig. 5.2. The roughness thus statistically estimated, i.e. $\sigma = 6.9$ nm for 60 °C, is in good agreement with the RMS-roughness for the 60 °C film. It may be speculated that the corresponding surface correlation length $T \simeq 291$ nm is determined by the periodicity of the PFP-needles. Although, the HHCF of the −20 °C film is for the sake of completeness shown in Fig. 5.3c as well, the large jaggedness of the surface prevents a similar analysis, i.e. the parameter obtained from the HHCF are not reliable. Figure 5.3b and 5.3c show the modulus of the 2D-fast Fourier transform (FFT) for 60 °C and −20 °C, which are representative of a reciprocal space image. Measuring the highest occurrence of the smallest and largest length-scale within the images (indicated by the blue and red lines) allows to estimate the average size of the long and short axis of the crystallites. For PFP grown at 60 °C it is then found that the average diameter of the long crystallite axis

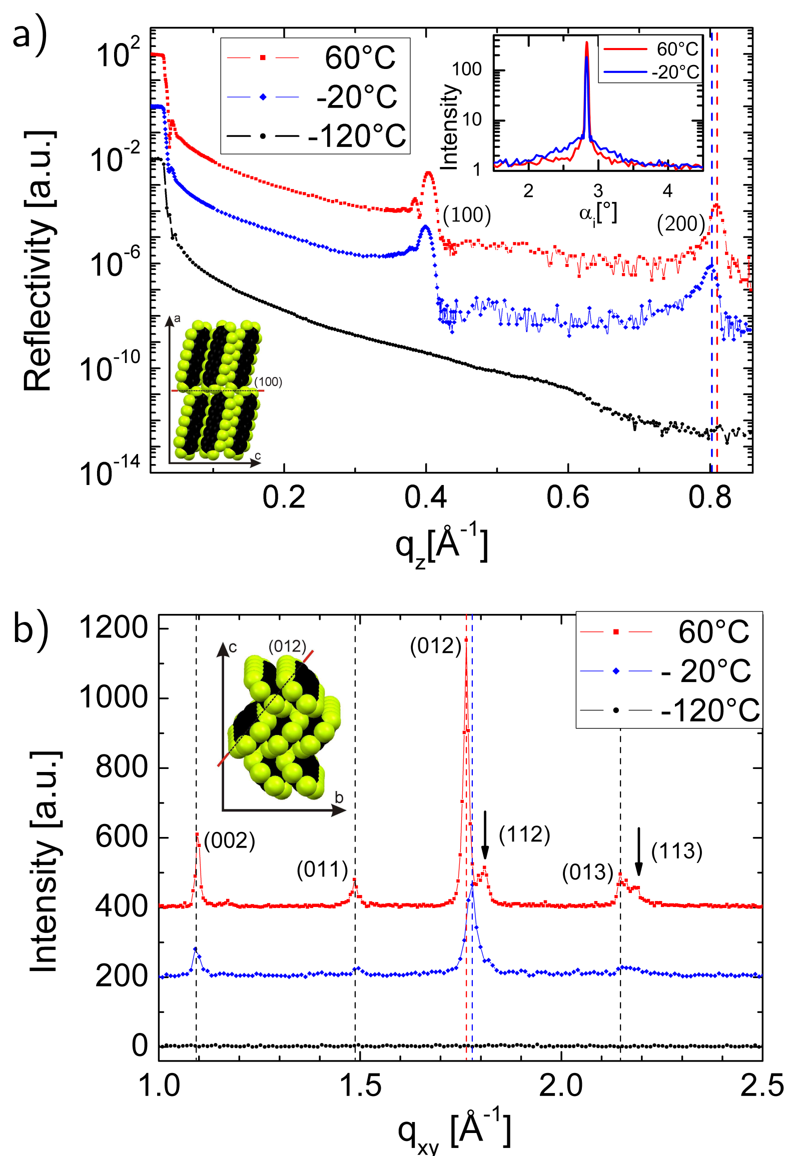

Figure 5.4: (a) XRR-scans of PFP grown at 60 °C (red), −20 °C (blue) and −120 °C (black). Additionally, rocking scans were performed on the (100)-Bragg reflections. (b) GID-scans of PFP grown at 60 °C (red), −20 °C (blue) and −120 °C (black). XRR- and GID-scans are vertically shifted for clarity in (a) and (b). The molecular packing of PFP is shown as an inset in perpendicular (a) and parallel (b) direction to the sample surface. (100) and (012) scattering planes are indicated with dashed lines.

is $d_l \simeq 2.47$ μm and of the short axis $d_s \simeq 0.37$ μm. In contrast, for $-20\,°$C, it is observed that $d_l \simeq 0.88$ μm and $d_s \simeq 0.69$ μm, i.e the circular shaped geometry of the PFP-islands, grown at low temperatures is mirrored in the 2D-FFT image.

5.1.3.2 Post-growth analysis of the molecular structure

The out-of-plane film structure can be characterized by XRR. Figure 5.4a shows XRR-scans of two 50 nm PFP *ex situ* samples, which were grown at substrate temperatures of 60 °C (red) and -20 °C (blue), respectively. For both temperatures, Bragg reflections ($h00$) up to the 2nd order can be observed. The indexing throughout the thesis is chosen in compliance with Ref. [58], which means that the long molecular axis is assigned to axis a (see bottom left inset of Fig. 5.4a). Note that at a substrate temperature of -120 °C no Bragg reflections are found. For 60 °C well pronounced Kiessig- and Laue oscillations are observed. From the respective periodicities the total and the coherent film thickness are estimated to be $D_{tot} = 566 \pm 36$ Å and $D_{coh} = 402 \pm 18$ Å. The out-of-plane lattice spacing is derived in the following from the second order Bragg peak including a refractive correction for the PFP-layer.

The lattice parameter $a = 15.52 \pm 0.02$ Å, agrees well with that of the PFP single crystal phase, reported by Sakamoto et al. [58]. For growth temperatures of -20 °C Kiessig- and Laue-oscillations are rapidly damped due to the higher roughness of the film. The out-of-plane lattice parameter is $a = 15.70 \pm 0.02$ Å, i.e. we observe a change in the lattice parameter by $\Delta a \approx 0.2$ Å compared to 60 °C. This increase of the lattice parameter upon decreasing the substrate temperature obviously implies a slight rearrangement of the molecular packing.

The in-plane film structure is explored by GID-scans performed post-growth with a point detector for low and high temperatures. For -20 °C and 60 °C (see Fig. 5.4b) the observed in-plane Bragg-reflections are close to the reported thin-film structure [64]. The absence of in-plane Bragg reflections for -120 °C is consistent with amorphous film growth of PFP at very low temperatures. Comparing the in-plane peak positions in Fig. 5.4b for 60 °C and -20 °C (see dashed lines) we observe a peak-shift in the [012]-direction. Decreasing the temperature obviously leads to a shift of $\Delta(012) = 0.016$ Å^{-1}, which corresponds to a lattice expansion of $\Delta_d = 0.032$ Å in the [012]-direction. Close to the (012) and (013) Bragg reflections two peaks (marked by arrows), are observed for 60 °C. We attribute these peaks to the projection of the (112)- and (113)-Bragg reflections onto the q_{xy} plane.

A better understanding of growth mechanisms can be obtained by taking advantage of the most recent detector technology with high dynamic range, high signal-to-noise ratio and faster acquisition and read-out times, which provides unprecedented spatial and temporal resolution. *In situ* RSMs were taken during growth and post-growth in the GID-regime. Post-growth RSM images are shown in Fig. 5.5a and Fig. 5.5b for the substrate temperatures 60 °C and -20 °C. Note that at -120 °C (Fig. 5.5c) no diffraction peaks are visible, similar to the XRR/GID-scans. At 60 °C well-defined crystal truncation rods (CTRs) are observed for all diffraction orders hkl. In contrast, CTRs are broader

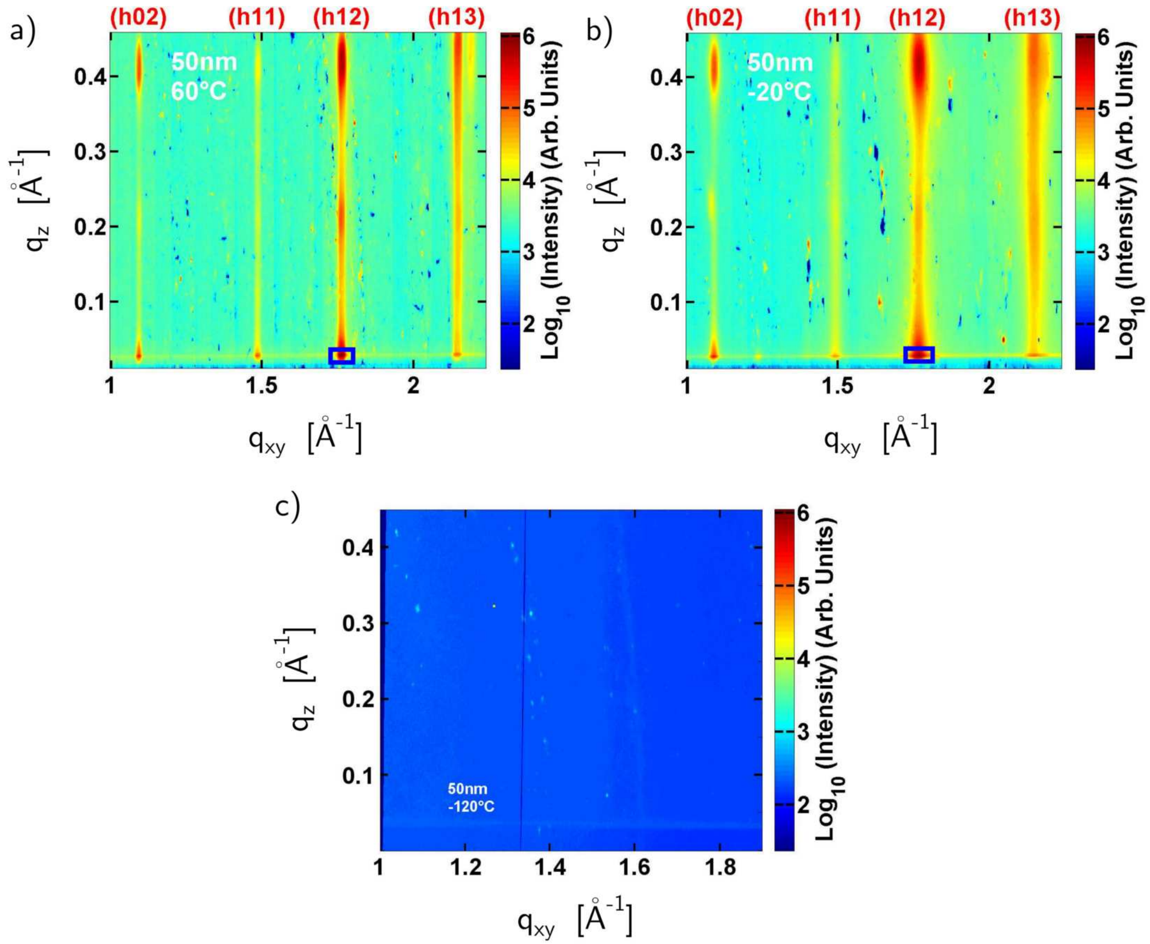

Figure 5.5: (a) RSM of 50 nm PFP grown at a substrate temperature of 60 °C. (b) RSM of 50 nm PFP grown at a substrate temperature of −20 °C. Blue rectangles mark the (012) Bragg reflection, which is used for the real-time data analysis. (c) RSM of 50 nm PFP grown at a substrate temperature of −120 °C. No noticeable diffraction features are present at this temperature. Note, that the same color scaling is used in (a–c)

and more diffuse at −20 °C. This suggests that at low temperatures the projection of the coherent scattering volume onto the sample surface is smaller. Furthermore, the absence of diffraction rings for both temperatures indicates that PFP-molecules grow in a 2D-powder structure on SiO_x-substrates. This is confirmed by rocking-scans, which are taken on the first Bragg reflection (see top right inset in Fig. 5.4a). At both temperatures a similar mosaicity is observed but with a higher diffuse background at low temperatures. PFP exhibits a high degree of crystallinity perpendicular to the sample surface when it is grown on SiO_x at elevated substrate temperatures. This is evident from our measurements here and also corroborates earlier studies [64]. However, the fact that the structure is also crystalline even at a temperature as low as −20 °C was not reported earlier and is established in this study.

At 60 °C, surprisingly, a series of weak $(\frac{1}{2}kl)$ diffraction peaks is observed (Fig. 5.5a). Evaluating their positions along the q_z-rods (see Fig. 5.5c for the $(h12)$- and $h02$-rod), results in $q_z = 0.211\,\text{Å}^{-1}$, i.e. half the q_z-value of the first order Bragg reflections. Therefore, we conclude that a coexisting phase with a unit cell two times larger along the a axis than the dominating PFP thin-film phase [64, 123] (with two molecules per unit cell) nucleates. This indicates that two molecules are arranged along the a axis of the unit cell, as was also observed e.g. for poly(p-phenyl)oligomers [138]. In contrast, at −20 °C the $(\frac{1}{2}kl)$ diffraction peaks are weaker (see also Fig. 5.5c). We speculate that the phase with the long axis doubled is on the one hand energetically more favored and its nucleation is on the other hand thermally activated. Thus, it is not present at low temperatures. In addition, at both substrate temperatures we observe a CTR next to the $(h13)$-rod, which to our knowledge has not been reported yet. Note that line scans of the $(h11)$ and $(h13)$ CTR's are shown in Fig. 5.6. The evolution of the in-plane grain size is of significant interest, because in previous studies it was observed that the ordering behavior of organic materials can be very different in the in-plane and the out-of-plane direction [29].

5.1.3.3 Real-time analysis of the in-plane structure

For the real-time data analysis, we have taken series of RSM-images *in situ* at −20 °C and 60 °C during the film growth with sufficient time resolution, i.e. the time between two images corresponds to ∼0.5 ML (mono-layer). Focusing on the in-plane information we restrict ourself to the (012)-diffraction peak, which is the strongest in-plane reflection with the best signal-to-noise ratio. Using the stronger (112)-reflection would also be possible, but in this case we would have a considerably large q_z-component, thus yielding a superposition of in-plane and out-of-plane information. For the following analysis, intensities are integrated within a region-of-interest (ROI), which is defined around the (012)-Bragg reflection (indicated by blue rectangles in Fig. 5.5).

Figure 5.7a shows the integral intensity plotted as a function of the nominal film thickness. At 60 °C the intensity increases linearly, which indicates the virtually ideal poly-crystallinity of PFP grown at high substrate temperatures. In contrast, at −20 °C the intensity increases in a non-linear fashion and starts to saturate at the film thickness of ∼20 nm. Obviously, there are more crystal defects at low temperatures leading to a

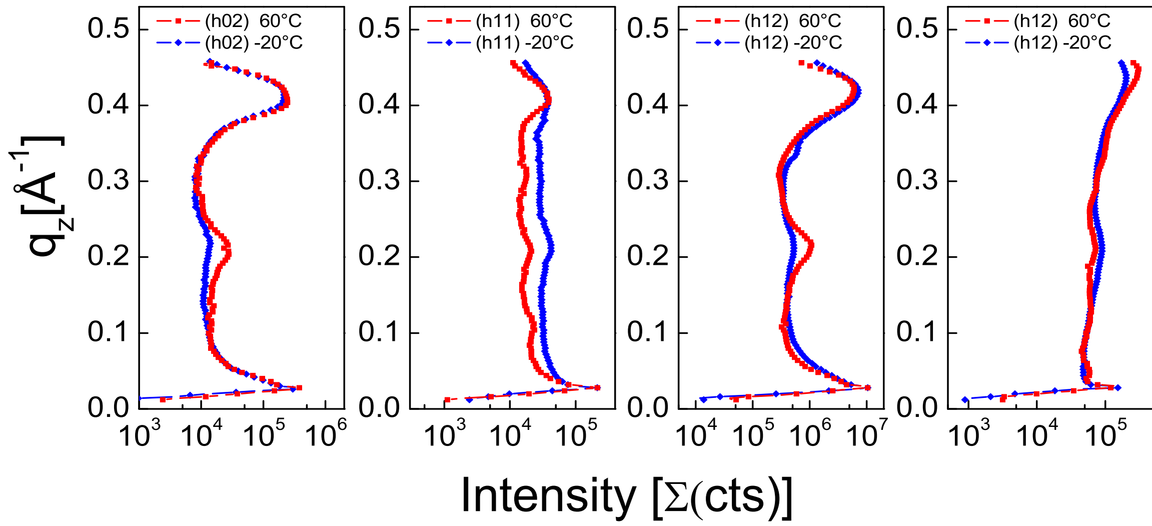

Figure 5.6: Line-scans (integration along q_{xy}-direction) extracted from the post growth RSM images for 60 °C and −20 °C (Fig. 5.5a and Fig. 5.5b), which show the diffuse intensity in the vicinity of the $(h02)$ and $(h12)$ CTRs. At 60 °C a diffraction peak is observed most evidently at $(\frac{1}{2}12)$, which nearly disappears at −20 °C. Note that the intensities of the 60 °C and −20 °C line-scans as well as the RSMs were normalized to a common maximum.

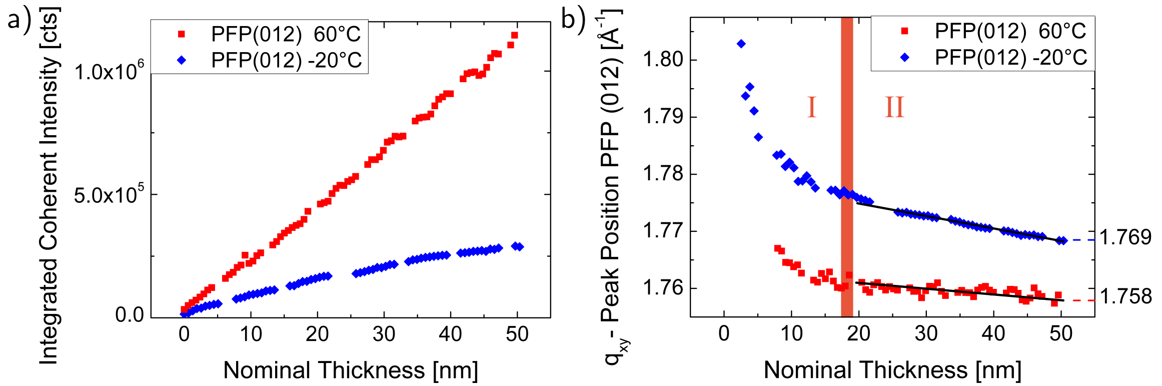

Figure 5.7: (a) Integrated intensity of the (012)-Bragg reflection, plotted against the nominal film thickness for 60 °C (red) and −20 °C (blue). (b) Position of the (012) diffraction peak plotted against the nominal film thickness for 60 °C (red) and −20 °C (blue). Fitting of the peak position was not possible at the initial stage of growth as the signal-to-noise ratio was too low. Black lines indicate the tentative trend of the temporal evolution in regime II.

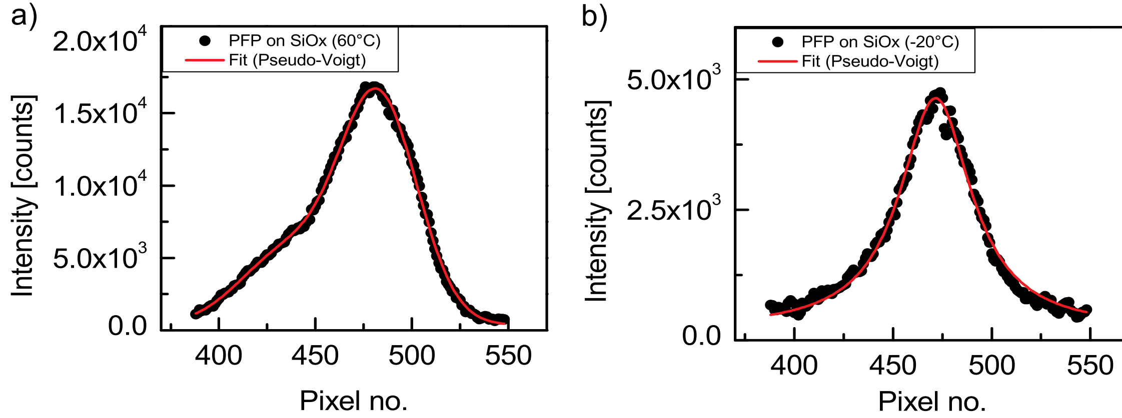

Figure 5.8: RSM images were integrated in the vicinity of the (012)-Bragg peak along q_z ($\simeq$ 15 pixel) to follow the peak evolution. (a–b) show the raw-data (intensity as function of pixel number) of the CCD-images for 60 °C and −20 °C together with the applied Pseudo-Voigt fit for the final film-thicknesses of 50 nm. Note that due to the orientation of the CCD-detector the peaks are vertically mirrored in comparison with the GID data (see Fig. 5.4), which was measured with a point-detector.

decrease of the coherent scattering crystal size parallel to the substrate plane. Additionally, at −20 °C there may well exist an amorphous fraction of material, which does not contribute to the coherent scattering. Therefore, resulting in a film thickness dependent loss of scattering intensity.

To gain real time information on grain size and lattice spacing we integrate intensities within the ROI along the q_z-direction to obtain a line scan with intensity as a function of q_{xy}. For both temperatures such line-scans were fitted with a double pseudo-Voigt profile (see Fig. 5.8), which was applied, to take the influence of the (112)-diffraction peak at 60 °C into account. From the fits the position of the peak as well as the FWHM were obtained. The evolution of the peak position as a function of nominal film thickness is shown in Fig. 5.7b. At both temperatures two regimes can be distinguished. The early stage of the growth, labeled as regime I, corresponds to a nominal film thickness of $d \approx 0-19$ nm (i.e. $d \approx 0-12$ ML). At this stage the (012)-diffraction peak shifts rapidly in a nonlinear fashion towards smaller q_{xy}, which means that for thin films of PFP, i.e. up to $d \approx 12$ ML, a significant relaxation of the lattice occurs. Regime II characterizes thicker films of PFP ($d \approx 19-50$ nm). At both temperatures the change of the lattice parameter is now linear and (as indicated by black lines in Fig. 5.7b) much slower. Additionally, it is observed that at 60 °C the peak shift is smaller than at −20 °C. This signifies

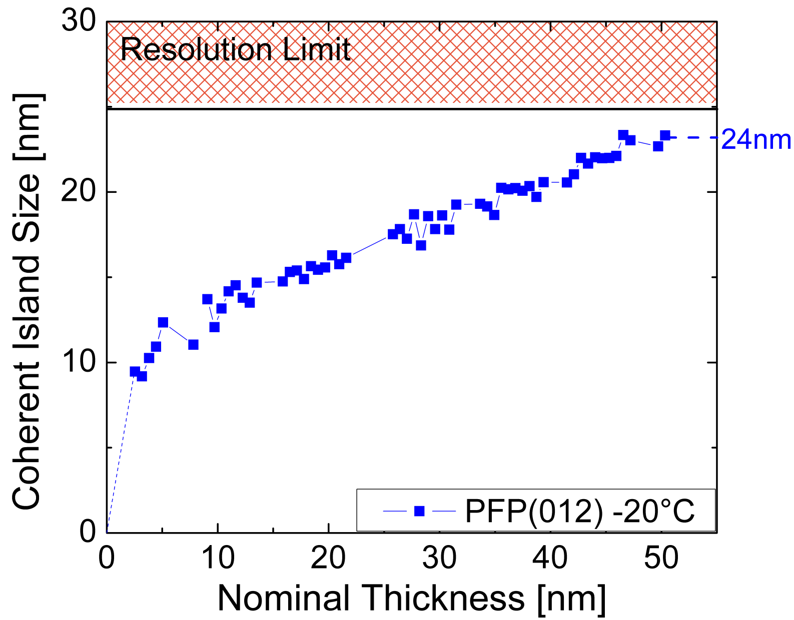

Figure 5.9: Evolution of the in-plane coherent island size in [012]-direction as a function of nominal film thickness for −20 °C.

that for PFP grown at 60 °C a relevant relaxation of the lattice takes place only until a critical film thickness of approximately 12 ML, in contrast to a substrate temperature of −20 °C. For thicker high temperature PFP films no significant modification of the lattice is expected. The final difference of the lattice parameter in [012]-direction between both highlighted temperatures is $\Delta q_{xy} = 0.011\,\text{Å}^{-1}$, which corresponds to a real space expansion of $\Delta d = 0.022\,\text{Å}$. Within the experimental resolution this agrees well with the temperature related shift of the (012)-Bragg reflection observed in the post-growth GID-scans (see Fig. 5.4b). The evolution of the coherent island size d_s in the in-plane direction (see Fig. 5.9) is obtained via the Scherrer-formula, i.e. $2\pi/\Delta q_{xy}$, where Δq_{xy} was corrected for the resolution function (see Sect. 5.1.2):

$$\Delta q_{xy} = \sqrt{\Delta q_{CCD}^2 - \Delta q_{res}^2}$$

Here, Δq_{CCD}^2 is the FWHM, which is obtained by fitting the (012)-peak in the RSMs and Δq_{res}^2 is the FWHM of the resolution function.

At −20 °C the in-plane coherent island size evolves very fast during the deposition of the first 5 nm. Subsequently, the island size increases linearly until a final size of $d_s = 24$ nm is reached. Since the experimental resolution limits the determination of the in-plane-island size to $d_s \approx 25$ nm, we were not able to follow the evolution at the high substrate temperature. However, by analyzing the 60 °C post-growth GID-scan the final island size is determined to be $d_s \approx 44$ nm. Therefore, we conclude that for high temperature PFP growth, islands evolve in-plane in [012]-direction rapidly, i.e. within a few ML, to a size beyond 25 nm.

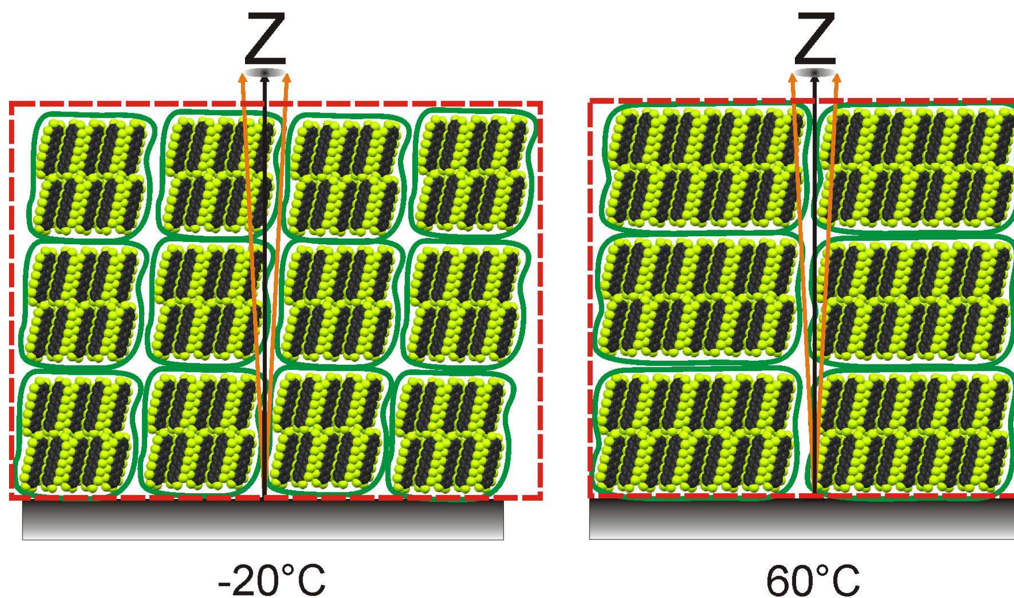

Figure 5.10: Suggested growth of PFP-crystallites at −20 °C (left) and 60 °C (right). The scattering volume is indicated by a dashed red line. Due to smaller crystallite sizes at −20 °C we expect a larger amount of domain boundaries (green lines) lying within the scattering volume. The possible occurrence of an amorphous fraction of material is not shown in the sketch.

Combining these results, we suggest a temperature dependent structure of PFP thin films as proposed in Fig. 5.10. At low temperatures the surface diffusion of molecules is limited. This leads to the formation of dislocations in the lattice resulting in smaller crystallites. As the film grows the lattice experiences a strong relaxation, i.e. structural re-arrangement of molecules until a critical thickness of approximately 12 ML is reached. Subsequent ML rearrange in a much more facile way. Crystallites are defined by grain boundaries, which on the one hand decrease the coherent scattering volume and on the other hand increase the contribution of diffuse scattering. Therefore, the final film is composed of relatively small crystallites exhibiting a low crystalline order in the in-plane direction. At elevated substrate temperatures the diffusion is stronger. Therefore, less dislocations are incorporated in the lattice resulting in larger crystallites. The crystallinity is significantly enhanced in the in-plane direction, i.e. better long-range order compared to low temperatures. The relaxation of the lattice is much weaker and beyond a critical thickness molecules barely re-arrange.

5.1.4 Results and discussion of PFP:PEN blends

This subsection contains yet unpublished results, which were measured at the ID3 beamline at the ESRF, Grenoble. Due to the limited available time at this beamtime we were only able to prepare PEN_2:PFP_1 and PEN_1:PFP_2 samples at $T_{sub} = 60$ °C.

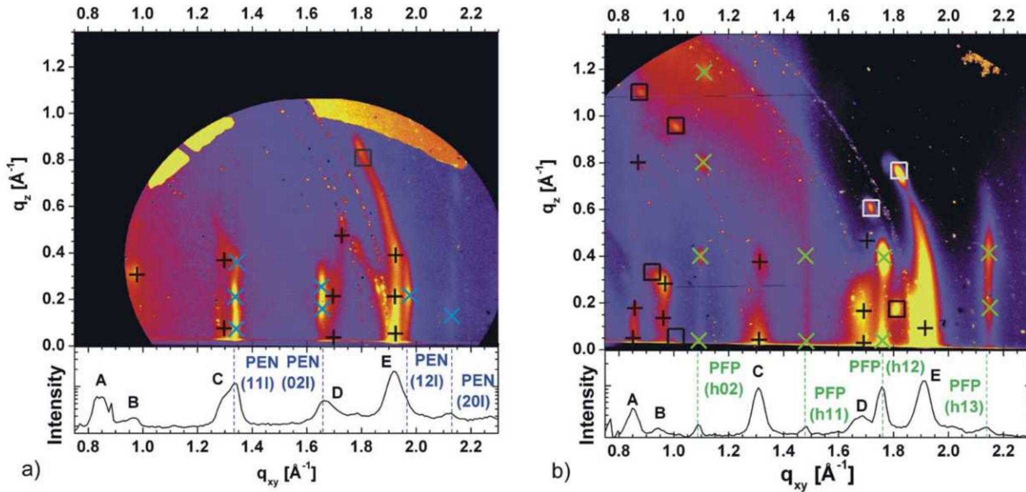

Figure 5.11: RSM of the PEN_2:PFP_1 sample (a) and the PEN_1:PFP_2 sample (b) measured post growth. Symbols indicate the different phases: pure PFP (green "x"), pure PEN (blue "x"), mixed PFP:PEN σ ("+") and mixed PFP:PEN λ ("□"). Bottom figures in (a) and (b) show the corresponding GID scans recorded with a point-detector. Note, that Fig. 5.11 was taken from Ref. [28] in order to indicate at which positions the ROI's have been placed to extract the real-time information of the different phases.

In order to analyze the structural evolution of the PFP:PEN thin film blends, Fig. 5.11 was taken from Ref. [28], in which the post-growth measurements of this experiment were already published. Accordingly, the preparation of the samples used in this section as well as the experimental setup and the growth parameters follow the procedure described in Ref. [28]. Figure 5.11 shows the post-growth reciprocal space map (RSM) of a PEN_2:PFP_1 and PEN_1:PFP_2 mixture. As indicated by the images one observes the simultaneous occurrence of the mixed σ- and λ-phases along with the thin-film phase of the pristine excessive molecule. Thus, we emphasize the observation from Ref. [28] that the growth of the λ orientation of the mixed phase results in a rather textured ring, whereas the σ-phase exhibits crystal truncation rods.

In this subsection we aim to complement the post-growth findings from Ref. [28] with our real-time analysis by investigating the thickness dependent evolution of the different phases. More precisely, not only the image after completion of the growth but rather the whole image series was processed. For the data analysis ROIs were placed at the positions were the σ- and λ-phases scatter in the RSM, i.e. for the σ-phase at $q_{xy} \approx 1.78\,\mathrm{nm}^{-1}$ ("x") and for the λ-phase at $q_{xy} \approx 1.8\,\mathrm{nm}^{-1}$ ("□"). It turned out that a quantitative analysis based on the footing of the previous section (where pristine PFP was investigated) is rather challenging. This comes from the fact that due to the similar unit cell parameters of the different structural orientations the features in the RSM overlap indistinguishably, particularly at low q_z-values. Therefore, only the evolution of the integrated intensities within the ROIs of the respective orientations were analyzed as a function of film thickness in Fig. 5.12. Surprisingly, we find that only for the mixture with an excess of PEN

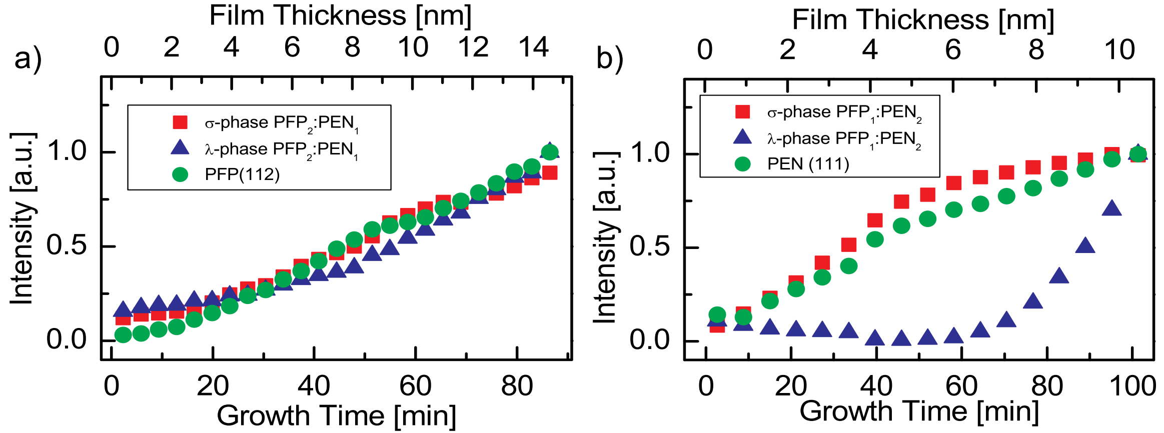

Figure 5.12: Intensity evolution for PFP_2:PEN_1 (a) and PFP_1:PEN_2 (b) grown at $T_{\text{sub}} =$ 60 °C. For both mixing ratios the time evolution of the σ- and λ-phase (of the mixed structure) are compared with respect to the pure excessing materials.

the nucleation of the λ-phase is significantly delayed. This actually, corroborates the experimental observation from Ref. [28] that PFP:PEN mixed films with an excessive amount of PEN material show a weaker scattering contribution from the λ-phase. In fact, for such films and below a thickness of $\simeq$ 6 ML we have no indication that the λ-phase nucleates at all. Therefore, we may speculate that the presence of pure PEN crystallites hinders the nucleation of the mixed λ-phase leading then to a weaker scattering signal as compared to the PEN_1:PFP_2 sample.

5.1.5 Summary and conclusion

This study gives an account of the temperature dependent structure and morphology of PFP thin films with thicknesses up to 50 nm prepared by OMBD on SiO_x-substrates. At growth temperatures of 60 °C, lying needle-like crystallites, several microns in length, are formed composed of smaller grains with an average size of 44 nm. Interestingly and so far unreported, a crystal phase containing four molecules per unit cell is observed. In contrast, at growth temperatures of −20 °C thin films are composed of mounds of diameter and height ∼500 nm. The final grain size is reduced to 22 nm. At growth temperatures of −120 °C we observe a fully amorphous film growth. A compression of the lattice parameters in the in-plane direction ($\Delta d/d$ (012) = 0.91 %) and their dilatation in the out-of-plane direction ($\Delta a/a$ (h00) = 1.29 %) is observed between growth temperatures of −20 °C and 60 °C.

Real-time *in situ* studies provide evidence for different kinetics of grain formation for low and high temperatures. In particular, for the pristine PFP films we suggest a growth model where the crystallinity in the in-plane direction is affected by the substrate temperature whereas in the out-of-plane direction it does not depend significantly on the temperature.

For the two mixtures it turned out that a quantitative data analysis is not so easy due to the overlap of the standing and the lying phase in the RSM. Thus, one can not clearly distinguish between those features, except at high q_z values, where the in-plane and the out-of-plane information of the crystal structure are however twinned. Therefore, we have only analyzed the evolution of the respective intensities. This leads to the important observation that the nucleation of the λ-phase is significantly delayed for films with an excessive amount of PEN.

Since the crystalline order is strongly connected to electronic transport properties, tuning the substrate temperature together with the film thickness may therefore be considered as a promising method to tailor the structure in device applications.

5.2 Post-growth GISAXS measurements on pristine DIP

The results of this section are taken from Ref. [30][3].

The investigation of growth processes and related changes in the interface morphologies are extremely relevant in many scientific areas. One of the ideally suited experimental methods to study the kinetic effects involved, such as surface diffusion, island condensation, and island nucleation [36, 139], all of which are inherently connected with the growth process itself, is x-ray scattering [25,64,140]. Particularly, diffuse scattering techniques [141–143] have widely been employed to decipher such processes. Apart from the surface correlations [144–146], *in situ* studies allow to monitor the growth and the evolution of the surface morphology in real time [31, 147–149].

In contrast to grazing incidence diffraction (GID), where the in-plane lattice planes of the crystallites are probed [33] on a molecular level, grazing incidence small angle x-ray scattering (GISAXS) provides access to length-scales ranging from several tens of nanometers to $\simeq 1\mu$m [98,100]. Therefore, among the prevalent off-specular scattering techniques GISAXS is the ideal tool to characterize the morphology of the sample, while simultaneously yielding a complete and non-invasive, statistical averaging of the surface (within the limits of the transverse coherence length of the x-ray beam) [150–152]. However, a quantitative analysis of the GISAXS data from island sizes, island-island correlations, and island shapes can require a significant computational and numerical effort. Although such kind of analysis has successfully been employed for well-ordered inorganic 2D structures [153], a generalization to organic materials, particularly to those with steps in the morphology and with shape anisotropy on the molecular level, is to our knowledge, still lacking. In this study we model our GISAXS data using the inverse Fourier transform of different island form factors.

As a representative material for rodlike organic semiconductors we use diindenoperylene

[3] C. Frank, R.Banerjee, M. Oettel, A. Gerlach, J. Novák, G. Santoro, and F. Schreiber, **submitted to Phys. Rev. B** (2014): *On the analysis of of island shape evolution from diffuse x-ray scattering of organic thin films and the implications for growth.*

(DIP, $C_{32}H_{16}$) [19,154–156], which is a crystalline small-molecule with significant potential for optoelectronic devices [8, 130]. Due to the large hole mobility [130] and ambipolar charge carrier transport in donor:acceptor blends [70], DIP is considered as a material of choice for the design and construction of organic semiconductor (OSC) applications. However, the intrinsic (rodlike) shape anisotropy of the molecule gives rise to a very complex growth. For instance, in the combination with different materials, which however is a prerequisite for working OSCs, there can either be a thickness dependent kinetically limited phase separation (in the case of a phase separating system) [32], or a mixing induced anisotropic correlation (in the case of an intermixing system) [29].

Inter alia, connected with the DIP thin film growth are the complicated growth mechanisms offering manifold facets and aspects of growth processes and diffusion mechanisms. These comprise post-growth structural reorganization [66,67,157], rapid roughening of the sample surface [68] and potentially, competing phases of the crystal structure [26,65,158]. Yet, studies, which investigate the DIP growth, primarily by the means of diffuse scattering techniques are very scarce [31, 159].

Here, we provide a combined GISAXS and atomic force microscopy (AFM) study on a set of *ex situ* samples with film thicknesses covering the first few monolayers, which represent the initial stages of the growth. Using a theoretical description from small angle scattering, we model our data with the form factor in the Born approximation (BA), taking different island shapes into account. The Born approximation form factor can provide a good approximation when both, the incident angle and the exit angle are higher than the critical angle. In this angular regime the dominant term of the distorted wave Born approximation (DWBA) corresponds well to the BA and multiple scattering and absorption effects can be neglected [97, 160]. For computational efficiency in the island shape fits, we have solved the Hankel transform for the in-plane component of the momentum transfer using the logFFT algorithm. Subsequently, we compare the estimated island size with that, obtained from AFM measurements. Our results are qualitatively corroborated by Ref. [31], in which the growth kinetics and the nucleation behavior of ultra-thin films of DIP were investigated in real-time, thus allowing for the determination of the mean island size and the molecular diffusion in the very first layers.

Based on our results, we finally suggest a model on how the average shape of the islands changes in the respective layers as the growth progresses. We emphasize that our experimental strategy as well as our approach for the data analysis should be equally applicable to other systems with evolution of islands during growth.

5.2.1 Growth conditions and sample preparation

Using an ultrasonic bath, the SiO_x substrates were cleaned with acetone, iso-propanol and ultra-pure water. DIP (see Fig. 5.13) was purchased (with gradient sublimation purity) from the Institute für PAH Forschung (Greifenberg, Germany). Samples were prepared in UHV conditions using the OMBD technique akin to the procedure described, e.g. in Ref. [13, 23, 37, 64, 81].

To be able to perform a consistent and thorough data analysis, several DIP sam-

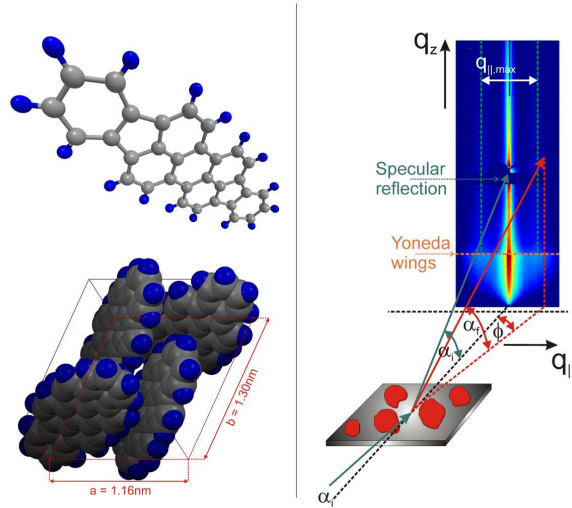

Figure 5.13: Left panel: (top) Single DIP ($C_{32}H_{16}$) molecule shown from a perspective view and (bottom) DIP molecules (at 298 K) arranged in the unit cell with the view along the c*-axis. The atom positions were taken from Ref. [26]. Right panel: GISAXS scattering geometry. The specular reflection is shielded with a beamstop, while the diffuse intensity, which is caused by the surface roughness, is recorded in the reciprocal space map (RSM) as a function of the exit angle α_f and the in-plane angle ϕ.

ples were grown with film thicknesses (or equivalently total film coverages) ranging from $\sim$0.5–5.5 ML. Notably, to obtain a strong diffuse scattering intensity we have chosen the respective layer coverages of the films in fractions corresponding to half a monolayer [31]. The growth rate for this sample series was set to $R_{\mathrm{growth}} \approx 0.1$ nm/min and the substrate temperature was fixed to $\simeq 25$ °C.

In order to investigate how the in-plane morphology of DIP changes as a function of deposited material, GISAXS measurements (see Fig. 5.13 for schematic) were performed at the P03 MiNaXS beamline [161–163] at the PETRA III storage ring, DESY, which is ideally suited to measure long-range in-plane correlation lengths. In the experiment, the detector-to-sample distance was 4.9 m and a Pilatus 300K detector with a pixel size of $172 \times 172\,\mu\mathrm{m}^2$ was used. During the measurements the incidence angle was set to $\alpha_i = 0.39°$ and a wavelength of $\lambda = 1.0868$ Å was employed. For each of the samples 51 frames were recorded with a measurement time of one second per frame and subsequently binned to one image. Our AFM measurements were performed in non-contact mode on a JPK Nanowizard II instrument. The AFM data analysis was performed using the software Gwyddion [106].

5.2.2 Results and Discussion

In view of the discussion above, reciprocal space maps of the DIP samples are analyzed to determine how the morphology changes with respect to the film thickness.

5.2.2.1 Discussion of the reciprocal space maps

Although, in principle AFM gives similar information as GISAXS, there are situations were the AFM technique is not ideal. Apart from the fact that the AFM is primarily a local probe and the images obtained are not necessarily a true representative of the average topography, there is always the risk of tampering the top organic layers particularly, when measurements have to be performed *in situ* at a sufficiently short time scale [31]. Therefore, in order to test the applicability of our method in real-time the data analysis is first tested under conditions, which can be compared to AFM. Accordingly, we employ GISAXS as the main technique in this study.

Figure 5.14 shows the GISAXS signal as reciprocal space maps (RSM) for the binned images covering a film thickness between 0.5–5.5 ML. The position $q_{z,c}$ of the Yoneda wing [144] was extracted and translated into the critical angle α_c according to

$$\alpha_c = \sin^{-1}\left(\frac{q_{z,c}\lambda}{2\pi} - \sin\alpha_i\right) , \tag{5.9}$$

leading to $\alpha_c(\mathrm{SiO_x}) \approx 0.163°$ and $\alpha_c(\mathrm{DIP}) \approx 0.15°$ (see also Ref. [12, 159]. Note that (neglecting absorption) the penetration depth [97] is given by $z_{1/e} = \lambda/(4\pi\alpha_c)$. Therefore, under the specular condition of reflection, i.e. where $\alpha_i = \alpha_f = 0.39°$ and correspondingly $q_z = 0.79\,\mathrm{nm}^{-1}$, the penetration depth of the incoming wave is of the order of ~5000 Å, resulting in a full penetration of the thin organic layer.

A further prominent scattering feature in GISAXS experiments is the presence of side streaks along the q_z-direction in the RSM. These (in the following called) “correlation streaks” point to a certain in-plane correlation length, which is caused by lateral roughness modulations in the morphology of the sample. In all of the images of Fig. 5.14 we find two such streaks at different $q_{||}$-positions symmetrically located around $q_{||} = 0$. It is observed that the $q_{||}$-positions of the streaks strongly depend on the film thickness. In particular, we find that for larger thicknesses the separation between the two streaks decreases. Since we are mainly interested in the in-plane component of the momentum transfer, line profiles were extracted from the images in Fig. 5.14. By choosing a suitable region of interest (ROI) as indicated by the red box in Fig. 5.14a, in which the intensity was integrated along the q_z-direction (in the range $q_z = 0.88 - 0.94\,\mathrm{nm}^{-1}$) we get the horizontal GISAXS sections only as a function of $q_{||}$ as shown in Fig. 5.14f for the different film thicknesses.

For small thicknesses the samples exhibit a very pronounced central peak at $q_{||} = 0$. Due to the increasing film roughness, which usually occurs during the deposition of more DIP material [68], this peak gradually decreases and is finally masked by the approaching correlation peaks. Importantly, and relevant for the analysis in the following sections, we find that the correlation peak position in the line profiles (or correlation streaks in the RSM) do not show any dependence on q_z. This is observed for all thicknesses and is illustrated in Fig. 5.15 for the respective samples. As a consequence, the horizontal line profiles can be extracted at arbitrary q_z-positions within the GISAXS images, while still containing enough information (particularly, at q_z-positions well above the Yoneda

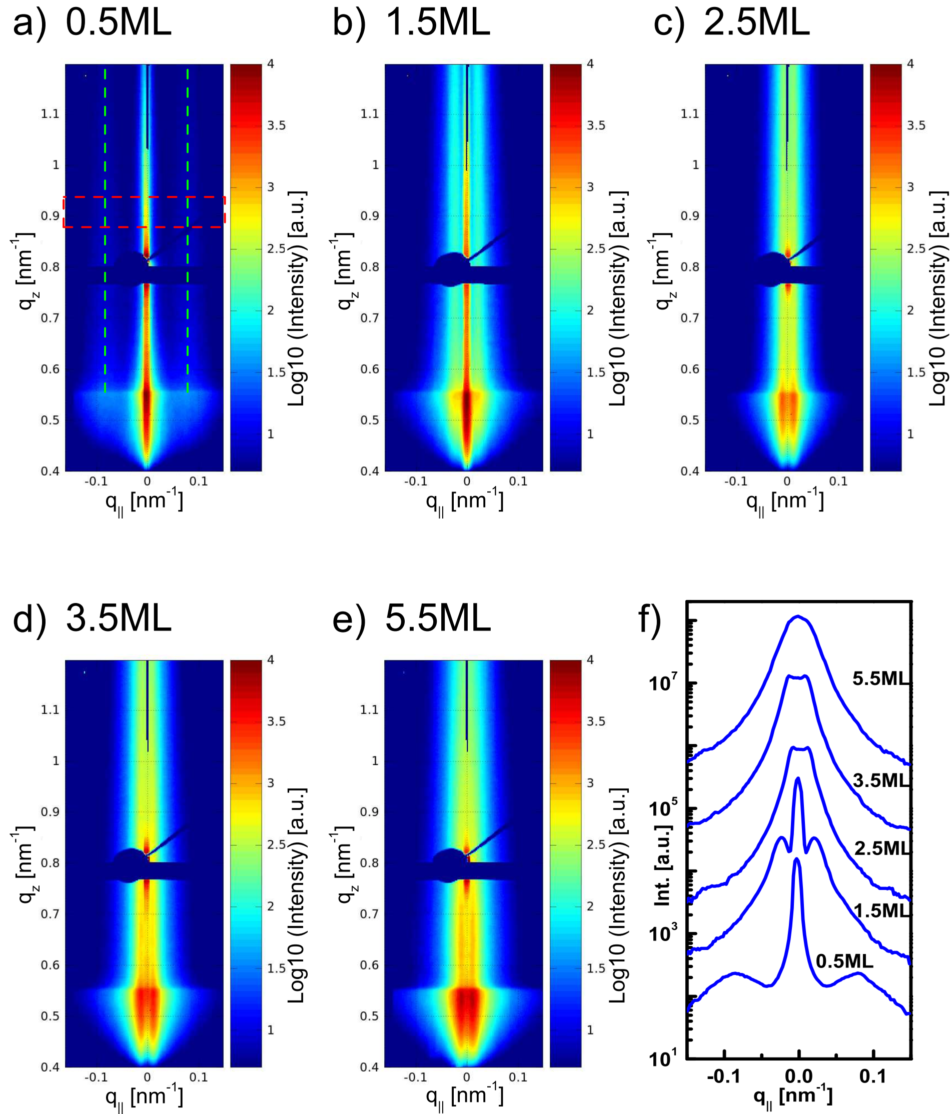

Figure 5.14: (a-e) GISAXS signal of ultra thin films of pure DIP grown on native SiO_x substrates. The film thickness covers a range of 0.5–5.5 ML. The dark blue horizontal stripe corresponds to the non-sensitive inter module detector gaps, while the dark circle corresponds to the specular beamstop. Green dashed lines in (a) indicate the positions of the correlation streaks. The red box in (a) shows at which q-position the region of interest (ROI) was chosen in order to extract the GISAXS line profiles. To improve the statistics of the line profiles the ROI was integrated along the q_z-direction. The resulting horizontal GISAXS sections are shown for the respective coverages in (f). One observes that the maximum position of the correlation peaks shifts towards smaller $q_{||}$ for increased film thickness indicating the increase in the in-plane correlation length as a function of film thickness. Note that the curves have been shifted for clarity in (f).

wings, where multiple scattering and absorption effects are essentially negligible). As a consequence, the Born approximation [97] still holds and an appropriate theoretical model can be used in the data analysis. Albeit, there are pre-built tools for GISAXS data analysis, such as the software package "FitGISAXS" [164], which is based on the distorted wave Born approximation, we find that some of the more realistic island shapes, e.g. a cone, are currently not supported. Therefore, we restrict ourself to model the line profiles with the description provided in the next section.

5.2.2.2 Modeling the GISAXS profiles

In the following, we introduce a simple model similar to Refs. [86,165,166] to describe the scattering intensity I. In this approach, the scattering occurs from N identical "objects", i.e. islands, with a three–dimensional shape, which are distributed on a two–dimensional plane (parallel to the substrate) such that their distribution only depends on the in–plane coordinates. The average two–dimensional density of the islands is denoted by ρ. In general, we decompose the three–dimensional scattering vector $\mathbf{q}$ and the three–dimensional position vector $\mathbf{r}$ into in–plane ($||$) and z–components:

$$\mathbf{q} = \begin{pmatrix} \mathbf{q}_{||} \\ q_z \end{pmatrix}, \quad \mathbf{r} = \begin{pmatrix} \mathbf{r}_{||} \\ z \end{pmatrix} \tag{5.10}$$

Hence the scattering intensity can in general be expressed as a product of an island form factor and a factor describing the in–plane distribution of the islands [153,167,168]

$$I(\mathbf{q}_{||}, q_z) \propto |F(\mathbf{q}_{||}, q_z)|^2 \left\langle \sum_{j=1}^{N} \sum_{k=1}^{N} e^{i\mathbf{q}_{||}\cdot(\mathbf{r}_{j,||} - \mathbf{r}_{k,||})} \right\rangle , \tag{5.11}$$

where $\mathbf{r}_{j,||}$ is the in–plane position vector of island j and the form factor F is defined as the Fourier transform of the three–dimensional island shape function $\Omega_s(\mathbf{r}_{||}, z)$. Introducing the in–plane pair correlation function for the islands, $g(\mathbf{r}_{||})$, and the total correlation function $h(\mathbf{r}_{||}) = g(\mathbf{r}_{||}) - 1$, one can define a two–dimensional structure factor by $S(\mathbf{q}_{||}) = 1 + \rho\tilde{h}(\mathbf{q}_{||})$ where $\tilde{h}(\mathbf{q}_{||})) = \mathrm{FT}_{2D} h(\mathbf{r}_{||})$ is the two–dimensional Fourier transform of h. With these definitions, the scattering intensity becomes

$$I(\mathbf{q}_{||}, q_z) \propto N|F(\mathbf{q}_{||}, q_z)|^2 \left(S(\mathbf{q}_{||}) + (2\pi)^2 \rho \delta^{(2)}(\mathbf{q}_{||}) \right) . \tag{5.12}$$

Thus I contains a delta-peak corresponding to the in–plane forward direction. In the following, this peak will be neglected since it is not resolved by the measured diffuse scattering intensity $I \equiv I_{\mathrm{diff}}$ [85,99,168].

In order to obtain information about the island shape, the scattering intensity will be analyzed at a particular q_z but in real space on the plane. Hence one needs a two–dimensional inverse Fourier transform (FT_{2D}^{-1}) of Eq. (5.12). We introduce

$$\Phi(\mathbf{r}_{||}, q_z) = \mathrm{FT}_{2D}^{-1} |F(\mathbf{q}_{||}, q_z)|^2 \tag{5.13}$$

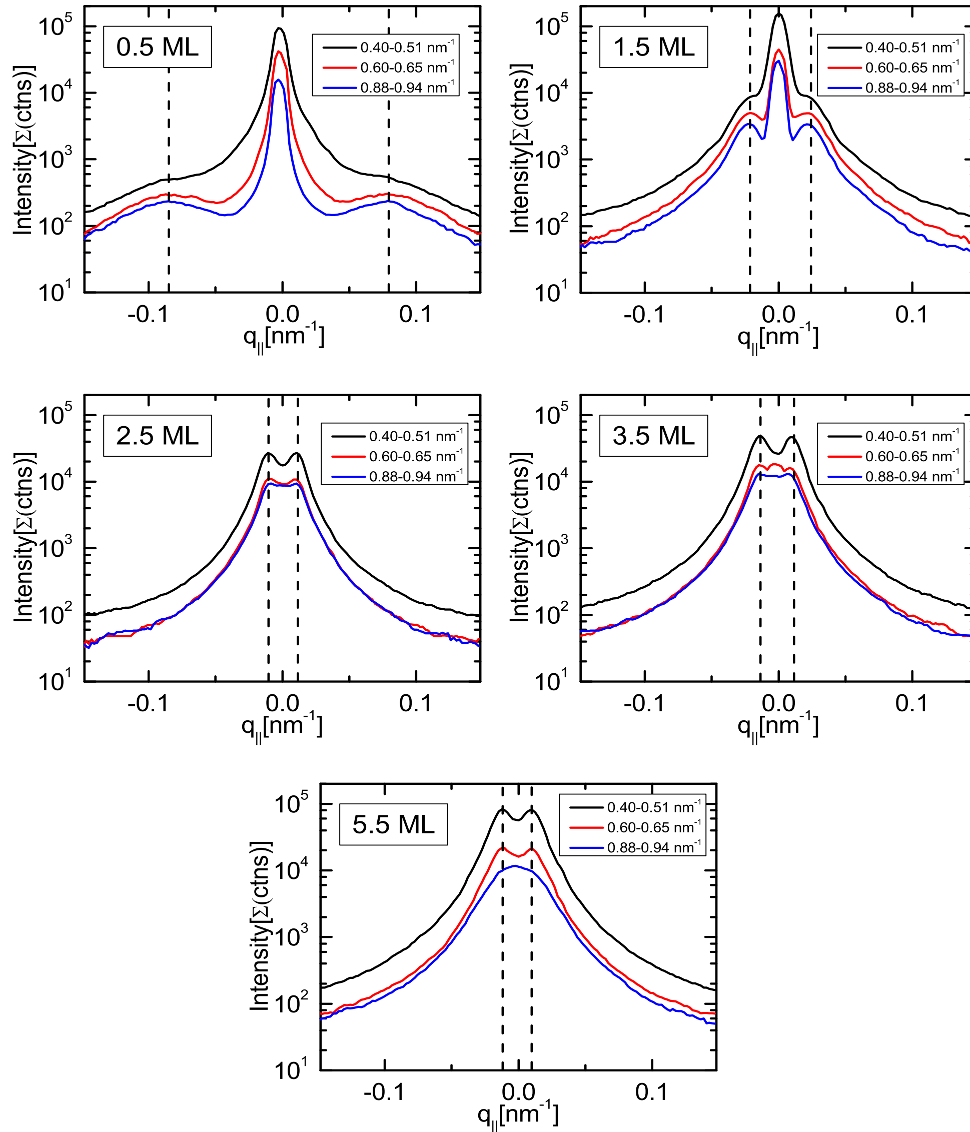

Figure 5.15: Horizontal sections of the GISAXS-signal taken from Fig. 5.14. Sections are extracted in the ranges $q_{z,1} = 0.4–0.51\,\mathrm{nm}^{-1}$, $q_{z,2} = 0.6–0.65\,\mathrm{nm}^{-1}$ and $q_{z,3} = 0.88–0.94\,\mathrm{nm}^{-1}$ and shown for thicknesses between 0.5–5.5 ML. Dashed lines indicate that the position of the correlation peak does not change with respect to q_z.

which is related to the (real–space) island shape function Ω_s by

$$\Phi = (\mathrm{FT}_z\Omega_s) \otimes (\mathrm{FT}_z\Omega_s)^\star \,. \tag{5.14}$$

Here, FT_z is the Fourier transform in z–direction, $\otimes$ denotes the two-dimensional, in–plane convolution and * denotes complex conjugation. Hence Eq. (5.12) becomes

$$\begin{aligned}\hat{I}(\mathbf{r}_{||}, q_z) &= \mathrm{FT}_{2D}^{-1} I(\mathbf{q}_{||}, q_z) \\ &\propto N\left(\Phi(\mathbf{r}_{||}, q_z) + \rho\Phi(\mathbf{r}_{||}, q_z) \otimes h(\mathbf{r}_{||})\right)\end{aligned} \tag{5.15}$$

For our subsequent analysis, we assume an island shape which is isotropic in the plane, hence $\hat{I}, \Phi, h$ depend only on $r_{||} = |\mathbf{r}_{||}|$. Determination of the island shape (using the shape function Ω_s and, derived from it, the function Φ) is easily possible if the total correlation function in the plane h is sufficiently small and the variations of h occur on larger length scale than those of Φ. Then one can restrict oneself to regions of small $r_{||}$ where $\hat{I}$ is dominated by the island form factor contribution and assume

$$\hat{I}(r_{||}, q_z) \propto N\,\Phi(r_{||}, q_z) \qquad (\text{small } r_{||})\,. \tag{5.16}$$

This equation will be used in the following to determine the average island shape. The different island shapes used to model our data are shown in Fig. 5.16.

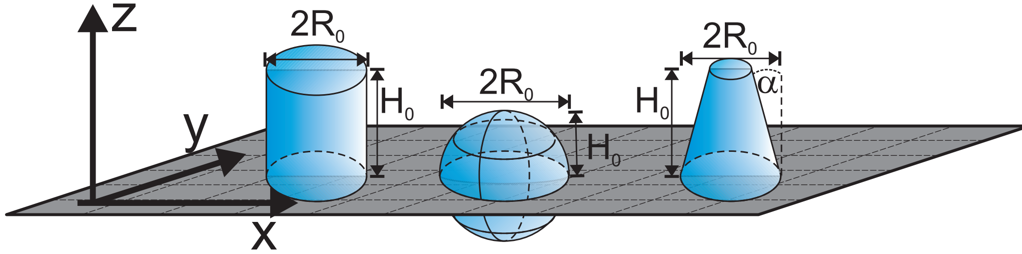

Figure 5.16: Geometries of the island shape used to fit Φ in Eq. (5.16). Shown from left to right are a cylinder, a truncated sphere and a cone. The most relevant fit parameters are the radii R_0 and the tilt angle α of the cone.

5.2.2.3 Discussion of the GISAXS profiles

A comprehensive summary of the inverse in–plane Fourier transform $\hat{I}(r_{||}, q_z = 0.91\,\mathrm{nm}^{-1})$ of the GISAXS line profiles is provided for all samples in Fig. 5.17. For all coverages 0.5...5.5 ML, $\hat{I}$ shows a strong variation for small $r_{||}$ ($r_{||} \lesssim 100$ nm) which are attributable to the island shape. However, for the lowest coverages of 0.5 and 1.5 ML, $\hat{I}$ is not small for larger lengths and shows a decay on the scale of several hundred nm. It is actually difficult to explain this behavior of $\hat{I}$ using Eq. (5.15) which is based on a model of monodisperse islands having a size of about 100 nm. Indeed, the AFM images for these low coverages (see Fig. 5.18a and Fig. 5.18b) reveal that islands are quite dense and are coalesced to

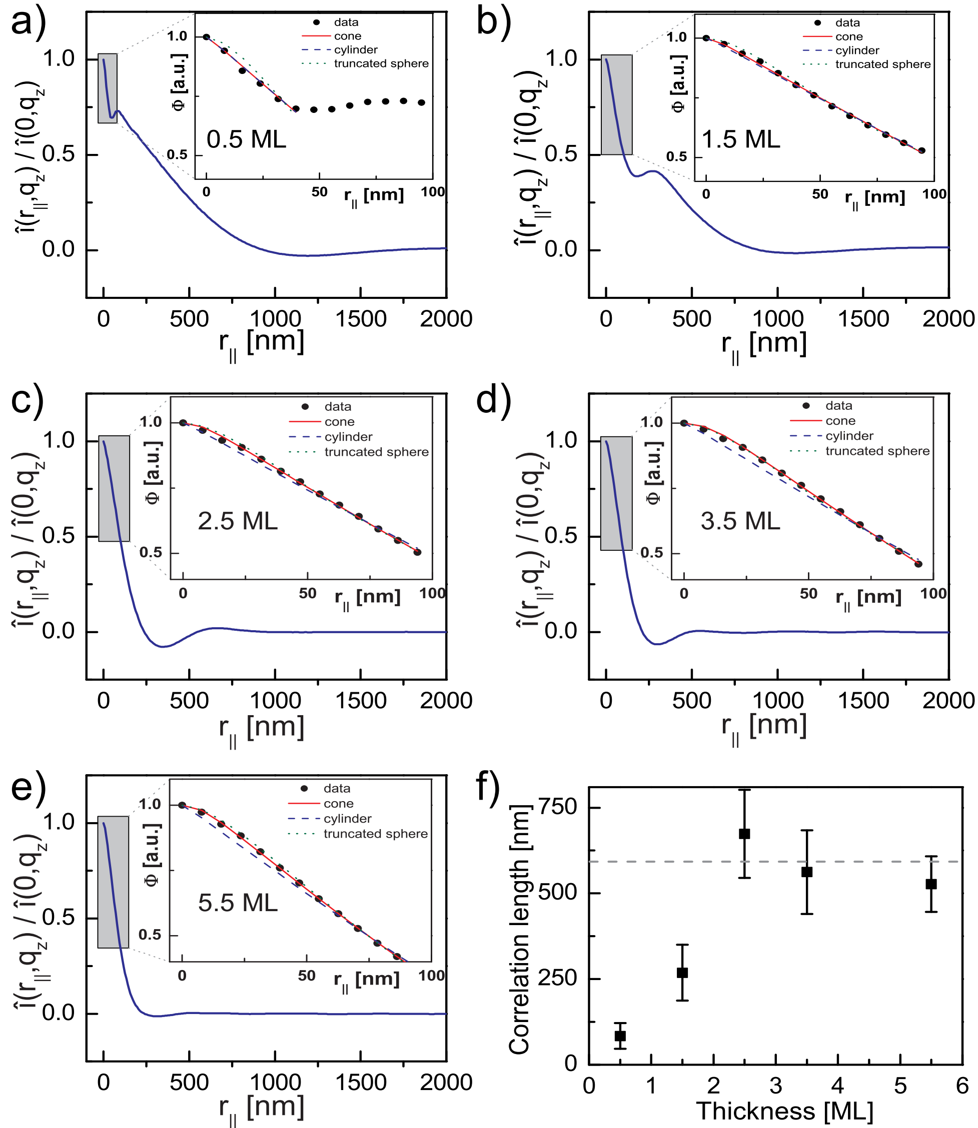

Figure 5.17: (a-e) Normalized Fourier transform (blue solid line) of the line profiles shown in Fig. 5.14 for coverages Θ of 0.5 to 5.5 ML (taken at $q_z = 0.91\,\mathrm{nm}^{-1}$). The inset shows a magnification for small radii (indicated by the shaded area) along with the fit of Φ for the different island shapes. (f) In-plane correlation length observed in the morphology of the samples, as function of film thicknesses. The correlation lengths are obtained from (a-e) and can be related to the average inter-island distance. The dashed line represents the saturation value.

greater, anisotropic objects with different sizes. This case should be more appropriately analyzed with a model taking into account the polydispersity of such fused islands, and we expect that fitting an island shape through Eq. (5.16) is a first guess. For higher coverages (2.5 to 5.5 ML) the separation of form factor and pair correlation contribution

is much clearer in the results for $\hat{I}$. From the behavior at $r_{||} > 200$ nm, one can infer that the total correlation function h shows small oscillations with a relative strength of about 10% of the maximum value of $\hat{I}$ with a first minimum at about 250 nm. This is consistent with pair correlations of hard objects of about 100 nm size at small to moderate densities. The positions of the first maxima of $\hat{I}$ in Fig. 5.17a – Fig. 5.17e account for an in-plane correlation length within the sample surface and can be related to the average (nearest neighbor) island-to-island distance.

The dependence of the inter-island distance (or inter-island spacing) on the film coverage, as derived from the positions of the first maxima, is demonstrated in Fig. 5.17f. We observe that the inter-island spacing for small coverages (0.5 and 1.5 ML) is substantially smaller than the inter-island spacing for higher coverages. In view of the discussion above, the small distance for 0.5 ML ($\approx$ 80 nm) is just the distance of coalesced islands, while for 1.5 ML ($\approx$ 250 nm) it is related to both coalescence and distance between islands since the islands are quite dense. In the case of 3D-growth (for small film thicknesses) the inter-island distance does not depend on the amount of deposited material, since mounds only grow higher but do not change their lateral positions. Therefore, the saturation value of $\simeq 600$ nm, which is achieved for thicknesses $\Theta \geq 2.5$ ML, points to the formation of 3D-islands. These observations are consistent with the *in situ* evolution of the inter-island distance reported in Ref. [31].

5.2.2.4 Fitting the GISAXS profiles

Based on the theory discussed in the previous section, the mean island shape and size can be determined from the functional dependence of $\hat{I}(r_{||}, q_z) = \mathrm{FT}_{2D}^{-1} I(q_{||}, q_z)$ close to $r_{||} = 0$. Since $\Delta r_{||}$, i.e. the minimum resolvable distance between two points in real space, is given by $\pi/q_{||,\mathrm{max}}$, a sufficient experimental resolution and maximum momentum transfer are required to satisfy the Nyquist-Shannon sampling theorem [169] and to obtain information close to $r_{||} \simeq 0$.

In our model, $\hat{I}$ close to $r_{||} = 0$ is only determined by the island shape function (see Eqs. (5.14) and (5.16)). When using hard shapes with rotational symmetry as depicted in Fig. 5.16, the necessary in–plane convolutions in $\hat{I}$ could also be computed analytically (overlapping circles), and an additional z–integration has to be done numerically. Here, we have chosen to fully numerically compute $\hat{I}$ by using Fast Fourier transformation techniques in Eq. (5.13). Owing to the cylindrical symmetry of the islands, the 2D Fourier transform for the $||$-component can actually be related to a Hankel transform, when using polar coordinates. The Hankel transform is most efficiently calculated by the logFFT algorithm [170, 171], i.e. by solving the Fast Fourier Transform (FFT) on a logarithmic grid. Note that from a numerical perspective, the Hankel transform is ideally suited to analyze the full range of $\hat{I}$, i.e. taking the correlations of the islands $h(r)$ into account, or to analyze "fuzzy" shape functions which would arise when one orientationally averages over fused islands. This is however beyond this study but potentially interesting for future work. Accordingly, utilizing the scientific computational software package "MATLAB" [172], Φ has been calculated using the form factor of either a cylinder, a cone or a truncated

Thickness [ML]	Cylinder Model [χ^2]	Tr. Sphere Model [χ^2]	Cone Model [χ^2]
0.5	287.9	2393.8	384.0
1.5	120.5	159.3	83.6
2.5	368.3	143.8	62.2
3.5	902.2	116.5	45.4
5.5	781.3	148.5	25.9

Table 5.1: χ^2-parameters obtained by fitting the data in Fig. 5.17 with different island shapes. Note that we assumed constant weighting factors for all data points in $\Phi(r_{||}, q_z)$.

sphere. A summary of the prevailing theoretical descriptions and a collection of form factors for the different island shapes can, for instance be found in Ref. [97]. To fit the data, the autocorrelation functions for the respective island types were implemented in the MATLAB software package "Mfit" [173]. The optimization of the parameters was then performed using the Simplex Nelder-Mead algorithm [174], which is ideally suited to minimize higher dimensional problems. The resulting deviation from the dataset yields the χ^2-parameter for the goodness of the fit. Based on the AFM-images shown in Fig. 5.18 we have determined the height H_0 of the islands for each thickness and subsequently used this as an initial guess for the fitting. As expected, it turned out that Φ is not very sensitive to the island height. Thus, depending on the island type, the base radius R_0 and, in the case of the cone also the tilt angle α, are the relevant parameters to describe Φ. A description of the parameters and the island shapes used for the fitting is shown in Fig. 5.16 and a complete summary of the χ^2-parameter for all the fits is given in Tab. 5.1.

Analysis of the morphology and comparison with AFM

In order to compare the different island shapes AFM measurements for all *ex situ* samples are shown in Fig. 5.18. A close inspection of the images taken for $\Theta = 0.5\,\text{ML}$ and $\Theta = 2.5\,\text{ML}$ reveals that islands already coalesce, which suggests that here the top layer coverages are slightly larger than 50%. The insets of Fig. 5.18 show the island size distribution for the top structures along with a Gaussian fit to obtain the mean island size. From the full width at half maximum (FWHM) of the Gaussian fits one finds the polydispersity of islands, which is largest for $\Theta = 1.5\,\text{ML}$. Remarkably, we observe that the radii obtained by the GISAXS fits (see Fig. 5.18f) match very well with the AFM radii of the structures on top of the islands. This becomes most evident for $\Theta = 2.5\,\text{ML}$ (see Fig. 5.18c) where the bottom terraces are of the order of $\sim 500\,\text{nm}$, whereas the top structures are of the order of $\sim 100\,\text{nm}$. We suppose that the contrast in the electron density is much higher in the very top layers as compared to the bottom layers. These are practically filled (especially at $\Theta = 2.5\,\text{ML}$) and act like the "substrate" for the mounds. Thus, the main contribution to the scattering signal comes from the top layers allowing

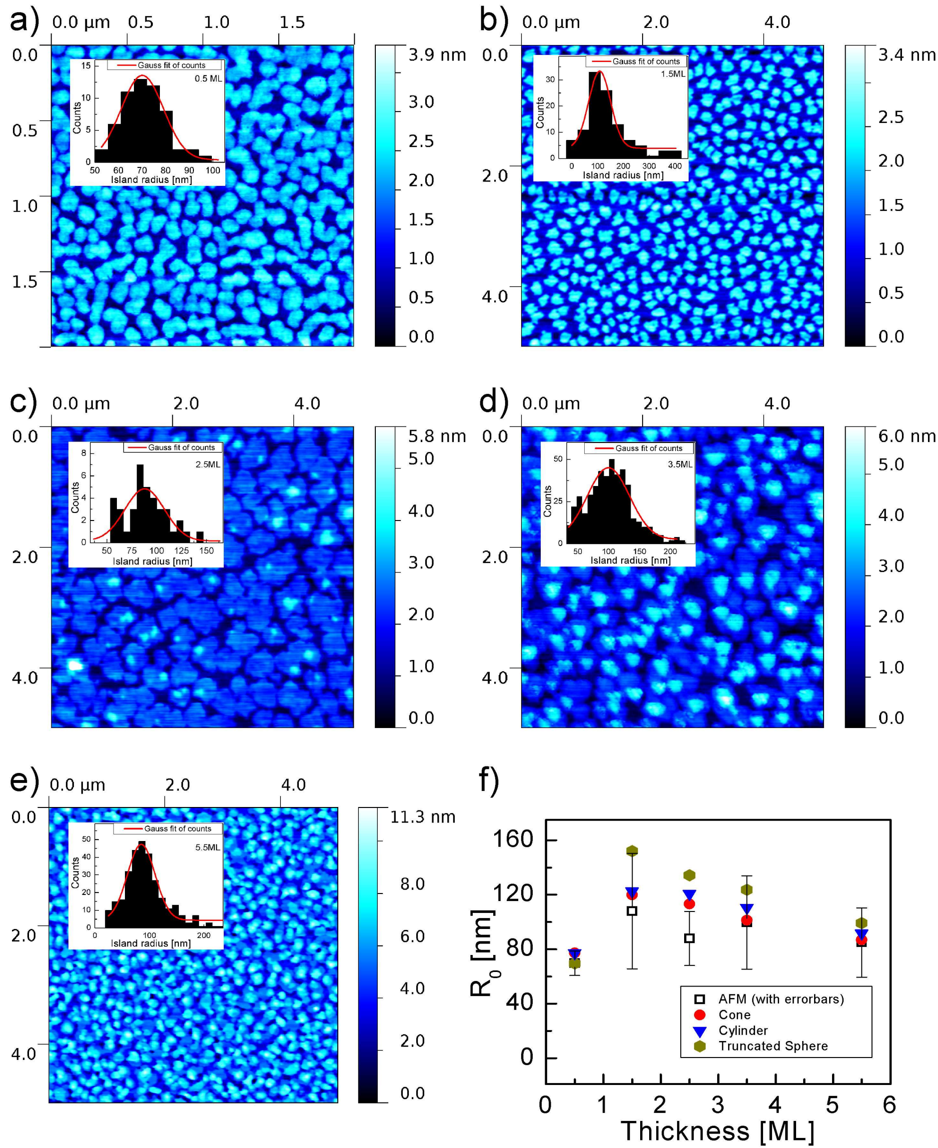

Figure 5.18: (a-e) AFM images for $\Theta = 0.5$–$5.5\,\mathrm{ML}$. The inset contains the respective island-size distribution along with a Gaussian fit. The images for 0.5 ML and 2.5 ML show a signature of the coalescing of islands, which suggest that the top layer filling is slightly larger than 50%. (f) Comparison of the thickness dependent radius obtained by AFM (black squares with error bars accounting for the polydispersity) and the GISAXS fits using different island shapes. Among the models used the cone model provides the best description for most of the thicknesses.

the GISAXS technique to primarily sense the top structures.

The insets of Fig. 5.17 provide a summary of the results obtained by fitting the fall-off of $\hat{I}(r_{||}, q_z)$ normalized to $\hat{I}\left(r_{||} = 0, q_z\right)$ with the function $\Phi(\mathbf{r}_{||}, q_z)$. From the fits in

Fig. 5.17 (summarized in Tab. 5.1) we observe that the modeling with the cone model provides an excellent agreement at higher film coverages. In contrast, we find that the goodness of the fit, i.e. χ^2, becomes worse towards small coverages. For the fits with the cylinder model it is the other way around, i.e. we obtain better agreement at low film coverages.

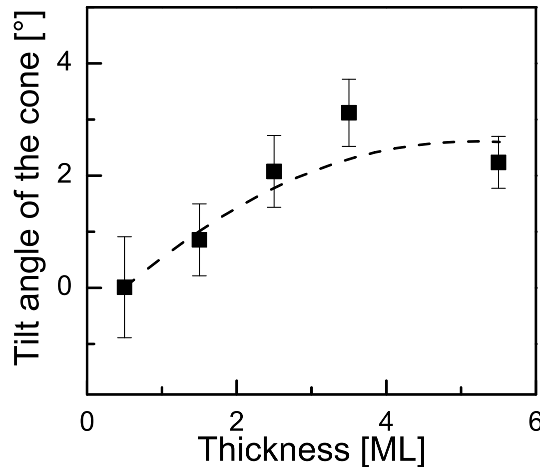

Figure 5.19: The tilt angle of the cones is shown as a function of the film thickness. Smaller film thicknesses favor a cylinderlike island shape, whereas larger ones deviate from that shape. Note that the dashed line should only serve as a guide for the eyes.

The preceding discussion allows to compare the mean island radii obtained by AFM with those obtained by GISAXS as shown in Fig. 5.18f. For the cylinder and the cone model we observe very good agreement for all coverages except for $\Theta = 2.5\,\mathrm{ML}$. However, as mentioned above, this sample particularly features a strong signature of island coalescence and thus a precise statistical determination of the island size is difficult with both methods. We note that the truncated sphere model overestimates the island radius significantly for coverages $\Theta > 0.5\,\mathrm{ML}$. For the sample, which shows the worst fit, i.e. $\Theta = 2.5\,\mathrm{ML}$, the cone model deviates by $\sim$22% from the AFM data, while the truncated sphere model already differs by $\sim$35%. Therefore, we conclude that the truncated sphere model is physically less relevant. Henceforth, the following discussion will only focus on the cylinder and cone shapes. From our observations these models provide a better parameterization of the film surface.

Thickness dependence of the island shape

To further exploit how the morphology varies, we show the tilt angle α (obtained from fitting our data with the cone model) versus the film coverage in Fig. 5.19. As intuitively expected, we find that for low thicknesses ($\Theta \leq 1.5\,\mathrm{ML}$) the tilt angle α is very close to $0\,^\circ$ corresponding to a cylinder (i.e. a cone with a tilt angle of $0\,^\circ$). Evidently, the tilt angle increases only slightly for higher coverages. However, we observe that such a slight

increase, already, has a large impact on the shape of the islands: obviously, a significant deviation from the cylinder shape is necessary to suit the moundlike surface morphology of the growing islands (see also Tab. 5.1).

This also complies with the results of Ref. [31] where we observe a layer-by-layer growth until a film coverage of 2 ML and subsequently a transition to a 3D growth. Therefore, we suppose a growth scenario of the following type: at low coverages (i.e. $\Theta \leq 2\,\mathrm{ML}$) a relatively large interlayer mass transport results in 2D (cylinderlike) islands, which increase in size as the growth progresses and finally merge into non-geometric anisotropic shapes, thus accounting for a layer-by-layer growth. At high coverages (i.e. $\Theta > 2\,\mathrm{ML}$) the interlayer transport is significantly smaller, which leads to the formation of mounds, therefore we observe a measurable deviation from the cylinder shape. An extreme case would be met, if the interlayer mass transport is completely suppressed resulting then in Poisson-growth. Both, this intermediate case of "wedding-cake" structures and the extreme Poisson-growth have previously been observed [36].

Further improvement of the fits may be obtained e.g. by modeling Φ with two partly merged cylinders in the very low coverage regime. Here, islands show a signature of coalescence and a precise evaluation is more difficult. However, implementing such a complex function is rather challenging and is beyond the scope of the present study.

5.2.3 Conclusion

This work presents GISAXS measurements of ultra-thin films (i.e. below 6 ML) of the organic semiconductor DIP grown on native SiO_x-substrates. Using the shape function of a cone, a cylinder and a truncated sphere we model the DIP-islands and determine the mean radius. This allows for a comparison with the island size distribution obtained by our supporting AFM measurements. Remarkably, we observe a significant difference between the employed models. We find that for low film coverages a cylinder provides a suitable shape function to model the islands. Towards higher thicknesses a continuous deviation from the cylinder shape is observed, which is characterized by the formation of wedding-cake structures in the film morphology.

This work in principle provides a comprehensive picture on the complicated nature of thin film growth and in general its dynamics, which are not yet fully deciphered. Importantly, we believe that the presented approach is not only useful to analyze the surface morphology of organic thin film growth in real time, but additionally, may successfully be adopted to other materials potentially featuring a very different shape.

The next step to acquire a better understanding of the growth, especially in the sub-monolayer coverage regime demands for the utilization of real-time techniques. Based on the findings in the preceding sections, the next part investigates in real-time how the GISAXS-pattern of DIP changes during the film growth. Importantly, measurements were here performed on a sufficiently small time-scale, which allows to observe dynamic processes.

5.3 Real-time GISAXS measurements on pristine DIP

The content of the following section has been published in Ref. [31][4].

Substantial experimental as well as theoretical efforts have been made to establish a molecular level understanding of the physics underlying the growth of organic thin films [8, 34,139,175,176]. Yet, connecting microscopic and macroscopic processes such as molecular diffusion and island size evolution remains a serious challenge. This is particularly true for rod-shaped organic semiconductor molecules because of their additional degrees of freedom, i.e. tilting (for non-spherical compounds) and bending (for flexible compounds). In this context, diindenoperylene (DIP, $C_{32}H_{16}$) is known to exhibit the complexities of the growth process rather typical for molecular systems with shape anisotropy [25,68,157,158]. These can include, e.g., rapid roughening, thickness-dependent lattice parameters and the competition of different structural phases. Since some of these effects may be transient, a key to their understanding are real-time investigations [125, 177, 178]. An important aspect is the evolution of the lateral island size l (see Ref. [179]), which not only can be used to optimize the thin film growth, but also provides information on the surface diffusion.

In this section, we investigate the growth of DIP with film thicknesses of only a few monolayers (ML) on native silicon oxide at different deposition rates and substrate temperatures. Simultaneous recording of the specular [64,88] and the off-specular (diffuse) [180] intensities (see Fig. 5.20), which is performed *in situ* and in real-time in this study, allows to gain insight into the growth mechanisms and evolution of islands of such anisotropic organic molecules. Notably, the specular signal was measured at a fixed incidence angle, which was chosen to coincide with the so called anti-Bragg point [88, 181], i.e. at half of the reciprocal lattice vector belonging to the (001) reflection of the DIP σ-phase [158]. Among the prevalent off-specular scattering techniques, grazing incidence small angle x-ray scattering (GISAXS) [98, 100] is the ideal tool to characterize the growth process *in situ* in a non-invasive way. While the intensity at the anti-Bragg point contains time-resolved information on the out-of-plane film structure [129], the off-specular scattering in the vicinity of the critical angle α_c (Yoneda-wings) [86, 144] can be exploited to observe changes of the in-plane film morphology. This can be realized by the use of high brilliance synchrotron radiation in combination with a fast area detector with high dynamic range.

In particular, the oscillations of the specular intensity (which were extracted from the GISAXS images taken during film growth by choosing an appropriate region around the specular reflection at the anti-Bragg point) are analyzed taking into account a thickness-dependent out-of-plane lattice parameter in order to determine the different layer coverages. The evolution of the diffuse signal (extracted by choosing a suitable region in the vicinity of the Yoneda-wings) is then used to follow the film thickness dependence

[4] C. Frank, J. Novák, R. Banerjee, A. Gerlach, F. Schreiber, A. Vorobiev, and S. Kowarik, Phys. Rev. B **90**, 045410 (2014): *Island size evolution and molecular diffusion during growth of organic thin films followed by time-resolved specular and off-specular scattering.*

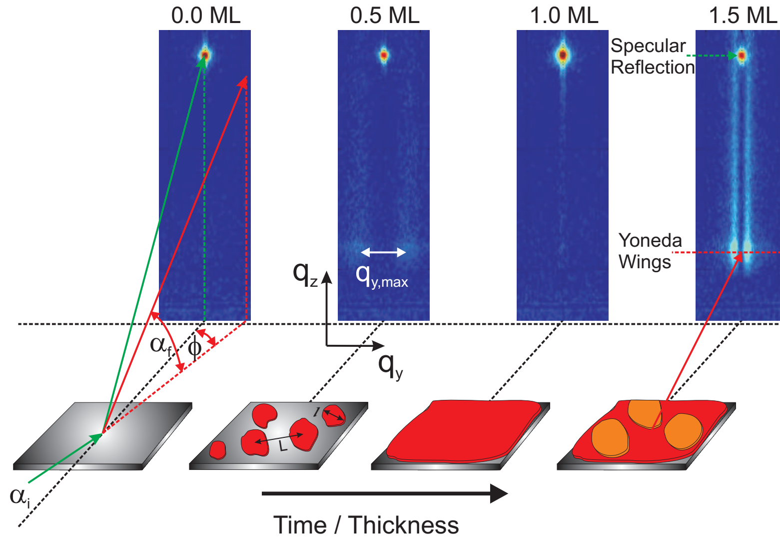

Figure 5.20: Scattering geometry, typically used in GISAXS experiments. Recording data with sub-monolayer time resolution allows to follow the growth in real-time. A gradual filling of successive layers leads to an oscillating intensity of the vertical streaks in the image series. The separation $q_{y,\,\mathrm{max}}$ of these features around the Yoneda-wings can be related to the average island-to-island distance L and for a known molecular coverage in the layer also to the average island diameter l.

of the average island size. Henceforth, any reference to "specular" and "diffuse growth oscillations" would correspond to the differently oscillating intensities taken from the respective part of the GISAXS profiles, as mentioned above. GISAXS measurements are complemented by *ex situ* x-ray reflectivity (XRR) and atomic force microscopy (AFM). Using the results of these investigations, we demonstrate the influence of the activation energy barrier on the island nucleation during the initial stages of growth.

5.3.1 Growth conditions and sample preparation

DIP was purchased from the Institut für PAH Forschung (Greifenberg, Germany) with gradient sublimation purity. The films were grown on SiO_x substrates in a portable UHV chamber [81], allowing control of the substrate temperature T_{sub} (25, 50 and 100 °C) and the growth rate R_{growth} (0.1, 0.4, and 1.1 nm/min). All real-time measurements were performed at beamline ID10B of the ESRF (Grenoble, France) at a wavelength of $\lambda = 0.929\,\text{Å}$ and an incidence angle of $\alpha_i = 0.8\,°$, which corresponds to the anti-Bragg condition of the (standing up) σ-phase of DIP [65,158,182]. For data acquisition a photon-counting pixel detector (MAXIPIX) was used, which provided a horizontal resolution of $\Delta q_{xy} = 2.8 \times 10^{-3}$ Å and a dynamic range of 2×10^5 counts/pixel.

In order to measure the in-plane and the out-of-plane structural evolution simultaneously, the GISAXS scattering geometry (as shown in Fig. 5.20) was employed. Corresponding to a wavelength of $\lambda = 0.929\,\text{Å}$, the critical angle ($\alpha_c$) of DIP was $0.12\,°$. Both,

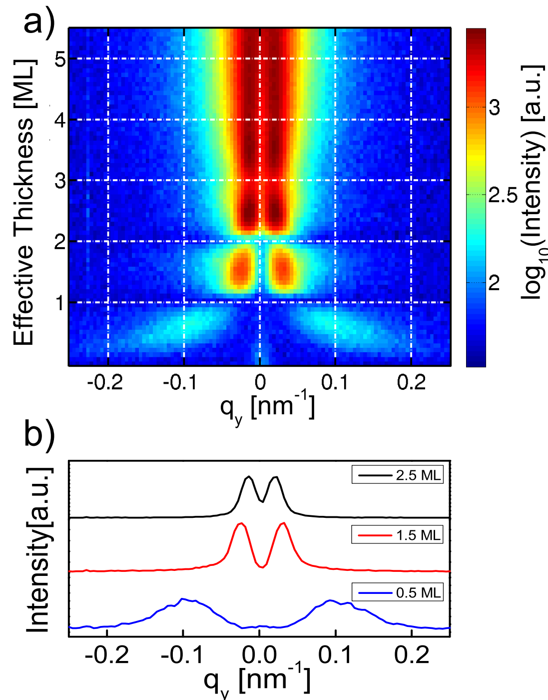

Figure 5.21: (a) Scattering intensity at the critical angle (Yoneda-wings) as a function of adsorbed material for DIP grown at $T_{\text{sub}} = 25\ ^\circ\text{C}$ and $R_{\text{growth}} = 0.1\,\text{nm/min}$. Detector images from which the horizontal GISAXS sections have been extracted, were integrated for 20 seconds per frame leading to a resolution of $\simeq 15$ frames/ML. (b) Horizontal line sections (extracted from the GISAXS images in (a)) at coverages of $\theta = 0.5$, 1.5, and 2.5 ML. It is clearly observed that the separation between the two correlation peaks decreases for higher film coverages. As the growth progresses, more material is adsorbed on the surface and the correlation peaks become more intense.

the specular (i.e. $\alpha_i = \alpha_f = 0.8\,^\circ$, $\phi = 0\,^\circ$) and the GISAXS (i.e. $\alpha_f \approx \alpha_c$, $\phi \neq 0\,^\circ$) signal are analyzed as a function of time. This allows a self-consistent thickness calibration in units of monolayer equivalents.

5.3.2 Results and discussion

Figure 5.21 shows the evolution of the GISAXS intensity profiles integrated within the region $q_z = 1.03$–$1.30\,\text{nm}^{-1}$ as a function of adsorbed material and the in-plane momentum transfer q_y. The chosen range includes the Yoneda-wings, thus providing information on the characteristic surface correlation length. The associated time-resolution was $\simeq$ 15 frames/ML, where each frame has been exposed for 20 seconds. The appearance of two relatively weak correlation peaks at the very beginning of the growth ($q_y \simeq 0.17\,\text{nm}^{-1}$) indicates the existence of a well-defined correlation length, which corresponds to the average island-to-island distance L. Below one ML coverage, we observe a significant

change in the intensity as well as in the position of these correlation peaks. The shift towards smaller values of q_y ($\simeq 0.05\,\mathrm{nm}^{-1}$) implies that the island-to-island distance, measured from the island's center of mass (see Fig. 5.20), increases as the 1$^{\mathrm{st}}$ layer is being filled. At a coverage of 1 ML both peaks disappear, which points to the absence of any noticeable long-range surface modulations for the smooth, completely filled 1$^{\mathrm{st}}$ ML. The off-specular intensity oscillates between a maximum at half-filled layers to a minimum at the completion of subsequent layers. During the growth of the 2$^{\mathrm{nd}}$ ML the peaks appear at still smaller values of q_y ($\simeq 0.03\,\mathrm{nm}^{-1}$). Above ~ 3 ML we observe two intense streaks, which do not change position with respect to q_y, accounting for an average correlation length-scale which is representative of the finite average distance of the DIP mounds. This is a clear signature of a transition from the layer-by-layer (LBL) to the 3D-growth, i.e. formation of molecular islands, which is analogous to the classical Stranski-Krastanov (SK) growth mode. Similar observations were made for other growth conditions of the film (e.g. different temperature and growth rate), indicating that in general for DIP the 1$^{\mathrm{st}}$ ML is always completely filled before the 2$^{\mathrm{nd}}$ or subsequent ML grow on top of it. Generally, the critical thickness, at which a transition from the LBL to the 3D-growth occurs, depends non-trivially on R_{growth} and T_{sub} and requires separate systematic investigations to gain further detailed knowledge.

5.3.2.1 Analysis of the out-of-plane structure

To probe the dependence of the out-of-plane structure on the growth conditions, we have analyzed the thickness-dependent intensity at the anti-Bragg point (corresponding to $q_z = 1.87\,\mathrm{nm}^{-1}$) using a combination of a growth model first proposed by Trofimov *et al.* [183] and kinematical scattering theory [25, 88, 129] (see Fig. 5.22a – Fig. 5.22c).

According to this prevailing model (PM) the total scattering intensity is given by

$$I(t) = \left| A_{\mathrm{sub}}(q_z) e^{i\phi} + c \sum_n \theta_n(t) e^{-inq_z d} \right|^2 , \tag{5.17}$$

where A_{sub} is the scattering amplitude, ϕ the phase shift, c the molecular layer form factor, θ_n the coverage of layer n, q_z the out-of-plane momentum transfer, and d the out-of-plane lattice parameter. We find that this model deviates considerably from the observed intensities during the growth of the 2$^{\mathrm{nd}}$ ML for all DIP samples grown at high substrate temperatures (see Fig. 5.22). Organic molecules with shape anisotropy may exhibit a change of their tilt angle [175] — an effect which is not considered in Eq. (5.17). In particular for the molecular system DIP/SiO_x previous studies reveal kinetically determined orientational and structural transitions of the molecular layer, which (depending on the substrate material) take place in the first few-monolayer regime [158] and can be related to a thickness dependent inter-layer mass transport [157, 184]. This collective change of the molecular tilt angle potentially involves all layers simultaneously. Therefore, we introduce thickness-dependent parameters (c', Φ, d'), where Φ is the phase of the now complex layer form factor $c'e^{i\Phi}$. To determine at which stage and how gradually the collective

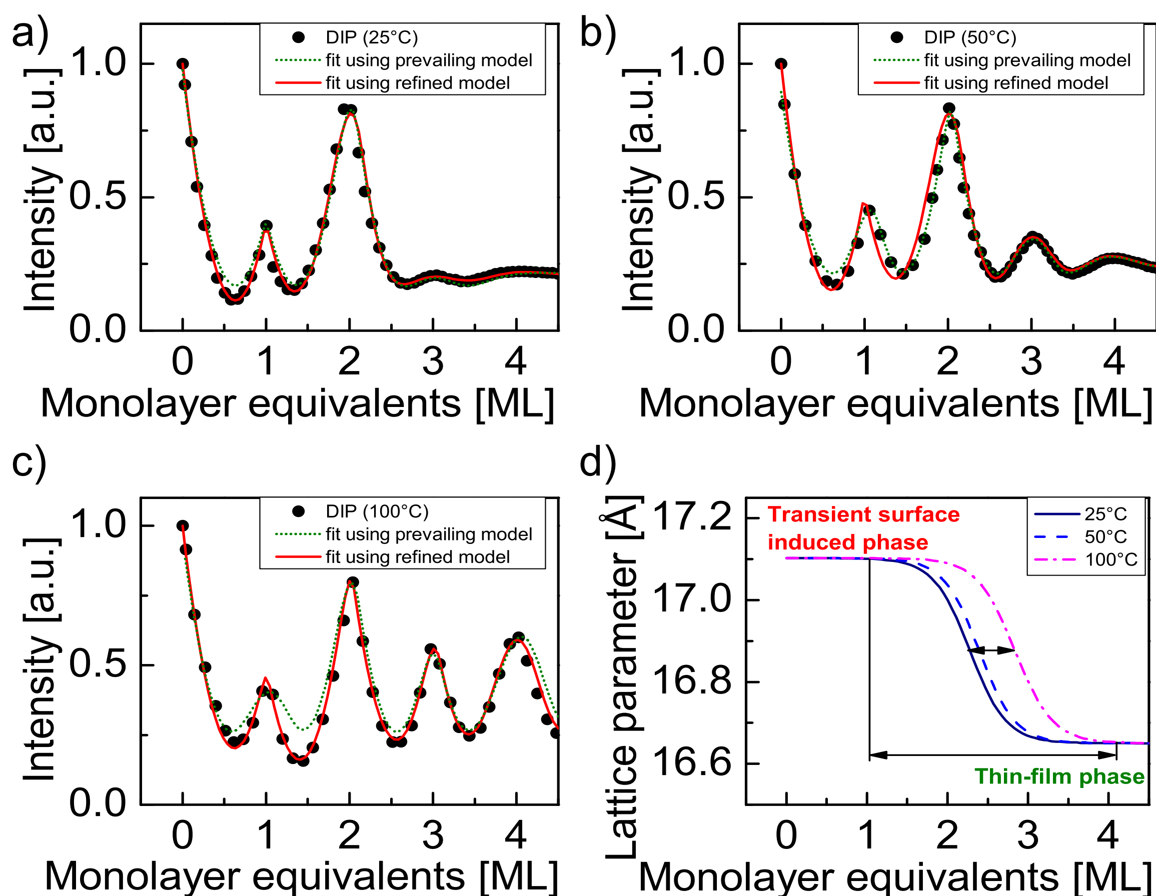

Figure 5.22: ((a-c) Specular oscillations at the anti-Bragg point (scatter plots) for DIP grown at $T_{\mathrm{sub}} = 25\ ^\circ\mathrm{C}$, $50\ ^\circ\mathrm{C}$, $100\ ^\circ\mathrm{C}$ and $R_{\mathrm{growth}} = 0.4\,\mathrm{nm/min}$. The data were fitted using the prevailing model (PM) but show a considerable deviation during the filling of the 2nd ML. However, the fit improved remarkably once the refined model (RM) has been applied. (d) Using the refined model the thickness dependence of the out-of-plane lattice parameter was determined for three different temperatures, showing an orientational transition from the transient surface induced to the thin-film phase. Importantly, the transition is delayed for higher substrate temperatures.

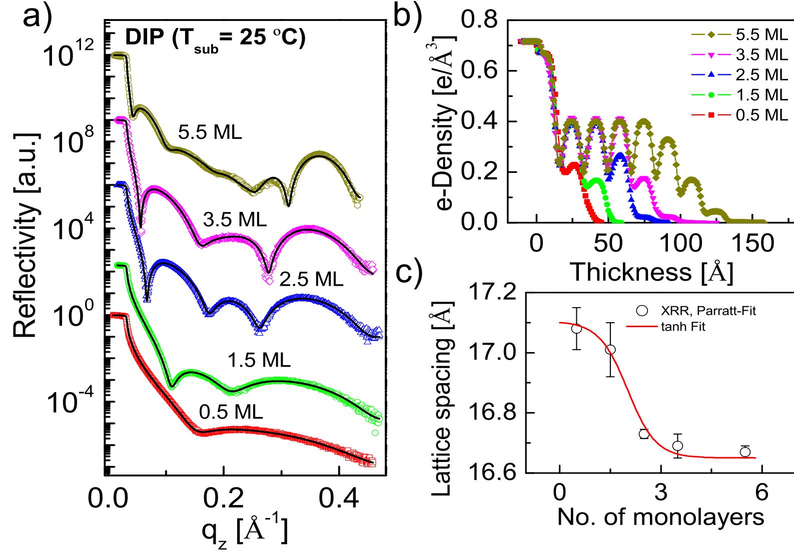

Figure 5.23: (a) *Ex situ* post-growth XRR scans (open symbols) of DIP grown at a substrate temperature of $T_{\text{sub}} = 25$ °C and a growth rate of $R_{\text{growth}} = 0.1\,\text{nm/min}$. The film thickness was varied between 0.5–5.5 ML. Solid lines show fits based on the Parratt formalism. (b) Corresponding electron densities plotted against the nominal film thickness. (c) Out-of-plane lattice parameters obtained from the XRR data shown in panel a (open circles) and the respective tanh-functional fit (solid line).

change occurs, the variation of the lattice parameter (as a function of thickness) is obtained from analyzing the XRR profiles of the films (see Fig. 5.23). The XRR data were fitted using the Parratt formalism [84,97]. The electron density profiles and the respective out-of-plane lattice parameters obtained from the fits are shown in Fig. 5.23b and 5.23c, respectively. Finding that the change in the lattice parameter can be well described using a tanh-functional dependence (Fig. 5.23c), we introduce an empiric variation of the three parameters c', Φ and d', (which, for the sake of convenience, are combined in a vector $\boldsymbol{P}$), according to

$$\boldsymbol{P}_{\gamma,t_0} = \boldsymbol{P}_\infty + \frac{\Delta \boldsymbol{P}}{2}\left(\tanh[\gamma(t-t_0)] - 1\right) \ . \tag{5.18}$$

From our data we are able to extract the asymptotic value $\boldsymbol{P}_\infty \equiv \boldsymbol{P}(t \to \infty)$, the variation $\boldsymbol{\Delta P} \equiv \boldsymbol{P}(t = t_0) - \boldsymbol{P}(t \to \infty)$ and the steepness parameter γ. Fitting the anti-Bragg growth oscillations with this function results in a remarkable agreement (see Fig. 5.22a – Fig. 5.22c).

Importantly, the change of the out-of-plane lattice depends on the growth temperature. For example, we observe that while the fit for 100 °C reproduces the experimental data very well, using the same functional dependence of the lattice parameter and complex layer form factor for a different temperature (say 25 °C) leads to a markedly different intensity profile. Figure 5.22d shows the thickness-dependent evolution of the out-of-plane lattice

parameter of the thin films at the same R_{growth} (0.4 nm/min) for three different T_{sub}. We find that the transition from the transient to the stable thin film phase, which results in a lattice spacing decrease of ~ 0.5 Å, occurs between 2–4 ML (see Fig. 5.22d). Interestingly, this change in the molecular tilt angle occurs simultaneously with the transition from the LBL to the 3D-growth. Additionally, we observe a delay in this collective molecular tilting (to the stable thin film orientation) for the films grown at a higher substrate temperature. We attribute this delay to the fact that the strength of the long-range in-plane cohesive interaction depends on the dimensions of the islands. Within the model-description it is quite reasonable to assume that the close packing of molecules within an island confines their respective molecular movements (including tilting). In particular, the more molecules are involved (i.e. the larger the island size), the more difficult it is to collectively cause the molecules to flip within that island. Consequently, we expect that the critical point, where the collective tilting occurs depends on the parameters describing the shape of the islands, i.e. for disc shaped islands (as observed in this study) the island-diameter and height. Because increasing T_{sub} leads to larger islands (as discussed later), the tilt is delayed.

5.3.2.2 Analysis of the in-plane morphology

AFM was performed post growth to complement our scattering measurements on the same set of samples with various thicknesses (0.5–5.5 ML) and coverages (see Fig. 5.24).

At ~ 0.5 ML 2D compact islands, which already start to coalesce, form on the substrate. At ~ 1.5 ML the substrate is completely covered by the 1$^{\text{st}}$ layer (Fig. 5.24b inset), which serves as a template for the nucleation of the 2$^{\text{nd}}$ layer. We also observe that islands nucleating on top of the 1$^{\text{st}}$ layer are significantly larger than those on SiO_x. For higher coverages (Fig. 5.24c and Fig. 5.24d) we observe mound formation with the 2$^{\text{nd}}$ layer providing the base for the mounds. This indicates a very pronounced LBL growth during the early stages, followed by a transition to island-like growth as was also observed in the GISAXS data (Fig. 5.21a).

For the quantitative analysis of the real-time GISAXS, we deduce the mean island-to-island distance $L = 2\pi/|q_{y,\,\text{max}}|$ from the position of the two correlation peaks using Lorentzian fits of the Yoneda-wing at an exit angle $\alpha_f \simeq \alpha_c$ (Fig. 5.25a). As expected for the initial LBL growth, the specular intensity oscillates up to ~ 3 ML. The subsequent 3D-growth results in a rapid damping of the oscillations. Importantly, the diffuse scattering intensity also exhibits pronounced oscillations in the LBL regime with maxima at half-filled and minima for closed layers. This anti-correlation of specular and diffuse intensities is related to the periodically changing surface roughness, i.e. for half-filled layers the roughness takes on a maximum. A sudden change of the island distance after filling the 1$^{\text{st}}$ layer accounts for the nucleation of new widely spaced islands in the 2$^{\text{nd}}$ ML. Additionally, we find that islands nucleating on top of the 1$^{\text{st}}$ layer are significantly larger than on top of the substrate, as also confirmed by AFM.

To derive the average island diameter l we approximate DIP islands as 2D disks and combine the layer coverage θ_n (obtained by fitting the anti-Bragg oscillations) with the

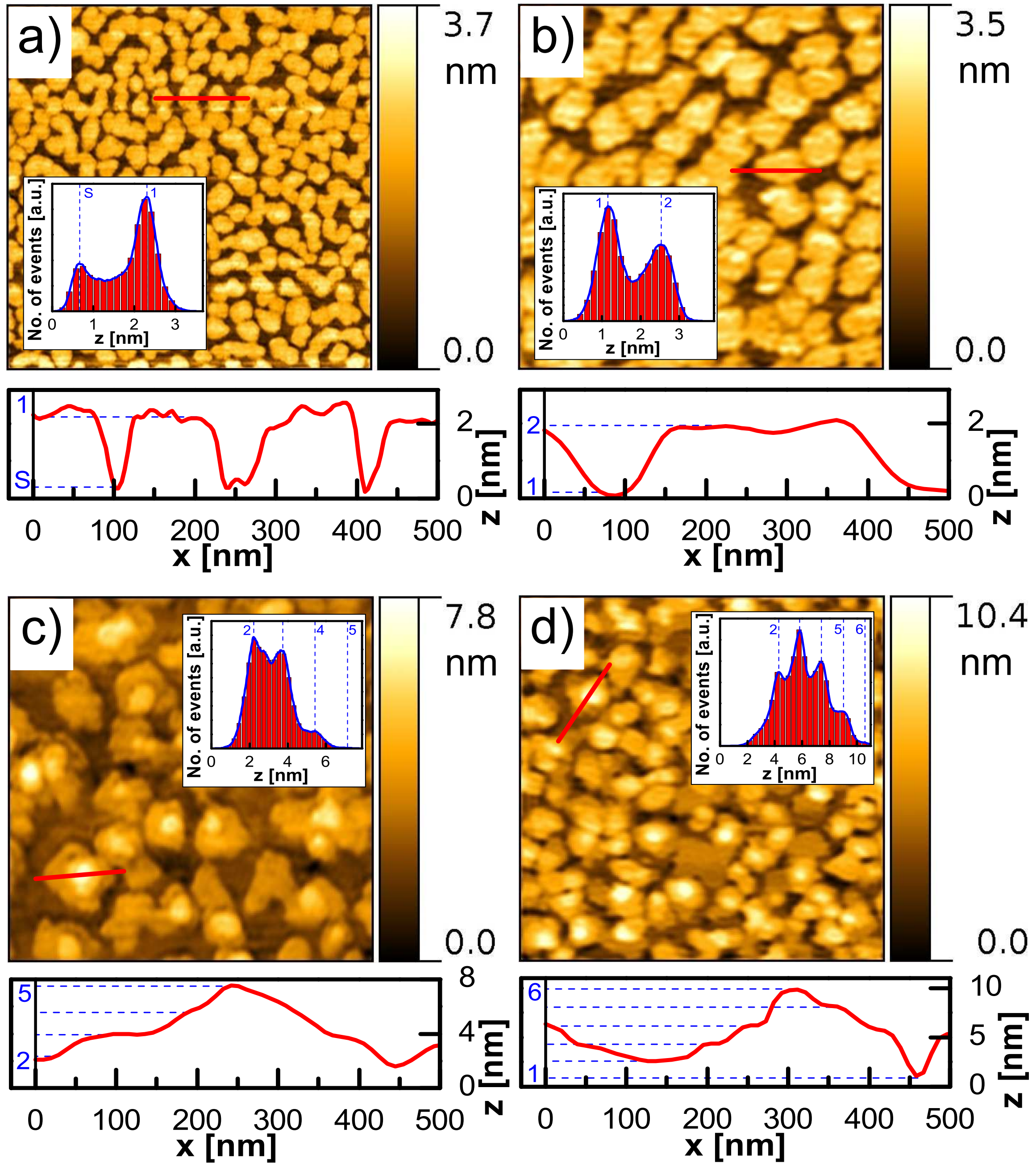

Figure 5.24: AFM images of DIP grown at $T_{\text{sub}} = 25$ °C and $R_{\text{growth}} = 0.1\,\text{nm/min}$ taken with a JPK Nanowizard II. Respective height-distributions are shown in the insets. Line profiles (indicated by red lines) are shown below the respective images. The images are shown for coverages of $\sim 0.5\,\text{ML}$, $\sim 1.5\,\text{ML}$, $\sim 3.5\,\text{ML}$ and $\sim 5.5\,\text{ML}$ (a–d) and cover an area of $2 \times 2\,\mu\text{m}^2$.

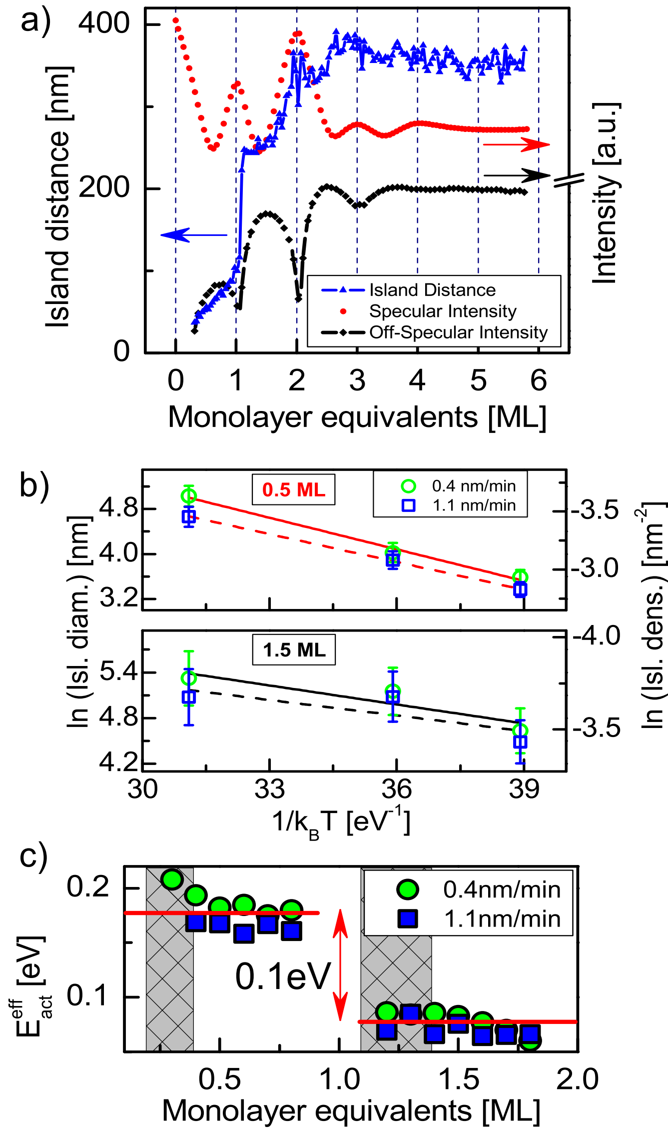

Figure 5.25: (a) Average island distance (left axis), specular and diffuse intensity (right axis) obtained by fitting the GISAXS data for DIP grown at $T_{\mathrm{sub}} = 25$ °C. (b) Arrhenius plot for two different growth rates and two different thicknesses. The solid lines correspond to linear fits of $R_{\mathrm{growth}} = 0.4\,\mathrm{nm/min}$ and the dashed lines to $R_{\mathrm{growth}} = 1.1\,\mathrm{nm/min}$, respectively. (c) Effective activation energy of nucleation $E_{\mathrm{act}}^{\mathrm{eff}}$ calculated for different coverages, which are almost constant throughout the layer filling. Note that $E_{\mathrm{act}}^{\mathrm{eff}}$ was derived using Eq. (5.19), which is valid only for small coverages (shown here as shaded areas).

island distance L given by $l = 2L\sqrt{\theta_n/\pi}$. Figure 5.25b shows that the island diameter extracted at coverages of 0.5 ML and 1.5 ML consistently follows the same trend within the investigated temperature/growth rate regime. For example, at $R_{\text{growth}} = 0.4\,\text{nm/min}$ and a coverage of 0.5 ML (1.5 ML) we find that the island size increases from $l = 36\,\text{nm}$ (103 nm) to $l = 153\,\text{nm}$ (205 nm), when increasing the substrate temperature from 25 °C to 100 °C. Increasing the growth rate to $R_{\text{growth}} = 1.1\,\text{nm/min}$ has less impact on the island size and leads to only marginally smaller islands. Importantly, we observe that the nucleation of larger islands in the 2$^{\text{nd}}$ layer is a general feature of DIP growth under different conditions. We relate this behavior to a significant difference between the molecule-substrate interaction (dominant during the initial stage of growth) versus the molecule-molecule interaction (dominant during the later stages of growth), which leads to a difference in the corresponding diffusion length scales.

5.3.2.3 Estimation of effective activation energies

The relevant growth kinetics within such systems may be obtained by comparing the effective activation energy of nucleation $E_{\text{act}}^{\text{eff}}$ between the 1$^{\text{st}}$ and 2$^{\text{nd}}$ layer. In this context, $E_{\text{act}}^{\text{eff}}$ is derived from the Arrhenius plot of the island diameter (or alternatively island density) versus temperature (Fig. 5.25b). The *in situ* data has been analyzed over a broad coverage regime using this approach. The different slopes in the two Arrhenius plots indicate a difference between the activation energies, and therefore also between the diffusion barriers in the 1$^{\text{st}}$ and the 2$^{\text{nd}}$ layer. In dynamical 2D-nucleation theory considering small layer coverage ($\theta_n \ll 1$), the kinetics of the island growth, i.e. the time dependence of the island size and density, is related to the flux of the incoming molecules F, the surface diffusion coefficient D, the thermal energy k_BT, and the critical nucleus size $i^\star$ [43, 185, 186]. For the first two ML we relate l to $E_{\text{act}}^{\text{eff}}$ via

$$l \propto \theta_n^{-\frac{(i^\star+1)}{2}} \left(\frac{D_0}{F}\right)^{\frac{i^\star}{2(i^\star+2)}} e^{-E_{\text{act}}^{\text{eff}}/k_BT}\ , \tag{5.19}$$

where D_0 is the diffusion pre-exponential factor. The activation energy is proportional to the diffusion barrier E_D and binding energy $E_{i^\star}$ of clusters consisting of $i^\star$ molecules and, in conventional theory, [36, 175, 179] given by $E_{\text{act}}^{\text{eff}} = (i^\star E_D + E_{i^\star})/2(i^\star + 2)$. Note that a precise determination of $E_{i^\star}$ turns out to be very difficult. Even for comparatively simple inorganic systems, like Pt grown on Pt(110), the experimentally obtained binding energy of a Pt dimer differs from those estimated by density functional calculations [36, 187, 188] by 66%. For molecular systems with shape anisotropy orientational degrees of freedom arise, which implies that even $E_{i^\star}$ (and actually in principle also E_D) are not unique numbers, since they depend on the *relative orientation* of the molecules. These issues call for an extension of the theoretical description on a fundamental level, as e.g. also seen in previous results on the growth exponents [68, 158]. Therefore, we restrict ourselves to the determination of the effective activation energy for island nucleation. The effective activation energies thus determined for different coverages are shown in Fig. 5.25c and

	R_{growth}	$E_{\text{act}}^{\text{eff}}$	$\Delta E_{\text{act}}^{\text{eff}}$
Layer 1 (DIP on SiO_x)	0.4 nm/min	0.19±0.01 eV	0.11 eV
Layer 2 (DIP on DIP)		0.08±0.01 eV	
Layer 1 (DIP on SiO_x)	1.1 nm/min	0.16±0.04 eV	0.09 eV
Layer 2 (DIP on DIP)		0.07±0.01 eV	

Table 5.2: Effective activation energy of nucleation $E_{\text{act}}^{\text{eff}}$ for the 1st and 2nd layer obtained by taking the layer-specific average of the data shown in Fig. 5.25c. The error bars for $E_{\text{act}}^{\text{eff}}$ correspond to the standard deviation of the different datasets.

summarized in Table 5.2. For both growth rates, we observe a consistent difference of $\Delta E_{\text{act}}^{\text{eff}} \approx 0.1\,\text{eV}$ between the 1st and 2nd molecular layer. This implies an increase of the diffusion length of DIP in the 2nd layer, which leads to a longer migration time of monomers and thus explains the observed formation of larger islands.

5.3.3 Summary and conclusion

We have used real-time x-ray specular and diffuse scattering to study *in situ* the dynamics of DIP thin film growth on silicon oxide, namely the thickness-dependent evolution of lattice parameters, island-size evolution and surface diffusion processes. We have introduced an improvement on the existing model for simulations of anti-Bragg growth oscillations by including the effect of the change in the molecular tilt angle during growth. We suggest that the observed molecular tilting from the transient surface induced towards the stable thin-film phase orientation is related to a change in the inter-layer transport leading to the transition to 3D-growth. Furthermore, we have used real-time GISAXS to study the island size evolution during deposition of DIP. The smaller diffusion activation energy on top of the 1st molecular layer results in a larger diffusion length and hence the formation of bigger islands than on the silicon oxide substrate, where the activation energy is $\sim 0.1\,\text{eV}$ larger. For DIP on SiO_x, this seems to be a rather general phenomenon at various growth rates and substrate temperatures.

We have provided a systematic x-ray scattering study to investigate in real-time the growth behavior of rod-like organic semiconducting molecules. The evolution of island sizes and differences of the molecular diffusion in the very first layers are important questions that need to be addressed – also for more complex systems such as binary mixtures [23, 29, 32]. Our results provide key insights into this rich field, which could be used for the development of new theoretical models of growth that go beyond the existing formalism by including shape anisotropy.

5.4 GID-GISAXS measurements on DIP:C60 blends

The results in the following section emerged from a collaboration with R. Banerjee *et al.* and were published in Ref. [32][5].

OSCs have attracted substantial research interest in recent years, in an effort to complement inorganic semiconductors, due to their attractive optical and structural properties. Several device applications, such as diodes, field-effect transistors up to all-organic integrated circuits, photodiodes, OPVs, and organic light emitting diodes have been demonstrated by OSCs based on polymers or small molecules such as C_{60}, acenes, perylene-derivatives, and phthalocyanines [4, 8, 189–193]. Since the structure and morphology have a strong influence on the performance, their control is mandatory, but the mechanisms of structure formation of OSCs and their mixtures (and indeed molecular materials in general) are not completely understood on a fundamental level [23, 68, 158, 194, 195].

One principal strategy in OPV employs the mixing of donor and acceptor molecules (bulk heterojunction) [70, 196, 197]. The resulting efficiency crucially depends on the interplay of the diffusion lengths of the excitons generated by the absorption of light and the structural length scales of the D:A mixture, such as the typical width of the D and A domains [70]. Controlling these structural length scales in D:A mixtures, which are potentially phase-separating, is thus a key point in this field. In addition to the relevance for applications, this is also a challenge for the fundamental understanding of the structural evolution of mixtures. Some comparisons can be made to the rich area of binary alloys (i.e. mixtures of elementary systems) [198] and to organic bulk crystals [199]. In the latter field, due to the different ratio of the range of interactions to the size of the objects (molecules) as well as their inherent anisotropy in shape, additional parameters have to be considered, which can lead to an even broader range of scenarios [23, 29]. An important further challenge also comes from the fact that applications of OSCs are typically based on thin films, so that issues related to their interfaces and kinetically controlled growth enter the scenario.

The main focus of the present section is the real-time and *in-situ* observation of growth as well as post-growth structural characterization of two prototypical OSCs, DIP and C_{60} (inset of Fig. 5.26a), co-evaporated in different mixing ratios. DIP and C_{60} are relevant for OPVs as a model D:A pair [19, 77]. GID was performed as a function of time during growth and also as a function of probing depth post growth, to observe the evolution of the in-plane Bragg peaks. XRR and GISAXS measurements were performed for post-growth analysis of the out-of-plane structure and in-plane domain size of the mixed films, respectively.

In this part of the thesis, it is shown that for co-evaporated DIP:C_{60}-blends with phase-separating tendency as used in OPVs, the domain size is thickness (or growth time) dependent and thus kinetically limited. The coherent crystallite grain size as well as the inter-domain distances of the mixing molecules, for a given thickness, can be tailored by

[5] R. Banerjee, J. Novák, C. Frank, C. Lorch, A. Hinderhofer, A. Gerlach, and F. Schreiber, Phys. Rev. Lett. **110**, 185506 (2013): *Evidence for kinetically limited thickness dependent phase separation in organic thin film blends.*

tuning the mixing ratio of molecules. At the same time, enhanced out-of-plane order and smoothing of the mixed films is observed compared to pure films upon co-evaporation of these mixed films in different mixing ratio. The results provide fundamentally new insight into the basic understanding of the phase separation kinetics of these systems by demonstrating the inter-correlation between the lateral and the vertical length scales (or time) with substantial implications for the theoretical understanding of OPVs.

5.4.1 Growth conditions and sample preparation

Sublimation grade DIP and C_{60} were obtained from Institut für PAH Forschung Greifenberg, Germany, with 99.9% purity, and Creaphys with 99.9% purity, respectively. Films containing DIP and C_{60} with varying mixing ratio were co-evaporated on Si wafers covered with a native oxide layer ($\sim$ 9 Å) at a base pressure $< 5\times10^{-9}$ mbar. The growth rate monitored by XRR and a quartz crystal microbalance was $\sim$0.4 nm/min. Apart from the pure films of DIP and C_{60}, five different molar mixing ratios of DIP:C_{60} (3:1, 2:1, 1:1, 1:2, 1:3) were investigated. The error in the stoichiometry of the mixtures is 10% determined by the error in the read-out of the quartz-crystal microbalance. All films for *in-situ* measurements were deposited up to a thickness of $\sim$20 nm at a substrate temperature of 25 °C. Scattering measurements (viz. XRR, time and depth-resolved GID and GISAXS) were performed at the X04SA beamline of the Swiss Light Source at a wavelength of 0.99987 Å, in a custom-built portable organic molecular beam deposition chamber [81], using a Pilatus II detector.

5.4.2 Results and Discussion

The results of the blended DIP:C60 films are presented in the following subsections, where they are organized in terms of post-growth and real-time analysis.

5.4.2.1 Post-growth analysis of the structure and morhology

XRR is used for the extraction of the electron density profile along the direction perpendicular to the sample surface and provides structural parameters like thickness and surface and interface roughness of thin films. The XRR profiles show distinct thickness oscillations for all the films and out-of-plane Bragg peaks for some of them (Fig. 5.26a). It is evident from the XRR measurements that when DIP dominates the mixture, extremely smooth films are produced. The higher the ratio of DIP in the blend, the smoother is the film (see Fig. 5.26a). For mixed thin films of DIP and C_{60}, the first Bragg peak was observed distinctly for DIP:C_{60} 3:1 ratio (henceforth called only 3:1) and 2:1. However, for 1:1, the Bragg peak is severely distorted and for further increase in the C_{60} molar concentration, i.e. for 1:2 and 1:3, the Bragg peak completely disappears. The C_{60} Bragg peak along the specular direction for pure as well as mixed films is not properly recognizable, because the C_{60} forms essentially untextured polycrystalline thin films with low structural order

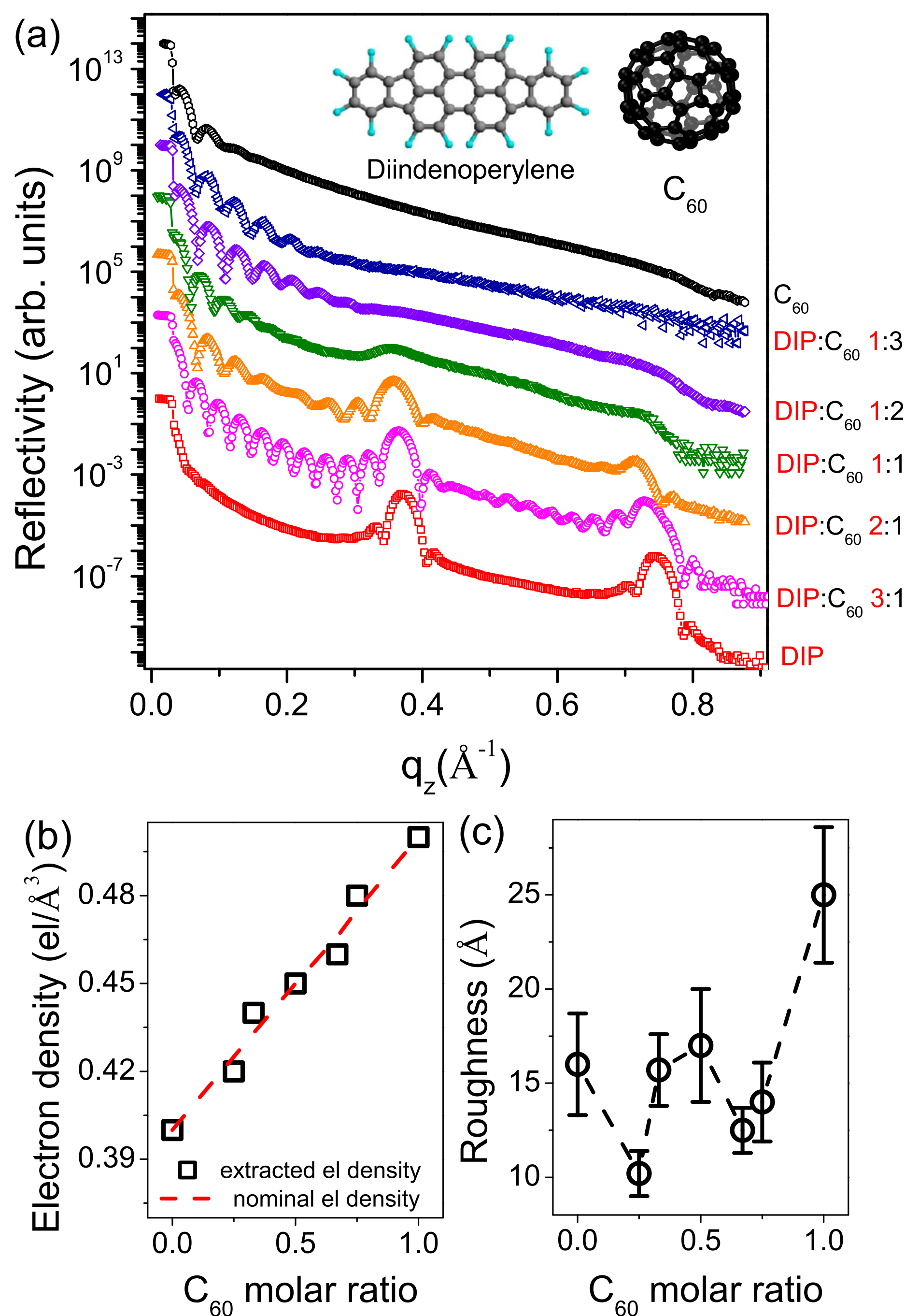

Figure 5.26: XRR profiles for the pure and the mixed films with various mixing ratios. The data have been scaled for clarity. The inset shows the molecular structure of DIP and C_{60}. (b) The average electron density derived from the fits of the XRR profiles. The dashed line shows the nominal electron density. (c) The top surface roughness and error bars derived from the XRR fits of the various films.

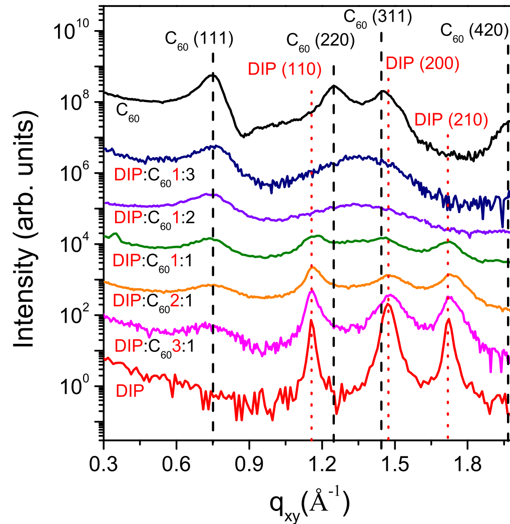

Figure 5.27: GID plots of the pure films as well as the films with varying mixing ratio. All films were ∼20 nm thick. The various peaks have been identified as either belonging to DIP thin film or C_{60} fcc thin film phases and no new or unidentified peaks were observed.

on bare Si substrates (in contrast to layered D/A heterostructures, showing a distinct C_{60}(111) Bragg peak at ∼0.75 Å^{-1}, if DIP serves as a template for C_{60} [200]).

The XRR data were fitted using the Parratt formalism [84, 97, 145] up to a value of the out-of-plane component of the momentum transfer vector (q_z) equal to 0.2 Å^{-1} to estimate the average electron density and the top layer roughness of the films. A single box model was used in order to limit the number of fitting parameters. The average electron density (ρ in el/Å^3) and the top surface roughness extracted from the XRR fits are plotted in Fig. 5.26b and Fig. 5.26c. We observe that ρ increases linearly from the value of ρ_{DIP} to the value of $\rho_{C_{60}}$ which consolidates the fact that there is no preference for either species to dominate the growth. In view of the strong tendency to phase-separate (see below), it is quite remarkable that DIP:C_{60} shows a smoothing effect upon mixing. Indeed, overall the roughness evolution appears to be non-trivial from a fundamental perspective, but its tunability *via* the mixing ratio may be exploited in applications demanding smooth interfaces.

GID probes reciprocal space at high in-plane scattering angles and provides information on the crystallinity of the samples. The post-growth GID measurements (Fig. 5.27) show the known in-plane Bragg reflections for C_{60} (rather broad, as expected) and DIP [23, 26]. The data show clear signs of phase separation since we can identify known peaks of pure DIP and C_{60} crystallites and no new or unidentified peaks even for mixed films with different ratio of mixing. Relative Bragg peak intensities from DIP and C_{60} correspond to the respective mixing ratios showing the expected predominance of the abundant species. The

peak width for DIP is also seen to increase, signifying smaller grain sizes for smaller DIP content. For the mixing ratios 1:2 and 1:3, the DIP and C_{60} peaks cannot be discriminated and result in a broad hump around the in-plane component of the momentum transfer vector $q_{xy} = 1.3\,\text{Å}^{-1}$ where the peaks are expected. From the perspective of applications in OPV, another important consideration relates to the crystallite grain sizes which is either small (hence large number of grains) or big (hence fewer) for a fixed molar mixing ratio. For a given thickness, this is expected to be tunable by substrate temperature and rate of deposition. In the active region of a bulk heterojunction composed of a phase-separating D:A pair, smaller domains increase the surface area of exposure and hence the possibility for the excitons to reach the interface (where they eventually separate), but on the other hand decrease the charge mobility and hence the charge extraction. Optimizing the efficiency would thus be a trade-off between the domain size (exciton exchange area) and the availability of percolation paths for charge transport.

GISAXS is sensitive to the morphology and preferential alignment of nanoscale objects at the surface. Additionally, it renders valuable information like the lateral correlations and sizes and shapes of nanostructures [97, 99, 145]. We observe distinct side peaks in the GISAXS measurements at different q_{xy}, depending on whether the thin film has a majority of DIP or C_{60} molecules (Fig. 5.28a – Fig. 5.28b). The line profiles obtained from post-growth GISAXS measurements are shown in Fig. 5.28a and clearly exhibit differences in the in-plane characteristic length scales for the various mixed films. For mixtures with more DIP the peak maximum is closely spaced around the specular, i.e. large in-plane length scales in real space, but for mixtures with more C_{60}, the peaks are observed at larger q_{xy} suggesting smaller in-plane length scales. For the 1:1 mixture two distinct length scales are seen which correspond to the DIP and C_{60} phases. It is also observed that the characteristic length (or island distance) of one of the mixing molecules (say C_{60}) depends on the ratio of the other (DIP) (see Fig. 5.28c). This can be exploited to prepare bulk heterojunctions with desired grain size as well as inter-domain distance.

5.4.2.2 Real-time analysis of the in-plane structure

Having established the tendency for phase-separation and the approximate in-plane correlations (island distances of the two respective components), a key question in film growth physics and for device architectures is whether this process is homogeneous or thickness-dependent. To address this issue, we focus on the 1:1 mixing ratio which has been used in devices [19, 77]. Real-time GID was performed to investigate the kinetics of phase separation during the growth process. The incident angle (θ_i) for GID measurements was 0.13° corresponding to a penetration depth of the entire film thickness. The real-time GID measurements (see Fig. 5.29) show that the GID peaks start to appear (i.e. crystallites of DIP and C_{60} start forming) only after a certain thickness and become more intense as the growth progresses. This leads to the speculation that there is a delayed onset of crystallization and phase separation until a certain thickness is reached. This is obviously kinetically determined for a non-equilibrium growth process. Also, it is intuitively plausible that the crystallization process is delayed for a statistical mixture with two dif-

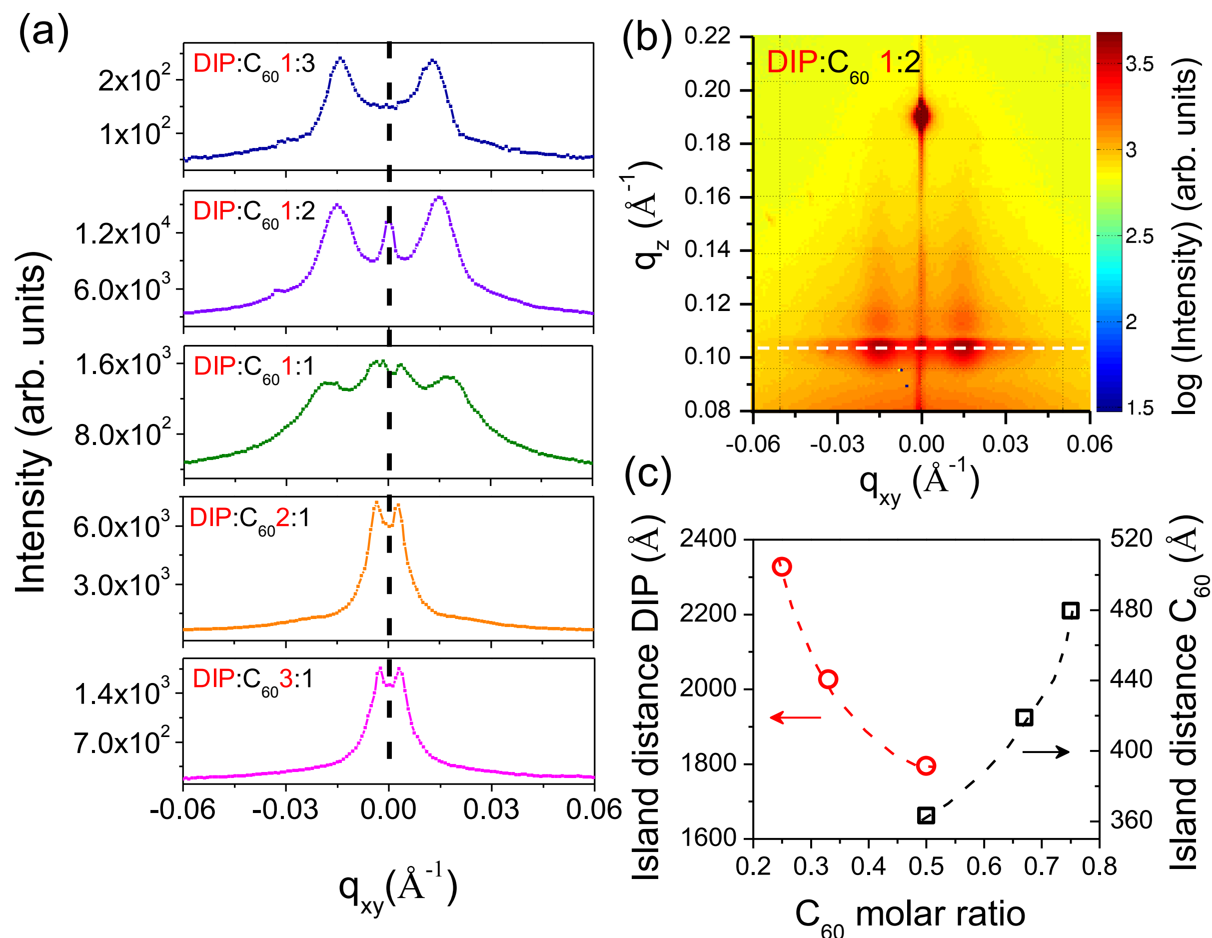

Figure 5.28: (a) GISAXS line profiles of the DIP and C_{60} mixed films at final stages of growth. The position of the correlation peak clearly indicates that the C_{60} island distances are smaller in size than the DIP islands. For the 1:1 mixture, two distinct length scales are seen corresponding to C_{60} and DIP molecules. (b) Representative GISAXS data for 1:2 mixed film. The white dashed line shows the line scan from which characteristic length scales have been derived. (c) The characteristic length scales (island distances) for DIP and C_{60} as a function of the molar ratio. The dashed lines are guide to the eye.

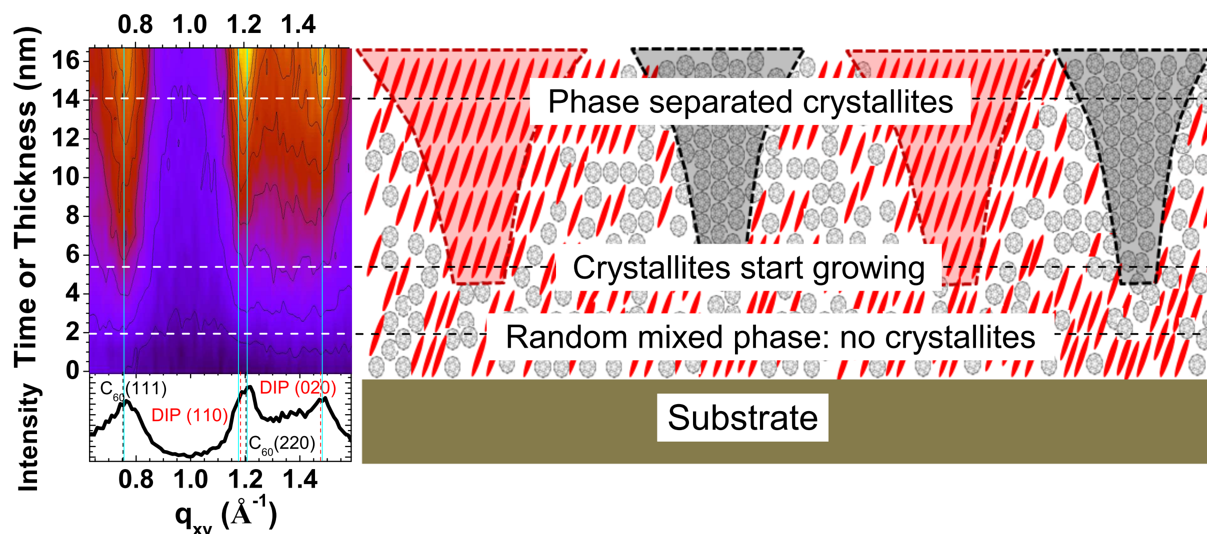

Figure 5.29: Contour plot of real-time GID data measured during growth of 1:1 mixed film. Contour lines indicate levels with equal intensity. GID data from the final thickness has been plotted at the bottom. The blue lines indicate the peak maxima. Schematic representation of the model proposed for the kinetically driven phase-separation during the growth of a co-evaporated DIP and C_{60} thin film. The molecules phase-separate into domains of crystallites which grow laterally with increasing thickness of the film.

ferent molecules than for the one with just the pristine molecule. Below this thickness, the molecules are probably still in a mixed, albeit non-crystalline phase, but as soon as this thickness is reached, they start to phase-separate and further growth of the mixed film only increases the lateral grain size of the phase-separated molecular domains. A schematic of the proposed model of growth is shown in Fig. 5.29.

To corroborate this model further and to demonstrate that the thickness-dependent lateral crystallite sizes are not a transient effect but rather prevail, post-growth *ex-situ* depth-resolved GID measurements were additionally performed on two films in ambient conditions to ensure that there is no significant post-growth structural reorganization in the mixed films. GISAXS probes the top surface structures and even by varying θ_i the buried structures cannot be easily probed due to the weak scattering contrast between DIP and C_{60}. Depth-resolved GID on the other hand probes the variation of the "coherent" lateral crystallite size at different depths of the film. For the 20 nm and 40 nm 1:1 mixed films, we performed depth-resolved GID by changing θ_i and hence the penetration depth of the impinging x-rays. Figure 5.30 shows that the peaks are better resolved at a very low penetration depth (50 Å corresponding to θ_i=0.05°), clearly indicating that the grain size at the top surface of the film is larger than near the bottom (film/substrate) interface for both films. The size of the crystallites estimated by the Scherrer formula is shown in Fig. 5.30 for DIP and C_{60} as a function of penetration depth. We already penetrate the entire film at θ_i=0.12° so the estimated crystallite size does not change on further

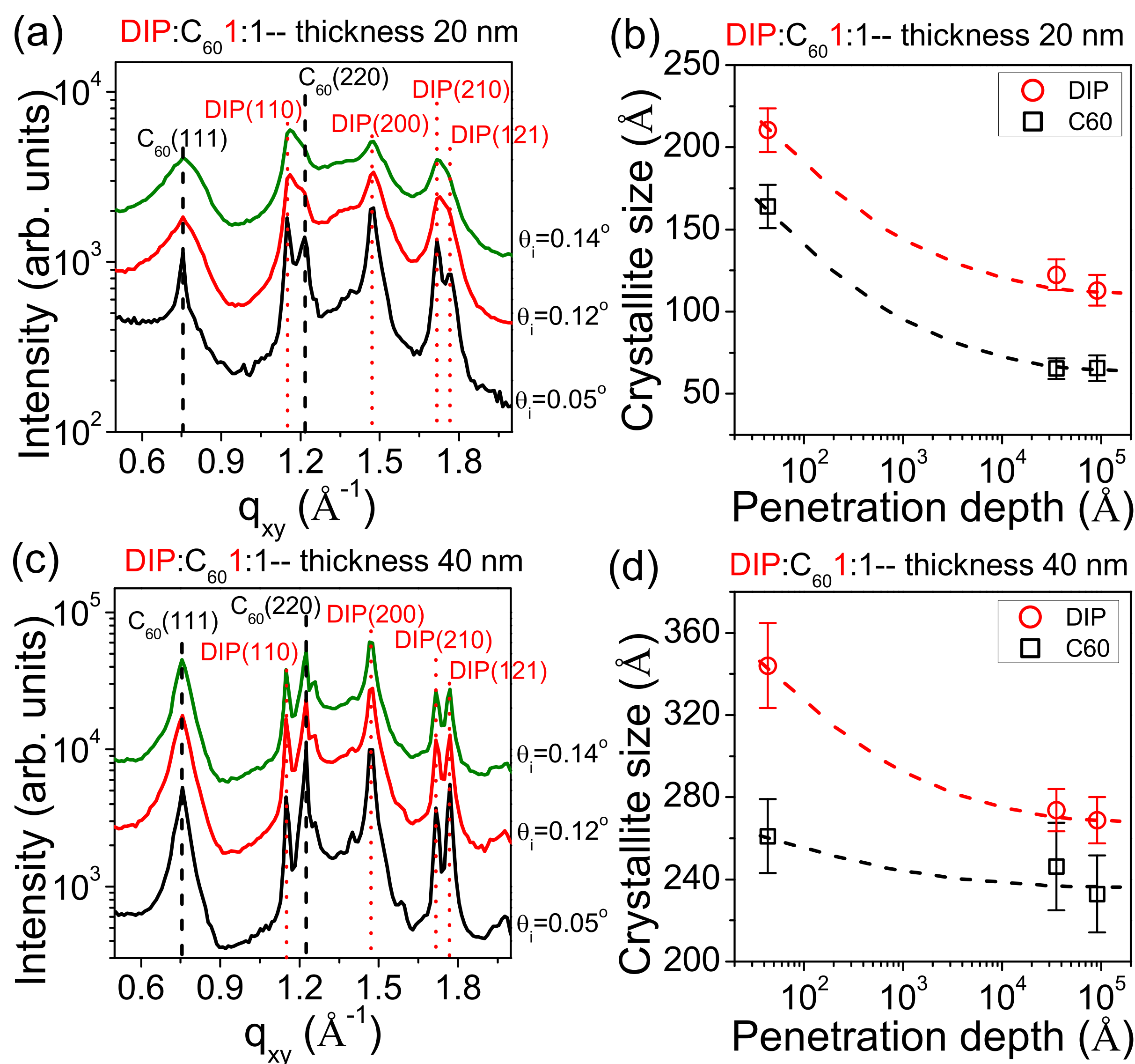

Figure 5.30: (a) Depth-resolved GID measurements of a 20 nm mixed film with ratio 1:1. (b) The average crystallite size estimated from the GID peaks using Scherrer-formula for the 20 nm film. It is observed that the crystallite at the top surface are much larger than at the bottom. (c) Depth-resolved GID measurements of a thicker (40 nm) film. Here, clear separation of the GID peaks is seen suggesting larger crystal grains for both DIP and C_{60}. (d) The average crystal grain size for the 40 nm film is much larger than that for the 20 nm film and one observes the same trend of increased grain size at the top surface. The dashed lines are guides to the eye.

increment of θ_i to $0.14\,^\circ$. For the thicker film (40 nm) we observe that the peaks are even better resolved and sharper than in the 20 nm film for the different depths of penetration. We observe larger lateral grain size for both constituents with increasing film thickness from 20 nm to 40 nm (see Fig. 5.30). The growth model (Fig. 5.29) is thus also valid for the 40 nm film but with larger crystallite grains than in the 20 nm film.

5.4.3 Summary and Conclusion

In conclusion, using surface-sensitive scattering techniques it was consistently shown that the co-evaporation of two prototypical small-molecule OSCs with a tendency for phase-separation leads to a thickness and growth-time dependent domain size. Thus, a plausible speculation is that this is a rather general phenomenon in kinetically limited growth of phase separating systems, most likely not limited to OSCs. This means that the relationship between the structural length scales and those relevant for the functioning of a device, namely exciton diffusion and carrier transport, can be vastly different for the region near the top vs. that near the bottom electrode and particular attention has to be paid to top-to-bottom asymmetry in mixed layers, as observed in this section. Qualitative agreement between real-time GID and post-growth depth-resolved GID is established which is consistent with the growth model proposed. The characteristic length-scales probed by GISAXS demonstrate clear dependence of island distances on the mixing ratio of molecules. The results may have substantial implications for the fundamental understanding of the phase separation kinetics of these systems as well as the modeling of device architectures of D:A blends.

Chapter 6

Summary and Conclusion

In this thesis we have characterized the growth of different organic materials, primarily by the use of real-time, diffuse x-ray scattering techniques. Post-growth studies often provide only a "snapshot" of the system, whereas real-time techniques allow, among other things, to follow the entire growth dynamics of the film. Here we have investigated pure, as well as mixed systems, in order to understand the kinetic issues involved, such as the structural and morphological film evolution and the molecular diffusion, which is only possible using time-resolved measurements. The following discussion summarizes our findings from Chap. 5.

6.1 Results of pristine PFP- and blended PFP:PEN films

In Sect. 5.1.3 we investigated the growth of thin films of pristine perfluoropentacene and its dependence on the substrate temperature. Real-time scattering was employed to probe the evolution of the in-plane crystal structure, which clearly depends on the film thickness. All films were grown up to 50 nm on silicon oxide, and the substrate temperature was varied between −120 °C and 60 °C. Additionally, blended films of the two sterically compatible compounds perfluoropentacene and pentacene were grown in order to extend the discussion in Sect. 5.1.3 to binary mixtures. The most important findings from Sect. 5.1 are summarized as follows:

- Along with the known thin-film phase, there is also a coexisting molecular arrangement with a unit cell having twice the size with respect to the long unit cell axis of the thin-film phase. This has been observed for the first time for PFP [33].
- Even at growth temperatures as low as −20 °C PFP shows a high degree of crystallinity in the out-of-plane direction. [33]
- The growth of PFP is characterized by a two-stage process. The molecular lattice experiences much stronger in-plane relaxation in the 0–19 nm thickness regime when compared to the 19–50 nm thickness regime [33].

- Co-deposition of PEN_x:PFP_{1-x} reveals that when PEN is in excess, nucleation of the mixed λ-phase is retarded with respect to the other crystal structures.

In conclusion, we have investigated the growth dynamics of PFP from a structural point-of-view. On the one hand, we find that the crystallinity of PFP is strongly affected by the substrate temperature only in the in-plane direction, which may potentially be a general effect for rodlike organic materials. In particular, for PFP we have explicitly determined the coherent in-plane crystal size as a function of film thickness. Thus, with regard to OSC applications, this actually allows one to tailor the in-plane crystallite size by altering the film thickness, while still having good crystallinity in the out-of-plane direction. In most electronic applications this is the relevant direction for charge transport. On the other hand, we have shown that there is evidence for different kinetic processes of crystal grain formation at low and high substrate temperatures [33]. Moreover, different functional dependence of the in-plane lattice relaxation is observed in different thickness regimes. All of these observations may be attributed to molecular diffusion processes. Yet, at present, there is no fully-developed theory to describe the growth of such anisotropic molecules. Therefore, studying the growth of such systems on a molecular level is of great interest, primarily to extend the existing growth theories.

The growth processes of mixed films are obviously even more complex in comparison to the pristine films. The simultaneous occurrence of the different structural orientations makes the analysis on a molecular level rather complex, particularly since some of these features tend to overlap at low q_z values. Thus, mixed films were only qualitatively investigated. Here, we find that below a certain film thickness the nucleation of the mixed λ-phase can be suppressed by an excessive amount of PEN. This observation is of particular relevance since it allows to study the mixed σ-phase (for low film thicknesses) at elevated substrate temperatures without the interference of a significant amount of lying molecules.

6.2 Results of pristine DIP films

This section summarizes our results from Sect. 5.2 and Sect. 5.3. In the first part (Sect. 5.2) a series of *ex situ* samples of pristine DIP was prepared on SiO_x. In contrast to the experiments in Sect. 5.1 we have limited the film thickness here on-purpose to the ultra-thin-film coverage regime, i.e. $\theta = 0.5$–$5.5\,$ML. This allows, for instance, the study of the structure and morphology during the initial stages of the growth. Furthermore, it allows one to discriminate between the molecule-substrate and molecule-molecule interaction [39]. High-resolution GISAXS measurements were performed post-growth in order to characterize the morphology of the films. This is, *inter alia*, necessary to analyze the DIP thin-film growth in real time, which was the focus of the second part (Sect. 5.3). In the following we give a short summary of the main results from the first part:

- We derive how the correlation length, which was obtained from the inverse Fourier transform of the GISAXS profiles, evolutes for the different coverages to a saturation

($\simeq 600\,\text{nm}$), and provide an explanation for how it is related to the morphology of the sample [30].

- Using small angle scattering theory derived for simple liquids and the LogFFT algorithm from Ref. [170, 171] to numerically calculate the 2D inverse-Hankel transform, we could successfully model the DIP islands, which were actually found to be in the order of $\approx 100\,\text{nm}$. Moreover, we observed a significant difference between our employed models, which was most pronounced in the kinetic roughening growth regime, i.e. 3D growth mode [30].

- At low coverages (in the layer-by-layer growth mode) we found that islands could be extremely well-modeled using the shape function of a cylinder. At higher coverages (in the 3D-growth mode) a detectable deviation from that shape is observed [30].

- AFM measurements on the same sample set corroborate the findings mentioned above [30].

Using specular and off-specular x-ray scattering in a combined way, we have studied the growth of ultra-thin films of pristine DIP, *in situ*, in the second part. In particular, we have measured the specular and the diffuse growth oscillations in real time, which allowed us to determine simultaneously the evolution of the out-of-plane structure and the in-plane morphology. DIP growth was studied with regard to different substrate temperatures and growth rates. Both parameters were varied in a relatively wide range. The results from the second part are summarized in the following:

- We studied the evolution of the in-plane correlation length and the growth kinetics of the films, including their dependence on the substrate temperature and the growth rate [31].

- We observed a temperature-dependent collective rearrangement of DIP-molecules from a transient, surface-induced phase to the stable, thin-film phase, resulting in a change of the out-of-plane lattice parameter of $\Delta d \approx 0.5\,\text{Å}$. We rationalize this by incorporating a thickness-dependent out-of-plane lattice parameter [31].

- We further observed that the nucleation behavior of DIP changes from the first to the second monolayer, which we relate to a difference in the diffusion length of the molecules and, connected with that, a difference in the effective activation energy of $\Delta E_{\text{act}}^{\text{eff}} \approx 0.1\,\text{eV}$ [31].

In conclusion, we have aimed to model the morphology of the DIP thin films in the first part. We have seen that the functional dependence of the correlation length itself provides an indication, on how the material grows. In the case of DIP, we find that the first two layers are completely filled, whereas deposition of more material leads to the formation of wedding-cake-like structures. We have modeled the form factor of the islands within the Born approximation and find that for the first two layers the shape function

of a cylinder provides a good approximation. At higher coverages, islands significantly deviate from that shape. Importantly, we use this model, i.e. cylinderlike islands within the first two layers, as a feedback to analyze the real-time data in the second part. The morphology observed in the first part is confirmed in the second part, as expected. Using the description of cylindrically-shaped islands, we investigated the growth kinetics within the first two layers. Note that only a few ML of DIP were grown, either close to room temperature or at elevated substrate temperatures, with the measurements performed *in situ*. Thus, we can exclude the occurrence of the DIP λ-phase [65], which would potentially complicate the analysis. Furthermore, we have no evidence that kinetic effects such as a potential post-growth structural reorganization or rapid roughening [66–68] are of relevance here. Excluding these kinetic effects and a potential polymorphism, we could quantitatively analyze the effective activation energies of diffusion in the first and the second layer. We conclude that due to an increase of the diffusion length of the DIP molecules in the second layer, the migration time of monomers is increased, leading to larger islands as compared to the first layer. Furthermore, we observed molecular rearrangement with respect to the out-of-plane directions from a substrate-induced thin-film phase to the stable thin-film phase, which typically occurs after completion of the second layer. This observation along with the formation of 3D-islands, both occurring simultaneously, demonstrates in which range the molecule-substrate interaction (at least for DIP grown on SiO_x) is of relevance.

We emphasize, again, that this kind of data analysis was based on simplified assumptions, since, at present there is no theory available that considers the shape-anisotropy of the molecules. As a consequence, the involved energy barriers, such as the ES-Barrier, the diffusion barrier and the binding energy of the molecular clusters, should, in principal not be treated as scalar numbers, but rather as tensor objects taking into account the relative orientation of the molecules. This is particularly true when studying growth on inter-molecular length-scales. Opposed to the experiments performed in this thesis the growth of isotropic molecules can be treated in a much simpler way, as recent studies on the growth of pure C_{60} demonstrate. Owing to the fact that orientational degrees of freedom are in this case not relevant, kinetic Monte Carlo simulations allow for a quantitative determination of the molecular dynamics and the involved energy barriers [201]. In this context, the development of growth theories involving anisotropic molecules (representing the majority of organic materials), is regarded as a prime objective.

In view of the discussion of the GISAXS analysis in Chap. 5, it might be quite instructive to conclude this section with a few comments on *x-ray cross correlations*. Cross correlation analysis has, for instance, recently been employed to study x-ray speckle patterns observed in disordered matter such as in colloidal glasses and semi-crystalline polymers [202,203]. Using higher order correlation functions one can reveal locally hidden symmetries, which are otherwise difficult to confirm. For instance, in the case of the Polymer system investigated (in transmission mode) in Ref. [202], namely polymethylmethacrylate (PMMA) colloidal particles in a suspension with $\sim 20-30\,\%$ volume fraction, the authors could observe a local five-fold symmetry, which is usually forbidden in crystalline systems except in quasi-crystals [204]. In order to check our GISAXS data for the occurrence

of such speckle patterns, horizontal line sections were extracted (as shown in Chap. 5) and the intensity fluctuations compared with the statistical noise level. Notably, we observed that the intensity fluctuations are of the same order than the statistical noise (see Fig. 7.3), thus demonstrating that x-ray speckles are not present in our GISAXS data. We may speculate that the reasons behind, can, for instance, either be related to the different scattering geometry employed in our experiment or that a higher degree of beam coherence is necessary to observe such speckles.

6.3 Results of blended DIP:C60 films

In Sect. 5.1 we investigated some of the kinetic aspects of thin-film growth of the two sterically compatible materials perfluoropentacene and pentacene. If co-evaporated, both constituents tend to form mixed polymorphs, which potentially arises from a large interaction energy between both species [28]. Henceforth, we want to extend this discussion to binary mixtures consisting of geometrically very differently-shaped molecules, namely diindenoperylene and buckminsterfullerene C_{60}, which is achieved by employing the previously-introduced scattering techniques, i.e. real-time GID and GISAXS, in combination with the analysis from the preceding chapters. As a consequence of this steric incompatibility of the two materials (DIP:C_{60}), we expected that this system would adopt a strong tendency for phase separation. Hence, in Sect. 5.4 we have grown several DIP:C_{60} molar mixtures of $\sim$ 20 nm thickness at about room temperature, while changing the mixing ratios (3:1,2:1,1:1,1:2,1:3). The growth was followed in real time using GID. Post-growth measurements comprise of GISAXS, XRR and depth resolved GID. In the following we summarize the main results from Sect. 5.4:

- We observed enhanced out-of-plane order and smoothening of the mixed films compared to pure films upon co-evaporation of DIP:C_{60} thin films in the different mixing ratios [32].
- Real-time, *in situ* GID measurements showed the kinetics and thickness dependence of phase separation, which appears to proceed only after a certain thickness [32].
- The crystallite grain size of the individual phase-separated components is significantly larger at the top of the film than at the bottom [32].

The aim of chapter 5.4 was to study the growth kinetics of binary mixtures, favoring phase separation, from a structural perspective. In general, phase separation is a scenario used in many OSC based applications, in which D:A interfaces are of interest. From our studies, we have seen that the stoichiometry of our organic systems critically depends on the film thickness. In particular, for the DIP:C_{60} 1:1 blend we find that below a critical thickness of $\sim$ 5 nm both constituents most likely form a mixed, but non-crystalline phase (similar to a “regular solution model” [29]). Above this thickness crystalline grains start forming for the different materials characterized here by a top-to-bottom asymmetry of the grains in the mixed layers. Potential implications can be found for the phase-separation

kinetics of active layers consisting of D:A blends such as used in OPV devices, where the effective structural length-scales and those on which exciton diffusion and electronic transport occur, can be different in the regions close the electrodes (where holes and electrons are collected).

6.4 Outlook

In view of the previous discussion, we find that there are still open issues summarized in the following:

- In Sect. 5.1 we analyze the growth of PFP:PEN blends in real-time. We emphasize that a clear discrimination between the mixed σ- and λ-phase turns out to be difficult since the respective features overlap in the RSM. We suggest here to determine the thin-film crystal structure of the mixed σ-phase. This can be realized by growing very thin PFP:PEN mixtures (at elevated temperatures) with an excess of PEN, where the nucleation of the λ-phase is suppressed and a discrimination is not necessary.

- In Sect. 5.3 we observe a difference of the effective diffusion-barrier between the first and second layer, which we attribute to a difference in the molecule-substrate and molecule-molecule interaction. We suggest analyzing this in more detail, using, for example different substrates to modify the molecule-substrate interaction. This would potentially require much effort, since along with the substrate also the temperature and the growth rate are system parameters. Yet, the information obtained may, for instance, be used as "real-world" input parameters for kinetic Monte Carlo simulations, taking molecular shape anisotropy into account [205].

- We believe that the established atomistic growth theories describing diffusion, nucleation and coalescence of isotropic particles are not adequate in their current stage, i.e to fully describe the growth of small organic molecules. This comes, *inter alia*, from the fact that the anisotropy of such molecules is presently not considered. Consequently, atomistic parameters, such as the Ehrlich-Schwoebel barrier or diffusion energies, would not just be scalar numbers, but rather depend on the relative orientation of the molecules. A refinement of the present theories is necessary, also in order to compare relevant system parameters with kinetic Monte Carlo simulations.

Chapter 7

Appendix

A few issues from Chap. 5 were intentionally skipped in order to focus the discussion on the relevant points. Henceforth, we will briefly address those issues in the following sections.

7.1 Form factors for simple island shapes

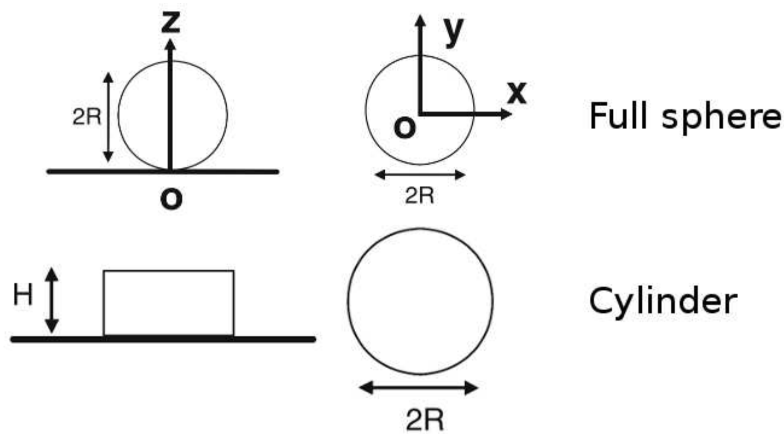

Figure 7.1: Island shape of a full sphere (top) and a cylinder (bottom) shown from the side-view (left panel) and from the top-view (right panel). Drawings of the island shapes were taken from Ref. [97].

In the following, we illustrate how the form factor of a full sphere and a cylinder, both having a uniform density, can be derived analytically (see also Fig. 7.1). For a summary of shapes commonly used in the GISAXS theory and their corresponding form factors see also Ref. [97].

7.1.1 Form factor of a full sphere

Owing to the symmetry of the full sphere with radius R (see Fig. 7.1), one can use a spherical coordinate system with azimuthal angle ϕ and inclination angle θ. With r, q being the absolute values of the vectors $\mathbf{r}$ and $\mathbf{q}$ we can rotate the coordinate system to obtain $\mathbf{q} \cdot \mathbf{r} = qr\cos\theta$, where the angle θ is defined between $\mathbf{r}$ and $\mathbf{q}$. Following the notation in Ref. [97], the form factor F is generally defined as

$$F = \int_s d\mathbf{r}\, \Omega_s e^{i\mathbf{q}\cdot\mathbf{r}} \ , \tag{7.1}$$

which using the shape function Ω_s of a unit sphere, i.e.

$$\Omega_s = u(R-r) = \begin{cases} 1 & : r < R \\ 0 & : r > R \end{cases} \tag{7.2}$$

can be expressed as

$$\begin{aligned} F &= \int_0^{2\pi} d\phi \int_0^{\pi} d\theta \int_0^{R} dr\, r^2 e^{iqr\cos\theta} \sin\theta \\ &= 2\pi \int_{-1}^{1} du \int_0^{R} dr\, r^2 e^{iqru} \\ &= \frac{4\pi}{q} \int_0^{R} dr\, r \sin qr \ . \end{aligned} \tag{7.3}$$

In the second line of Eq. (7.3), we have introduced the substitution $u \equiv \cos\theta$. Finally, Eq. (7.3) can be analytically solved using partial integration, which leads to

$$\begin{aligned} F &= \frac{4\pi}{q} \left\{ \left[\frac{-r}{q} \cos qr \right]_0^R + \int_0^R dr\, \frac{1}{q} \cos qr \right\} \\ &= \frac{4\pi}{q} \left[\frac{-R}{q} \cos qR + \frac{\sin qR}{q^2} \right] \\ &= 4\pi R^3 \left[\frac{\sin qR - qR\cos qR}{(qR)^3} \right] \\ &= 4\pi R^3 \frac{j_1(qR)}{qR} \ . \end{aligned} \tag{7.4}$$

Note that in the last line of Eq. (7.4) we have employed the definition of the spherical Bessel function of the first kind $j_1(x)$ (see e.g. Ref. [206]), which is related to the Bessel function of the first kind $J_1(x)$ by

$$j_1(x) = \sqrt{\frac{\pi}{2x}} J_{3/2}(x) \ . \tag{7.5}$$

7.1.2 Form factor of a cylinder

The form factor of a cylinder with radius R and height H (see Fig. 7.1) can be derived following the description in Sect. 7.1.1. Accordingly, we use a cylindrical coordinate system with azimuthal angle ϕ, in-plane component $\rho = \sqrt{x^2 + y^2}$ and out-of-plane component z. The in-plane and out-of-plane components of the momentum transfer are then given as $q_{||} = \sqrt{q_x^2 + q_y^2}$ and q_z, respectively. Exploiting the radial symmetry of the cylinder, we can rotate the coordinate system to obtain $\mathbf{q} \cdot \mathbf{r} = q_{||}\rho \cos\phi + q_z z$. The shape function of a cylinder is given by

$$\Omega_s = u(R-\rho) \cdot \mathrm{rect}\left(\frac{z - H/2}{H}\right) ,$$

$$u(R-\rho) = \begin{cases} 1 & : \rho < R \\ 0 & : \rho > R \end{cases} \qquad \mathrm{rect}\left(\frac{z-H/2}{H}\right) = \begin{cases} 1 & : |z| < H/2 \\ 0 & : |z| > H/2 \end{cases} \tag{7.6}$$

Hence, we obtain for the form factor

$$\begin{aligned} F &= \int_0^\infty \int_0^{2\pi} d\phi\, d\rho\, \rho u(R-\rho) e^{iq_{||}\rho\cos\phi} \int_{-\infty}^{\infty} dz\, \mathrm{rect}\left(\frac{z-H/2}{H}\right) e^{iq_z z} \\ &= \int_0^R d\rho\, \rho \int_0^{2\pi} d\phi\, e^{iq_{||}\rho\cos\phi} \int_{-H/2}^{H/2} dz\, e^{iq_z z} , \end{aligned} \tag{7.7}$$

i.e. the integration in Eq. (7.7)can be split into the in-plane (ρ, ϕ) and the out-of-plane (z) component. We will refer to this in the following as part I and II. Using the integral representation of the Bessel function of the first kind and zeroth order [206]

$$J_0(x) = \frac{1}{\pi} \int_0^\pi d\phi\, e^{ix\cos\phi} \tag{7.8}$$

we obtain for part I

$$\begin{aligned} I &= 2\pi \int_0^R d\rho\, \rho J_0(q_{||}\rho) \\ &= 2\pi \int_0^1 du\, uR^2 J_0(q_{||}Ru) , \end{aligned} \tag{7.9}$$

in which we have already introduced the substitution $u \equiv \rho/R$. Since the derivative of J_n is given by

$$\frac{dJ_n(x)}{dx} = -\frac{n}{x} J_n(x) + J_{n-1}(x) \tag{7.10}$$

we find that

$$\frac{d}{du}\left[uJ_1(q_{||}Ru)\right] = uq_{||}RJ_0(q_{||}Ru) . \tag{7.11}$$

Therefore, using the fundamental theorem of calculus we can easily solve Eq. (7.9) with Eq. (7.11), yielding

$$\begin{aligned} I &= 2\pi \frac{R}{q_{||}} \int_0^1 du \, \frac{d}{du} \left[u J_1(q_{||} R u) \right] \\ &= 2\pi R^2 \frac{J_1(q_{||} R)}{q_{||} R} \; . \end{aligned} \tag{7.12}$$

Furthermore, introducing $\mathrm{sinc}(x) := \sin x / x$ part II can be solved according to

$$\begin{aligned} II &= \int_{-H/2}^{H/2} dz \, e^{i q_z z} \\ &= \left[\frac{1}{i q_z} e^{i q_z z} \right]_{-H/2}^{H/2} \\ &= H \mathrm{sinc} \left(q_z H / 2 \right) \end{aligned} \tag{7.13}$$

Therefore, we obtain for the form factor of the cylindrically shaped islands with uniform density

$$F = I \cdot II = 2\pi R^2 H \frac{J_1(q_{||} R)}{q_{||} R} \mathrm{sinc} \left(\frac{q_z H}{2} \right) \; . \tag{7.14}$$

7.2 MATLAB codes

This section provides MATLAB routines used to calculate the Hankel transform. The script “test_hankeltrafo.m” is called to perform the numerical Hankel transform on the test function $y(x) = \exp(-x^2)$, which is subsequently compared with its analytic solution $y(k) = 0.5 * \exp(-k^2/4)$. The other MATLAB functions shown in this section are subroutines called within the Hankel transform script. Our fits from Sect. 5.2 are based on the here provided set of MATLAB routines.

test_hankeltrafo.m:

```
%% This performs a hankel transform and inverse hankel transform
% on the test function pair:
% y=exp(-x^2)    <--->    Y=0.5*exp(-k^2/4)
% Thumb-rule for cut-offs (to get rid of oscillations from aliasing
% effect): dx*N~40 lower cut-off ~0.1
%%
clear all;
N=1024;
dx=0.01;
```

```
dk=2*pi/(N*dx);
nhalf=fix(N/2);
r10=1;  %set ro to 1. This defines k0 for low ringing condition
%% initialize k-grid. Note, that matlab indices start from 1!!
ind=0:nhalf;
k=zeros(nhalf+1,1);
x(ind+1)=ind*dx;
k(ind+1)=ind*dk;
ind=2:nhalf;
x(nhalf+ind)=-(nhalf-ind+1)*dx;
k(nhalf+ind)=-(nhalf-ind+1)*dk;
%% define function on log x-grid
f=exp(-(r10*exp(x)).^2);
figure(2);plot(r10*exp(x),f,'.')
%% perform Hankel-transform and compare with test function
[HT,r20]=hankeltransform(f,x,k,dx,dk,1,N,r10);
figure(3);plot(r20*exp(x),HT,'+b',r20*exp(x), ...
exp(-(r20*exp(x)).^2/4)/2,'xr','MarkerSize',4);
xlim([0 3]);
%% perform inverse Hankel-transform and compare with input function
[iHT,r20]=hankeltransform(HT,x,k,dx,dk,-1,N,r10);
figure(4);plot(r10*exp(x),f,'+b',r10*exp(x),iHT,'xr','MarkerSize',4);
```

hankeltransform.m:

```
%numerical evaluation of hankel transform (of first order) using
%FFT on a logarithmic grid
%see also refs PRE 79, 061402 (2009) and
%Mon. Not. R. Astron. Soc. 312, 257-284 (2000)
%Parameter: f(x):   function to transform
%           x:      spatial coordinate
%           HT(k):  transformed function
%           p:      order of bias
%           dir:    1 for HT[f], -1 for HT^-1[f]
function [HT,r20] = hankeltransform( f,x,k,dx,dk,dir,N, r0 )
q=0;  %Note: Transform for arbitrary p are not implemented yet.
      % Set this to 0
nhalf=fix(N/2);
[um,k0]=uminit( k,q,r0,dx,nhalf);
%% check whether parameters are ok
if dir==1
```

```
    r10=r0;
    r20=k0;
elseif dir==-1
    r10=k0;
    r20=r0;
else
    display('ERROR: Please specify 1 or -1 for HT or HT^-1 !');
    return;
end
%% evaluate function on log grid
h1=f.*(r10*exp(x)).^(1-q);
%% perform hankel transform
h2=conj(fft(h1,N)*dx).*um';
h1=ifft(h2,N)*dk/(2*pi)*N;
HT=h1.*(r20.*exp(x)).^(-1-q);
end
```

uminit:

```
function [ um, k0 ] = uminit( k,q,r0,dx,nhalf)
%FUNCTION initializes um vector, which is necessray for Hankel transform.
%See Mon. Not. R. Astron. Soc. 312, 257-284 (2000) for description
%% determine k0 from low ringing condition (integer m==0)
um=zeros(2*nhalf,1);
c1=cgammaln((1+ q + 1i*k(nhalf+1))/2);
c2=cgammaln((1- q - 1i*k(nhalf+1))/2);
c=exp(c1-c2)*2^(q + 1i*k(nhalf+1));
r1=atan(imag(c)/real(c));
if real(c)<0
    r1 = r1+pi;
end
k0=exp(dx*r1/pi)/r0;
%% determine um
ind=1:nhalf;
c1=cgammaln((1+q)/2);
c2=cgammaln((1-q)/2);
um(1)=exp(c1-c2)*2^q;           %calculate um(m=0)
c1=(cgammaln((1+q+1i*k(ind+1))/2));
c2=(cgammaln((1-q-1i*k(ind+1))/2));
um(ind+1)=2.^(q+1i*k(ind+1)).*exp(c1-c2).*(k0*r0).^(-1i* k(ind+1));
um(2*nhalf-ind+1)=conj(um(ind+1));  %matlab indexing starts from 1
end
```

cgammaln:

```
function [ y ] = cgammaln( z )
%Calculation of COMPLEX gamma function according to the Lanczos
%approximation. See numerical receipes.
cof=[57.1562356658629235, -59.5979603554754912, ...
      14.1360979747417471, -0.491913816097620199, ...
      0.339946499848118887e-4, 0.465236289270485756e-4, ...
    -0.983744753048795646e-4, 0.158088703224912494e-3, ...
    -0.210264441724104883e-3, 0.217439618115212643e-3, ...
    -0.164318106536763890e-3, 0.844182239838527433e-4, ...
    -0.261908384015814087e-4, 0.368991826595316234e-5];

if (z<=0)
    display('ERROR: Bad argument of cgammaln! Re(Z)>0 expected!');
    return;
end
tmp=z+5.24218750000000000;
tmp=(z+0.5).*log(tmp)-tmp;
ser= 0.999999999999997092;          %corresponds to c_0
for i=1:length(cof)
    ser=ser+cof(i)./(z+i);          %sum over all coefficients
end
y=tmp+log(2.5066282746310005*ser./z);
end
```

7.3 Anti-Bragg fits

For the sake of a complete representation of our data, Fig. 7.2 shows all of the specular growth oscillations for various growth conditions along with the anti-Bragg fits from Sect. 5.3.2.

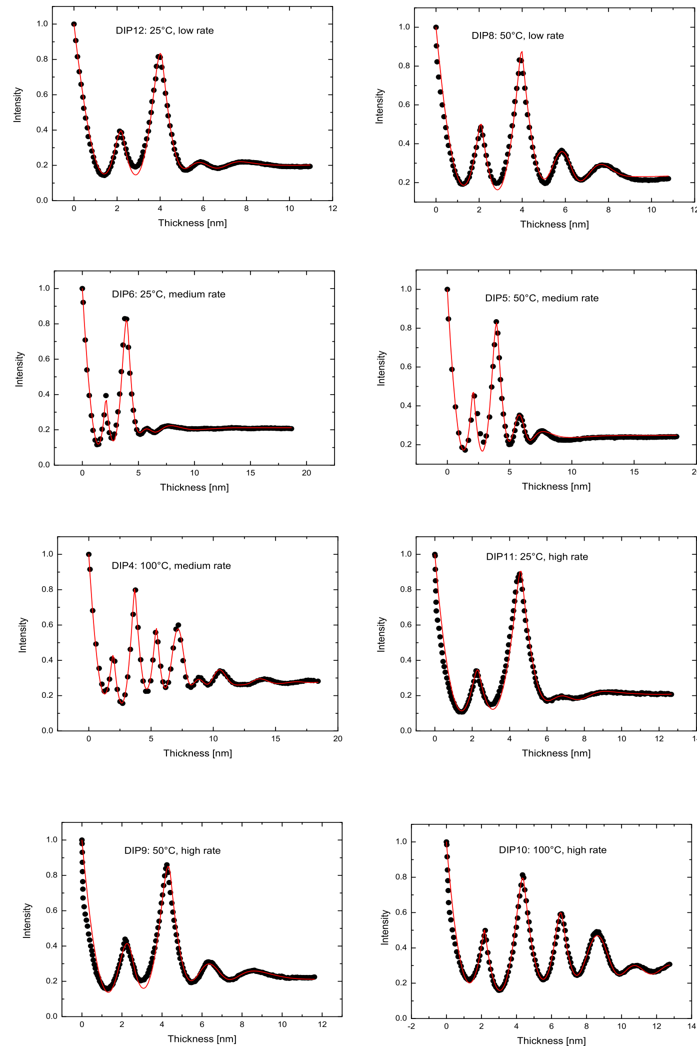

Figure 7.2: Anti-Bragg fits obtained with the model from Sect. 5.3 taking a thickness dependent out-of-plane lattice parameter into account. Fits (red lines) are shown for different growth rates and substrate temperatures. The corresponding data (solid dots) were entirely recorded at the beamline ID10B at the ESRF. The fits are shown for all available samples.

7.4 GISAXS line profiles

To check whether x-ray speckle patterns can be observed in our samples (see discussion in Sect. 6.2), GISAXS line profiles are extracted at three different q_z values.

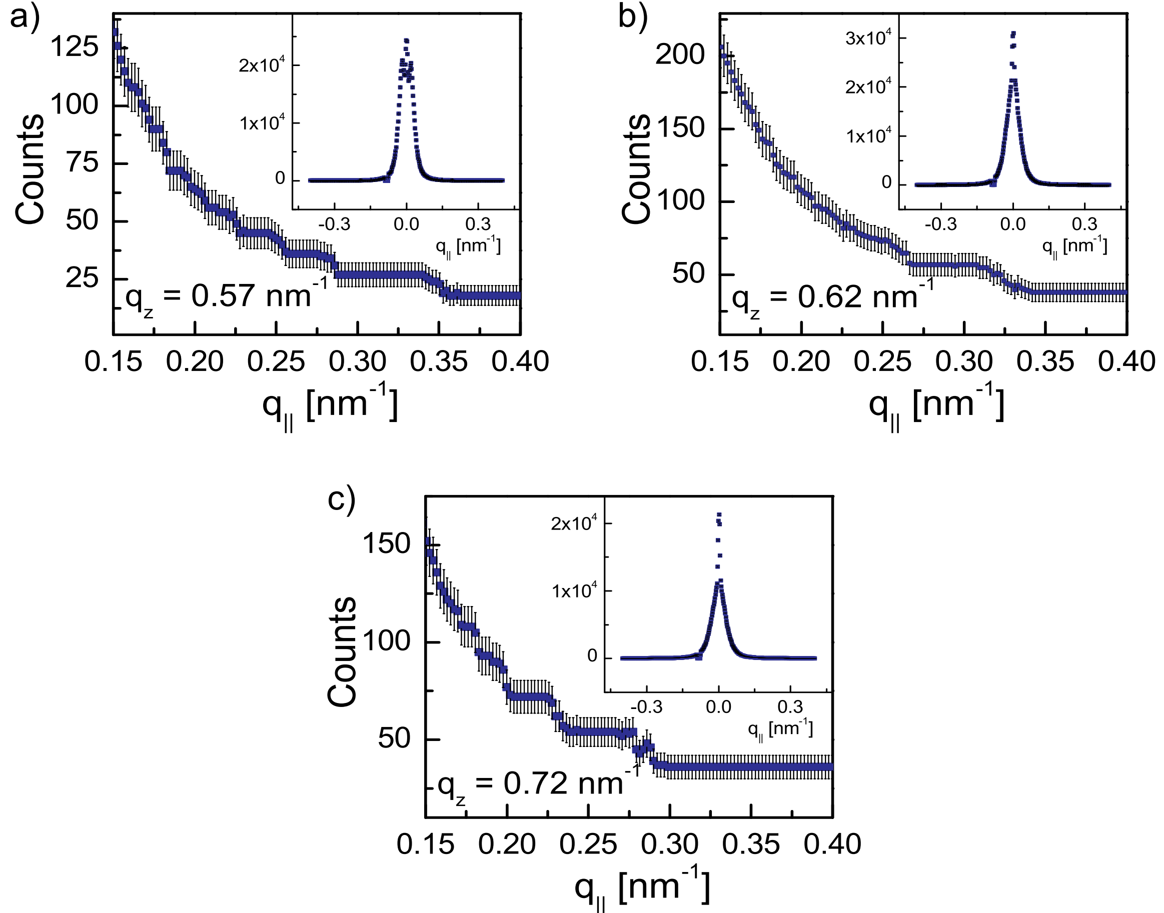

Figure 7.3: Horizontal line profiles extracted from a single shot GISAXS signal corresponding to an *ex situ* sample of 20 nm DIP grown on SiO_x. The GISAXS signal was recorded at the P03 beamline at the PETRA III storage-ring at DESY, where it was exposed to x-rays for ~ 1 s. Sections were extracted at: a) $q_z = 0.57\,\mathrm{nm}^{-1}$, b) $q_z = 0.62\,\mathrm{nm}^{-1}$, and c) $q_z = 0.72\,\mathrm{nm}^{-1}$. Error-bars in (a–c) mark the noise level of the measurement, which is given by the Poisson statistics. Sub-figures (a–c) illustrate that the intensity fluctuations are not caused by speckles, but rather occur within the statistical noise.

List of Acronyms

A acceptor

AFM atomic force microscopy

BA Born approximation

C_{60} buckminsterfullerene C_{60}

CCD charged-coupled-device

D donor

DIP diindenoperylene

DWBA distorted wave Born approximation

ES-Barrier Ehrlich-Schwoebel-Barrier

FFT fast Fourier transform

GID grazing incidence diffraction

GISAXS grazing incidence small angle X-ray scattering

OFET organic-field-effect-transistor

OLED organic-light-emitting-diode

OMBD organic molecular beam deposition

OPV organic-photovoltaic

OSC organic-molecular-semiconductor

PEN pentacene

PFP perfluoropentacene

RSM reciprocal space map

SiO_x silicon oxide

SPC single-photon-counting

UHV ultra-high vacuum

XRR x-ray reflectivity

Nomenclature

D' inter-layer diffusion

D intra-layer diffusion

L sample-detector distance

Δx pixel width

α_f exit angle

α_i incidence angle

δ' horizontal position of the area detector

δ in-plane scattering angle

γ' vertical position of the area detector

λ wavelength of the experiment

ϕ in-plane scattering angle

σ_s^c adatom capture number

σ surface roughness

d_n out-of-plane lattice spacing

d_s in-plane coherent island-size

d_{coh} coherent film thickness

d_{tot} total film thickness

k wavenumber

l length of the sample

$r_{\max}$ maximal resolvable island size parallel to the sample plane

w width of the beam

2D-FFT two dimensional fast Fourier transformation

CPD channels per degree of the area detector

FWHM full width at half maximum

HHCF height-height correlation function

ROI region of interest

Bibliography

[1] A. Pochettino, Accad. Lincei Rend **15**, 355 (1906): *Sul comportamento foto-elettrico dell'antracene*.

[2] M. Volmer, Ann. Phys. **40**, 775 (1913): *Different Photoelectric Phenomena in Anthracene, their Relation to one another, to Fluorescence and to the Formation of Dianthracene*.

[3] H. Kallmann and M. Pope, J. Chem. Phys. **30**, 585 (1959): *Photovoltaic Effect in Organic Crystals*.

[4] P. Peumans, S. Uchida, and S. R. Forrest, Nature **425**, 158 (2003): *Efficient bulk heterojunction photovoltaic cells using small-molecular-weight organic thin films*.

[5] S. R. Forrest, Nature **428**, 911 (2004): *The path to ubiquitous and low-cost organic electronic appliances on plastic*.

[6] S. M. Falke, C. A. Rozzi, D. Brida, M. Maiuri, M. Amato, E. Sommer, A. De Sio, A. Rubio, G. Cerullo, E. Molinari, and C. Lienau, Science **344**, 1001 (2014): *Coherent ultrafast charge transfer in an organic photovoltaic blend*.

[7] M. Schwoerer and H. C. Wolf, *Organic Molecular Solids* (2006).

[8] W. Brütting and C. Adachi, *Physics of Organic Semiconductors* (2012).

[9] S. Ahmad, J. Polym. Eng. **34**, 279 (2014): *Organic semiconductors for device applications: current trends and future prospects*.

[10] A. Dodabalapur, L. Torsi, and H. E. Katz, Science **268**, 270 (1995): *Organic Transistors: Two-Dimensional Transport and Improved Electrical Characteristics*.

[11] F.-J. M. Zu Heringdorf, M. Reuter, and R. Tromp, Nature **412**, 517 (2001): *Growth dynamics of pentacene thin Films*.

[12] A. C. Dürr, N. Koch, M. Kelsch, A. Rühm, J. Ghijsen, R. L. Johnson, J.-J. Pireaux, J. Schwartz, F. Schreiber, H. Dosch, and A. Kahn, Phys. Rev. B **68**, 115428 (2003): *Interplay between morphology, structure, and electronic properties at diindenoperylene-gold interfaces.*

[13] G. Witte and C. Wöll, J. Mater. Res. **19**, 1889 (2004): *Growth of aromatic molecules on solid substrates for applications in organic electronics.*

[14] Y. Sakamoto, T. Suzuki, M. Kobayashi, Y. Gao, Y. Inoue, and S. Tokito, Mol. Cryst. Liq. Cryst. **444**, 225 (2006): *Perfluoropentacene and Perfluorotetracene: Syntheses, Crystal Structures, and FET Characteristics.*

[15] S. A. Wolf, D. D. Awschalom, R. A. Buhrman, J. M. Daughton, S. von Molnár, M. L. Roukes, A. Y. Chtchelkanova, and D. M. Treger, Science **294**, 1488 (2001): *Spintronics: A Spin-Based Electronics Vision for the Future.*

[16] S. Sanvito, Nat. Mater. **6**, 803 (2007): *Organic electronics: Spintronics goes plastic.*

[17] J. Shinar and R. Shinar, J. Phys. D: Appl. Phys. **41**, 133001 (2008): *Organic light-emitting devices (OLEDs) and OLED-based chemical and biological sensors: an overview.*

[18] W. Cao and J. Xue, Energy Environ. Sci. **7**, 2123 (2014): *Recent progress in organic photovoltaics: device architecture and optical design.*

[19] J. Wagner, M. Gruber, A. Hinderhofer, A. Wilke, B. Bröker, J. Frisch, P. Amsalem, A. Vollmer, A. Opitz, N. Koch, F. Schreiber, and W. Brütting, Adv. Funct. Mater. **20**, 4295 (2010): *High Fill Factor and Open Circuit Voltage in Organic Photovoltaic Cells with Diindenoperylene as Donor Material.*

[20] Z. H. Xiong, D. Wu, Z. V. Vardeny, and J. Shi, Nature **427**, 821 (2004): *Giant magnetoresistance in organic spin-valves.*

[21] J. Ouyang, C.-W. Chu, C. R. Szmanda, L. Ma, and Y. Yang, Nat. Mater. **3**, 918 (2004): *Programmable polymer thin film and non-volatile memory device.*

[22] J. C. Scott and L. D. Bozano, Adv. Mater. **19**, 1452 (2007): *Nonvolatile Memory Elements Based on Organic Materials.*

[23] A. Hinderhofer and F. Schreiber, ChemPhysChem **13**, 628 (2012): *Organic-Organic Heterostructures: Concepts and Applications.*

[24] S. Kowarik, A. Gerlach, S. Sellner, L. Cavalcanti, O. Konovalov, and F. Schreiber, Appl. Phys. A Mater. **95**, 233 (2009): *Real-time X-ray diffraction measurements of structural dynamics and polymorphism in diindenoperylene growth.*

[25] A. R. Woll, T. V. Desai, and J. R. Engstrom, Phys. Rev. B **84**, 075479 (2011): *Quantitative modeling of in situ x-ray reflectivity during organic molecule thin film growth.*

[26] M. A. Heinrich, J. Pflaum, A. K. Tripathi, W. Frey, M. L. Steigerwald, and T. Siegrist, J. Phys. Chem. C **111**, 18878 (2007): *Enantiotropic Polymorphism in Diindenoperylene.*

[27] C. Weber, C. Frank, S. Bommel, T. Rukat, W. Leitenberger, P. Schäfer, F. Schreiber, and S. Kowarik, J. Chem. Phys. **136**, 204709 (2012): *Chain-length dependent growth dynamics of n-alkanes on silica investigated by energy-dispersive x-ray reflectivity in situ and in real-time.*

[28] A. Hinderhofer, C. Frank, T. Hosokai, A. Resta, A. Gerlach, and F. Schreiber, J. Chem. Phys. **134**, 104702 (2011): *Structure and morphology of coevaporated pentacene-perfluoropentacene thin films.*

[29] A. Aufderheide, K. Broch, J. Novák, A. Hinderhofer, R. Nervo, A. Gerlach, R. Banerjee, and F. Schreiber, Phys. Rev. Lett. **109**, 156102 (2012): *Mixing-Induced Anisotropic Correlations in Molecular Crystalline Systems.*

[30] C. Frank, R. Banerjee, M. Oettel, A. Gerlach, J. Novák, G. Santoro, and F. Schreiber, Phys. Rev. B **90**, 205401 (2014): *Analysis of island shape evolution from diffuse x-ray scattering of organic thin films and implications for growth.*

[31] C. Frank, J. Novák, R. Banerjee, A. Gerlach, F. Schreiber, A. Vorobiev, and S. Kowarik, Phys. Rev. B **90**, 045410 (2014): *Island size evolution and molecular diffusion during growth of organic thin films followed by time-resolved specular and off-specular scattering.*

[32] R. Banerjee, J. Novák, C. Frank, C. Lorch, A. Hinderhofer, A. Gerlach, and F. Schreiber, Phys. Rev. Lett. **110**, 185506 (2013): *Evidence for Kinetically Limited Thickness Dependent Phase Separation in Organic Thin Film Blends.*

[33] C. Frank, J. Novák, A. Gerlach, G. Ligorio, K. Broch, A. Hinderhofer, A. Aufderheide, R. Banerjee, R. Nervo, and F. Schreiber, J. Appl. Phys. **114**, 043515 (2013): *Real-time X-ray scattering studies on temperature dependence of perfluoropentacene thin film growth.*

[34] A. Pimpinelli and J. Villain, *Physics of Crystal Growth* (1998).

[35] I. V. Markov, *Crystal growth for beginners* (2003).

[36] T. Michely and J. Krug, *Islands, Mounds and Atoms* (2004).

[37] F. Schreiber, Phys. Status Solidi A **201**, 1037 (2004): *Organic molecular beam deposition: Growth studies beyond the first monolayer.*

[38] J. W. Evans, P. A. Thiel, and M. C. Bartelt, Surf. Sci. Rep. **61**, 1 (2006): *Morphological evolution during epitaxial thin film growth: Formation of 2D islands and 3D mounds.*

[39] J. Krug, Physica A **313**, 47 (2002): *Four lectures on the physics of crystal growth.*

[40] G. Ehrlich and F. G. Hudda, J. Chem. Phys. **44**, 1039 (1966): *Atomic view of Surface Self-Diffusion: Tungsten on Tungsten.*

[41] R. L. Schwoebel and E. J. Shipsey, J. Appl. Phys. **37**, 3682 (1966): *Step Motion on Crystal Surfaces.*

[42] D. Walton, J. Chem. Phys. **37**, 2182 (1962): *Nucleation of Vapor Deposits.*

[43] J. A. Venables, Philos. Mag. **27**, 697 (1973): *Rate Equation Approaches to Thin Film Nucleation Kinetics.*

[44] J. Villain, J. Phys. I France **1**, 19 (1991): *Continuum models of crystal growth from atomic beams with and without desorption.*

[45] W. Warta, R. Stehle, and N. Karl, Appl. Phys. A Mater. **36**, 163 (1985): *Ultrapure, high mobility organic photoconductors.*

[46] S. Schiefer, M. Huth, A. Dobrinevski, and B. Nickel, J. Am. Chem. Soc. **129**, 10316 (2007): *Determination of the Crystal Structure of Substrate-Induced Pentacene Polymorphs in Fiber Structured Thin Films.*

[47] S. Pratontep, M. Brinkmann, F. Nüesch, and L. Zuppiroli, Synt. Met. **146**, 387 (2004): *Nucleation and growth of ultrathin pentacene films on silicon dioxide: effect of deposition rate and substrate temperature.*

[48] S. Kowarik, A. Gerlach, W. Leitenberger, J. Hu, G. Witte, C. Wöll, U. Pietsch, and F. Schreiber, Thin Solid Films **515**, 5606 (2007): *Energy-dispersive X-ray reflectivity and GID for real-time growth studies of pentacene thin films.*

[49] S. Kowarik, K. Broch, A. Hinderhofer, A. Schwartzberg, J. O. Ossó, D. Kilcoyne, F. Schreiber, and S. R. Leone, J. Phys. Chem. C **114**, 13061 (2010): *Crystal grain orientation in organic homo- and heteroepitaxy of pentacene and perfluoropentacene studied with X-ray spectromicroscopy.*

[50] S. Kowarik, Ph.D. thesis, Wadham College, Oxford, 2006.

[51] C. D. Dimitrakopoulos, A. R. Brown, and A. Pomp, J. Appl. Phys. **80**, 2501 (1996): *Molecular beam deposited thin films of pentacene for organic field effect transistor applications.*

[52] C. C. Mattheus, A. B. Dros, J. Baas, G. T. Oostergetel, A. Meetsma, J. L. de Boer, and T. T. M. Palstra, Synt. Met. **138**, 475 (2003): *Identification of polymorphs of pentacene.*

[53] I. P. M. Bouchoms, W. A. Schoonveld, J. Vrijmoeth, and T. M. Klapwijk, Synt. Met. **104**, 175 (1999): *Morphology identification of the thin film phases of vacuum evaporated pentacene on SIO_2 substrates.*

[54] A. Moser, J. Novák, H. G. Flesch, T. Djuric, O. Werzer, A. Haase, and R. Resel, Appl. Phys. Lett. **99**, 221911 (2011): *Temperature stability of the pentacene thin-film phase.*

[55] H. Yoshida, K. Inaba, and N. Sato, Appl. Phys. Lett. **90**, 181930 (2007): *X-ray diffraction reciprocal space mapping study of the thin film phase of pentacene.*

[56] G. Yoshikawa, T. Miyadera, R. Onoki, K. Ueno, I. Nakai, S. Entani, S. Ikeda, D. Guo, M. Kiguchi, H. Kondoh, T. Ohta, and K. Saiki, Surf. Sci. **600**, 2518 (2006): *In-situ measurement of molecular orientation of the pentacene ultrathin films grown on SiO_2 substrates.*

[57] A. C. Mayer, A. Kazimirov, and G. G. Malliaras, Phys. Rev. Lett. **97**, 105503 (2006): *Dynamics of Bimodal Growth in Pentacene Thin Films.*

[58] Y. Sakamoto, T. Suzuki, M. Kobayashi, Y. Gao, Y. Fukai, Y. Inoue, F. Sato, and S. Tokito, J. Am. Chem. Soc. **126**, 8138 (2004): *Perfluoropentacene: High-Performance p-n Junctions and Complementary Circuits with Pentacene.*

[59] B. M. Medina, D. Beljonne, H.-J. Egelhaaf, and J. Gierschner, J. Chem. Phys. **126**, 111101 (2007): *Effect of fluorination on the electronic structure and optical excitations of π-conjugated molecules.*

[60] A. Hinderhofer, A. Gerlach, S. Kowarik, F. Zontone, J. Krug, and F. Schreiber, Europhys. Lett. **91**, 56002 (2010): *Smoothing and coherent structure formation in organic-organic heterostructure growth.*

[61] I. Salzmann, S. Duhm, G. Heimel, J. P. Rabe, N. Koch, M. Oehzelt, Y. Sakamoto, and T. Suzuki, Langmuir **24**, 7294 (2008): *Structural Order in Perfluoropentacene Thin Films and Heterostructures with Pentacene.*

[62] J. P. Reinhardt, A. Hinderhofer, K. Broch, U. Heinemeyer, S. Kowarik, A. Vorobiev, A. Gerlach, and F. Schreiber, J. Phys. Chem. C **116**, 10917 (2012): *Structural and Optical Properties of Mixed Diindenoperylene-Perfluoropentacene Thin Films.*

[63] Y. Inoue, Y. Sakamoto, T. Suzuki, M. Kobayashi, Y. Gao, and S. Tokito, Jpn. J. Appl. Phys. **44**, 3663 (2005): *Organic Thin-Film Transistors with High Electron Mobility Based on Perfluoropentacene.*

[64] S. Kowarik, A. Gerlach, A. Hinderhofer, S. Milita, F. Borgatti, F. Zontone, T. Suzuki, F. Biscarini, and F. Schreiber, Phys. Status Solidi RRL **2**, 120 (2008): *Structure, morphology, and growth dynamics of perfluoro-pentacene thin films.*

[65] A. Dürr, B. Nickel, V. Sharma, U. Täffner, and H. Dosch, Thin Solid Films **503**, 127 (2006): *Observation of competing modes in the growth of diindenoperylene on* SiO_2.

[66] S. Kowarik, A. Gerlach, S. Sellner, L. Calvacanti, and F. Schreiber, Adv. Eng. Mater. **11**, 291 (2009): *Dewetting of an Organic Semiconductor Thin Film Observed in Real-time.*

[67] A. Hinderhofer, T. Hosokai, K. Yonezawa, A. Gerlach, K. Kato, K. Broch, C. Frank, J. Novák, S. Kera, N. Ueno, and F. Schreiber, Appl. Phys. Lett. **101**, 033307 (2012): *Post-growth surface smoothing of thin films of diindenoperylene.*

[68] A. C. Dürr, F. Schreiber, K. A. Ritley, V. Kruppa, J. Krug, H. Dosch, and B. Struth, Phys. Rev. Lett. **90**, 016104 (2003): *Rapid Roughening in Thin Film Growth of an Organic Semiconductor (Diindenoperylene).*

[69] A. C. Dürr, Ph.D. thesis, Universität Stuttgart, 2002.

[70] A. Opitz, J. Wagner, W. Brütting, I. Salzmann, N. Koch, J. Manara, J. Pflaum, A. Hinderhofer, and F. Schreiber, IEEE J. Sel. Top. Quant. Electron. **16**, 1707 (2010): *Charge Separation at Molecular Donor-Acceptor Interfaces: Correlation Between Morphology and Solar Cell Performance.*

[71] J. L. de Boer, S. van Smaalen, V. Petricek, M. Dusek, M. A. Verheijen, and G. Meijer, Chem. Phys. Lett. **219**, 469 (1994): *Hexagonal close-packed* C_{60}.

[72] P. A. Heiney, J. E. Fischer, A. R. McGhie, W. J. Romanow, A. M. Denenstein, J. P. McCauley Jr., A. B. Smith, and D. E. Cox, Phys. Rev. Lett. **66**, 2911 (1991): *Orientational ordering transition in solid* C_{60}.

[73] H. W. Kroto, J. R. Heath, S. C. O'Brien, R. F. Curl, and R. E. Smalley, Nature **318**, 162 (1985): C_{60}*: Buckminsterfullerene.*

[74] W. I. F. David, R. M. Ibberson, J. C. Matthewman, K. Prassides, T. J. S. Dennis, J. P. Hare, H. W. Kroto, R. Taylor, and D. R. M. Walton, Nature **353**, 147 (1991): *Crystal structure and bonding of ordered* C_{60}.

[75] L. Gross, F. Mohn, N. Moll, B. Schuler, A. Criado, E. Guitián, D. Peña, A. Gourdon, and G. Meyer, Science **337**, 1326 (2012): *Bond-Order Discrimination by Atomic Force Microscopy.*

[76] A. Hinderhofer, Ph.D. thesis, Eberhard Karls Universität Tübingen, 2011.

[77] M. Gruber, M. Rawolle, J. Wagner, D. Magerl, U. Hörmann, J. Perlich, S. V. Roth, A. Opitz, F. Schreiber, P. Müller-Buschbaum, and W. Brütting, Adv. Energy Mater. **3**, 1075 (2013): *Correlating Structure and Morphology to Device Performance of Molecular Organic Donor-Acceptor Photovoltaic Cells Based on Diindenoperylene (DIP) and* C_{60}.

[78] S. J. Kang, Y. Yi, C. Y. Kim, K. Cho, J. H. Seo, M. Noh, K. Jeong, K.-H. Yoo, and C. N. Whang, Appl. Phys. Lett. **87**, 233502 (2005): *Ambipolar organic thin-film transistors using* C_{60}*/pentacene structure: Characterization of electronic structure and device property.*

[79] A. Opitz, M. Bronner, and W. Brütting, J. Appl. Phys. **101**, 063709 (2007): *Ambipolar charge carrier transport in mixed organic layers of phthalocyanine and fullerene.*

[80] D. L. Dorset and M. P. McCourt, Acta Crystallogr. Sect. A **50**, 344 (1994): *Disorder and the molecular packing of* C_{60} *buckminsterfullerene a direct electron-crystallographic analysis.*

[81] K. A. Ritley, B. Krause, F. Schreiber, and H. Dosch, Rev. Sci. Instrum. **72**, 1453 (2001): *A portable ultrahigh vacuum organic molecular beam deposition system for in situ x-ray diffraction measurements.*

[82] J. Als-Nielsen and D. McMorrow, *Elements of Modern X-ray Physics* (2001).

[83] M. Born and E. Wolf, *Principles of Optics* (1993).

[84] L. G. Parratt, Phys. Rev. **95**, 359 (1954): *Surface Studies of Solids by Total Reflection of X-Rays.*

[85] G. Renaud, R. Lazzari, and F. Leroy, Surf. Sci. Rep. **64**, 255 (2009): *Probing surface and interface morphology with Grazing Incidence Small Angle X-Ray Scattering.*

[86] U. Pietsch, V. Holý, and T. Baumbach, *High-Resolution X-Ray Scattering* (2004).

[87] M. Birkholz, *Thin Film Analysis by X-Ray Scattering* (2006).

[88] S. Kowarik, A. Gerlach, M. W. A. Skoda, S. Sellner, and F. Schreiber, Eur. Phys. J. Spec. Top. **167**, 11 (2009): *Real-time studies of thin film growth: Measurement and analysis of X-ray growth oscillations beyond the anti-Bragg point.*

[89] P. I. Cohen, G. S. Petrich, P. R. Pukite, G. J. Whaley, and A. S. Arrott, Surf. Sci. **216**, 222 (1989): *Birth-death models of epitaxy: I. Diffraction oscillations from low index surfaces.*

[90] I. T. Koponen, Nucl. Instr. Meth. Phys. Res. B **171**, 314 (2000): *Modeling layer-by-layer growth in ion beam assisted deposition of thin films.*

[91] R. Kariotis and M. G. Lagally, Surf. Sci. **216**, 557 (1989): *Rate equation modelling of epitaxial growth.*

[92] V. I. Trofimov, V. G. Mokerov, and A. G. Shumyankov, Thin Solid Films **306**, 105 (1997): *Kinetic model for molecular beam epitaxial growth on a singular surface.*

[93] V. I. Trofimov and V. G. Mokerov, Comput. Mater. Sci. **17**, 510 (2000): *Homoepitaxial growth kinetics in the presence of a Schwoebel barrier.*

[94] V. I. Trofimov and V. G. Mokerov, Mater. Sci. Eng. B-Adv **89**, 420 (2002): *Epitaxial growth kinetics in the presence of an Ehrlich-Schwoebel barrier: comparative analysis of different models.*

[95] V. I. Trofimov, Thin Solid Films **428**, 56 (2003): *Morphology evolution in a growing film.*

[96] V. I. Trofimov, J. Kim, and S. Bae, Surf. Sci. **601**, 4465 (2007): *Influence of two different adatom mobilities on the initial heteroepitaxial growth kinetics.*

[97] J. Daillant and A. Gibaud, *X-Ray and Neutron Reflectivity* (2009).

[98] R. Lazzari, F. Leroy, and G. Renaud, Phys. Rev. B **76**, 125411 (2007): *Grazing-incidence small-angle x-ray scattering from dense packing of islands on surfaces: Development of distorted wave Born approximation and correlation between particle sizes and spacing.*

[99] R. Lazzari, J. Appl. Cryst. **35**, 406 (2002): *IsGISAXS: a program for grazing-incidence small-angle X-ray scattering analysis of supported islands.*

[100] P. Müller-Buschbaum, in *Applications of Synchrotron Light to Scattering and Diffraction in Materials and Life Sciences*, Vol. 776 of *Lecture Notes in Physics*, edited by M. A. Gomez, A. Nogales, M. C. Garcia-Gutierrez, and T. A. Ezquerra (2009).

[101] P. Willmott, *An Introduction to Synchrotron Radiation: Techniques and Applications* (2011).

[102] K. D. Jandt, Surf. Sci. **491**, 303 (2001): *Atomic force microscopy of biomaterials surfaces and interfaces.*

[103] G. Hlawacek and C. Teichert, J. Phys.: Condens. Matter **25**, 143202 (2013): *Nucleation and growth of thin films of rod-like conjugated molecules.*

[104] T. Breuer and G. Witte, Phys. Rev. B **83**, 155428 (2011): *Epitaxial growth of perfluoropentacene films with predefined molecular orientation: A route for single-crystal optical studies.*

[105] G. Binnig, C. F. Quate, and C. Gerber, Phys. Rev. Lett. **56**, 930 (1986): *Atomic force microscope.*

[106] D. Nečas and P. Klapetek, Cent. Eur. J. Phys. **10**, 181 (2012): *Gwyddion: an open-source software for SPM data analysis.*

[107] F. Yang, M. Shtein, and S. R. Forrest, Nat. Mater. **4**, 37 (2005): *Controlled growth of a molecular bulk heterojunction photovoltaic cell.*

[108] J. E. Anthony, A. Facchetti, M. Heeney, S. R. Marder, and X. Zhan, Adv. Mater. **22**, 3876 (2010): *n-Type Organic Semiconductors in Organic Electronics.*

[109] T. Breuer, M. A. Celik, P. Jakob, R. Tonner, and G. Witte, J. Phys. Chem. C **116**, 14491 (2012): *Vibrational Davydov Splittings and Collective Mode Polarizations in Oriented Organic Semiconductor Crystals.*

[110] L. Huang, D. Rocca, S. Baroni, K. E. Gubbins, and M. B. Nardelli, J. Chem. Phys. **130**, 194701 (2009): *Molecular design of photoactive acenes for organic photovoltaics.*

[111] N. G. Martinelli, Y. Olivier, S. Athanasopoulos, M.-C. R. Delgado, K. R. Pigg, D. A. da Silva Filho, R. S. Sánchez-Carrera, E. Venuti, R. G. D. Valle, J.-L. Brédas, D. Beljonne, and J. Cornil, ChemPhysChem 2265 (2009): *Influence of Intermolecular Vibrations on the Electronic Coupling in Organic Semiconductors: The Case of Anthracene and Perfluoropentacene.*

[112] I. Salzmann, S. Duhm, G. Heimel, M. Oehzelt, R. Kniprath, R. L. Johnson, J. P. Rabe, and N. Koch, J. Am. Chem. Soc. **130**, 12870 (2008): *Tuning the Ionization Energy of Organic Semiconductor Films: The Role of Intramolecular Polar Bonds.*

[113] J.-Z. Wang, J. T. Sadowski, Z.-H. Xiong, Y. Fujikawa, Q. K. Xue, and T. Sakurai, Nanotechnology **20**, 095704 (2009): *Comparative studies of pentacene and perfluoropentacene grown on a Bi(0001) surface.*

[114] F. Anger, J. O. Ossó, U. Heinemeyer, K. Broch, R. Scholz, A. Gerlach, and F. Schreiber, J. Chem. Phys. **136**, 054701 (2012): *Photoluminescence spectroscopy of pure pentacene, perfluoropentacene, and mixed thin films.*

[115] K. Broch, U. Heinemeyer, A. Hinderhofer, F. Anger, R. Scholz, A. Gerlach, and F. Schreiber, Phys. Rev. B **83**, 245307 (2011): *Optical evidence for intermolecular coupling in mixed films of pentacene and perfluoropentacene.*

[116] F. Babudri, G. M. Farinola, F. Naso, and R. Ragni, Chem. Commun. **10**, 1003 (2007): *Fluorinated organic materials for electronic and optoelectronic applications: the role of the fluorine atom.*

[117] S. Duhm, I. Salzmann, G. Heimel, M. Oehzelt, A. Haase, R. L. Johnson, J. P. Rabe, and N. Koch, Appl. Phys. Lett. **94**, 033304 (2009): *Controlling energy level offsets in organic/organic heterostructures using intramolecular polar bonds.*

[118] S. Duhm, S. Hosoumi, I. Salzmann, A. Gerlach, M. Oehzelt, B. Wedl, T.-L. Lee, F. Schreiber, N. Koch, N. Ueno, and S. Kera, Phys. Rev. B **81**, 045418 (2010): *Influence of intramolecular polar bonds on interface energetics in perfluoro-pentacene on Ag(111).*

[119] N. Koch, A. Vollmer, S. Duhm, Y. Sakamoto, and T. Suzuki, Adv. Mater. **19**, 112 (2007): *The Effect of Fluorination on Pentacene/Gold Interface Energetics and Charge Reorganization Energy.*

[120] S. L. Wong, H. Huang, Y. L. Huang, Y. Z. Wang, X. Y. Gao, T. Suzuki, W. Chen, and A. T. S. Wee, J. Phys. Chem. C **114**, 9356 (2010): *Effect of Fluorination on the Molecular Packing of Perfluoropentacene and Pentacene Ultrathin Films on Ag (111).*

[121] D. G. de Oteyza, Y. Wakayama, X. Liu, W. Yang, P. L. Cook, F. J. Himpsel, and J. E. Ortega, Chem. Phys. Lett. **490**, 54 (2010): *Effect of fluorination on the molecule-substrate interactions of pentacene/Cu (100) interfaces.*

[122] A. Hinderhofer, T. Hosokai, C. Frank, J. Novák, A. Gerlach, and F. Schreiber, J. Phys. Chem. C **115**, 16155 (2011): *Templating Effect for Organic Heterostructure Film Growth: Perfluoropentacene on Diindenoperylene.*

[123] A. Hinderhofer, U. Heinemeyer, A. Gerlach, S. Kowarik, R. M. J. Jacobs, Y. Sakamoto, T. Suzuki, and F. Schreiber, J. Chem. Phys. **127**, 194705 (2007): *Optical properties of pentacene and perfluoropentacene thin films.*

[124] M. C. R. Delgado, K. R. Pigg, D. A. da Silva Filho, N. E. Gruhn, Y. Sakamoto, T. Suzuki, R. M. Osuna, J. Casado, V. Hernández, J. T. L. Navarrete, N. G. Martinelli, J. Cornil, R. S. Sánchez-Carrera, V. Coropceanu, and J.-L. Brédas, J. Am. Chem. Soc. **131**, 1502 (2009): *Impact of Perfluorination on the Charge-Transport Parameters of Oligoacene Crystals.*

[125] T. V. Desai, A. R. Woll, F. Schreiber, and J. R. Engstrom, J. Phys. Chem. C **114**, 20120 (2010): *Nucleation and Growth of Perfluoropentacene on Self-Assembled Monolayers: Significant Changes in Island Density and Shape with Surface Termination.*

[126] J. Götzen, C. H. Schwalb, C. Schmidt, G. Mette, M. Marks, U. Höfer, and G. Witte, Langmuir **27**, 993 (2011): *Structural Evolution of Perfluoro-Pentacene Films on Ag(111): Transition from 2D to 3D Growth.*

[127] K. Fujii, C. Himcinschi, M. Toader, S. Kera, D. R. T. Zahn, and N. Ueno, J. Electron. Spectrosc. Relat. Phenom. **174**, 65 (2009): *Vibrational properties of perfluoropentacene thin film.*

[128] T. Breuer, I. Salzmann, J. Götzen, M. Oehzelt, A. Morherr, N. Koch, and G. Witte, Cryst. Growth Des. **11**, 4996 (2011): *Interrelation between Substrate Roughness and Thin-Film Structure of Functionalized Acenes on Graphite.*

[129] B. Krause, F. Schreiber, H. Dosch, A. Pimpinelli, and O. H. Seeck, Europhys. Lett. **65**, 372 (2004): *Temperature dependence of the 2D-3D transition in the growth of PTCDA on Ag(111): A real-time X-ray and kinetic Monte Carlo study.*

[130] A. K. Tripathi and J. Pflaum, Appl. Phys. Lett. **89**, 082103 (2006): *Correlation between ambipolar transport and structural phase transition in diindenoperylene single crystals.*

[131] U. Heinemeyer, K. Broch, A. Hinderhofer, M. Kytka, R. Scholz, A. Gerlach, and F. Schreiber, Phys. Rev. Lett. **104**, 257401 (2010): *Real-Time Changes in the Optical Spectrum of Organic Semiconducting Films and Their Thickness Regimes during Growth.*

[132] F. Liscio, C. Albonetti, K. Broch, A. Shehu, S. D. Quiroga, L. Ferlauto, C. Frank, S. Kowarik, R. Nervo, A. Gerlach, S. Milita, F. Schreiber, and F. Biscarini, ACS Nano **7**, 1257 (2013): *Molecular Reorganization in Organic Field-Effect Transistors and Its Effect on Two-Dimensional Charge Transport Pathways.*

[133] R. Ruiz, A. C. Mayer, G. G. Malliaras, B. Nickel, G. Scoles, A. Kazimirov, H. Kim, R. L. Headrick, and Z. Islam, Appl. Phys. Lett. **85**, 4926 (2004): *Structure of pentacene thin films.*

[134] B. Krause, A. C. Dürr, K. Ritley, F. Schreiber, H. Dosch, and D. Smilgies, Phys. Rev. B **66**, 235404 (2002): *Structure and growth morphology of an archetypal system for organic epitaxy: PTCDA on Ag(111).*

[135] P. Fenter, F. Schreiber, L. Zhou, P. Eisenberger, and S. R. Forrest, Phys. Rev. B **56**, 3046 (1997): *In situ studies of morphology, strain, and growth modes of a molecular organic thin film.*

[136] L. Kilian, E. Umbach, and M. Sokolowski, Surf. Sci. **573**, 359 (2004): *Molecular beam epitaxy of organic films investigated by high resolution low energy electron diffraction (SPA-LEED): 3,4,9,10-perylenetetracarboxylicacid-dianhydride (PTCDA) on Ag(111).*

[137] K. O. Lee and T. T. Gan, Chem. Phys. Lett. **51**, 120 (1977): *Influence of substrate temperature on the optical properties of evaporated films of pentacene.*

[138] K. N. Baker, A. V. Fratini, T. Resch, H. C. Knachel, W. W. Adams, E. P. Socci, and B. L. Farmer, Polymer **34**, 1571 (1993): *Crystal structures, phase transitions and energy calculations of poly(p-phenylene) oligomers.*

[139] M. Fendrich and J. Krug, Phys. Rev. B **76**, 121302 (2007): *Ehrlich-Schwoebel effect for organic molecules: Direct calculation of the step-edge barrier using empirical potentials.*

[140] S. K. Sinha, M. K. Sanyal, S. K. Satija, C. F. Majkrzak, D. A. Neumann, H. Homma, S. Szpala, A. Gibaud, and H. Morkoc, Physica B **198**, 72 (1994): *X-ray scattering studies of surface roughness of GaAs/A1As multilayers*.

[141] S. K. Sinha, Y. P. Feng, C. A. Melendres, D. D. Lee, T. P. Russell, S. K. Satija, E. B. Sirota, and M. K. Sanyal, Physica A **231**, 99 (1996): *Off-specular X-ray scattering studies of the morphology of thin films*.

[142] P. S. Pershan, Colloid Surface A **171**, 149 (2000): *Effects of thermal roughness on X-ray studies of liquid surfaces*.

[143] B. Nickel, R. Barabash, R. Ruiz, N. Koch, A. Kahn, L. C. Feldman, R. F. Haglund, and G. Scoles, Phys. Rev. B **70**, 125401 (2004): *Dislocation arrangements in pentacene thin films*.

[144] S. K. Sinha, E. B. Sirota, S. Garoff, and H. B. Stanley, Phys. Rev. B **38**, 2297 (1988): *X-ray and neutron scattering from rough surfaces*.

[145] M. Tolan, *X-Ray Scattering from Soft-Matter Thin Films*, *Springer tracts in modern physics* (1999).

[146] T. Salditt, T. H. Metzger, and J. Peisl, Phys. Rev. Lett. **73**, 2228 (1994): *Kinetic Roughness of Amorphous Multilayers Studied by Diffuse X-Ray Scattering*.

[147] A. Fleet, D. Dale, A. R. Woll, Y. Suzuki, and J. D. Brock, Phys. Rev. Lett. **96**, 055508 (2006): *Multiple Time Scales in Diffraction Measurements of Diffusive Surface Relaxation*.

[148] S. Yu, G. Santoro, K. Sarkar, B. Dicke, P. Wessels, S. Bommel, R. Döhrmann, J. Perlich, M. Kuhlmann, E. Metwalli, J. F. H. Risch, M. Schwartzkopf, M. Drescher, P. Müller-Buschbaum, and S. V. Roth, J. Phys. Chem. Lett. **4**, 3170 (2013): *Formation of Al Nanostructures on Alq3: An in Situ Grazing Incidence Small Angle X-ray Scattering Study during Radio Frequency Sputter Deposition*.

[149] G. Santoro, S. Yu, M. Schwartzkopf, P. Zhang, S. K. Vayalil, J. F. H. Risch, M. A. Rübhausen, M. Hernández, C. Domingo, and S. V. Roth, Appl. Phys. Lett. **104**, 243107 (2014): *Silver substrates for surface enhanced Raman scattering: Correlation between nanostructure and Raman scattering enhancement*.

[150] D.-M. Smilgies, P. Busch, C. M. Papadakis, and D. Posselt, Synchrotron Radiation News **15**, 35 (2002): *Characterization of Polymer Thin Films with Small-Angle X-ray Scattering under Grazing Incidence (GISAXS)*.

[151] T. H. Metzger, I. Kegel, R. Paniago, and J. Peisl, J. Phys. D: Appl. Phys. **32**, A202 (1999): *Grazing incidence x-ray scattering: an ideal tool to study the structure of quantum dots*.

[152] P. Du, M. Li, K. Douki, X. Li, C. B. W. Garcia, A. Jain, D.-M. Smilgies, L. J. Fetters, S. M. Gruner, U. Wiesner, and C. K. Ober, Adv. Mater. **16**, 953 (2004): *Additive-Driven Phase-Selective Chemistry in Block Copolymer Thin Films: The Convergence of Top-Down and Bottom-Up Approaches.*

[153] J. Stangl, V. Holý, P. Mikulík, G. Bauer, I. Kegel, T. H. Metzger, O. G. Schmidt, C. Lange, and K. Eberl, Appl. Phys. Lett. **74**, 3785 (1999): *Self-assembled carbon-induced germanium quantum dots studied by grazing-incidence small-angle x-ray scattering.*

[154] D. Kurrle and J. Pflaum, Appl. Phys. Lett. **92**, 133306 (2008): *Exciton diffusion length in the organic semiconductor diindenoperylene.*

[155] D. G. de Oteyza, J. M. García-Lastra, M. Corso, B. P. Doyle, L. Floreano, A. Morgante, Y. Wakayama, A. Rubio, and J. E. Ortega, Adv. Funct. Mater. **19**, 3567 (2009): *Customized Electronic Coupling in Self-Assembled Donor-Acceptor Nanostructures.*

[156] D. G. de Oteyza, T. N. Krauss, E. Barrena, S. Sellner, H. Dosch, and J. O. Ossó, Appl. Phys. Lett. **90**, 243104 (2007): *Towards controlled bottom-up architectures in organic heterostructures.*

[157] X. Zhang, E. Barrena, D. Goswami, D. G. de Oteyza, C. Weis, and H. Dosch, Phys. Rev. Lett. **103**, 136101 (2009): *Evidence for a Layer-Dependent Ehrlich-Schwöbel Barrier in Organic Thin Film Growth.*

[158] S. Kowarik, A. Gerlach, S. Sellner, F. Schreiber, L. Cavalcanti, and O. Konovalov, Phys. Rev. Lett. **96**, 125504 (2006): *Real-Time Observation of Structural and Orientational Transitions during Growth of Organic Thin Films.*

[159] A. C. Dürr, F. Schreiber, M. Münch, N. Karl, B. Krause, V. Kruppa, and H. Dosch, Appl. Phys. Lett. **81**, 2276 (2002): *High structural order in thin films of the organic semiconductor diindenoperylene.*

[160] C. Revenant, F. Leroy, R. Lazzari, G. Renaud, and C. R. . Henry, Phys. Rev. B **69**, 035411 (2004): *Quantitative analysis of grazing incidence small-angle x-ray scattering: Pd/MgO (001) growth.*

[161] S. V. Roth, G. Herzog, V. Körstgens, A. Buffet, M. Schwartzkopf, J. Perlich, M. M. Abul Kashem, R. Döhrmann, R. Gehrke, A. Rothkirch, K. Stassig, W. Wurth, G. Benecke, C. Li, P. Fratzl, M. Rawolle, and P. Müller-Buschbaum, J. Phys.: Condens. Matter **23**, 254208 (2011): *In situ observation of cluster formation during nanoparticle solution casting on a colloidal film.*

[162] A. Buffet, A. Rothkirch, R. Döhrmann, V. Körstgens, M. M. Abul Kashem, J. Perlich, G. Herzog, M. Schwartzkopf, R. Gehrke, P. Müller-Buschbaum, and S. V. Roth, J. Synchrotron Rad. **19**, 647 (2012): *P03, the microfocus and nanofocus X-ray scattering (MiNaXS) beamline of the PETRA III storage ring: the microfocus endstation.*

[163] G. Santoro, A. Buffet, R. Döhrmann, S. Yu, V. Körstgens, P. Müller-Buschbaum, U. Gedde, M. Hedenqvist, and S. V. Roth, Rev. Sci. Instrum. **85**, 043901 (2014): *Use of intermediate focus for grazing incidence small and wide angle x-ray scattering experiments at the beamline P03 of PETRA III, DESY.*

[164] D. Babonneau, J. Appl. Cryst. **43**, 929 (2010): *FitGISAXS: software package for modelling and analysis of GISAXS data using IGOR Pro.*

[165] D. R. Lee, Y. S. Chu, Y. Choi, J. C. Lang, G. Srajer, S. K. Sinha, V. Metlushko, and B. Ilic, Appl. Phys. Lett. **82**, 982 (2003): *Characterization of the nanostructures of a lithographically patterned dot array by x-ray pseudo-Kossel lines.*

[166] J. K. Basu and M. K. Sanyal, Phys. Rep. **363**, 1 (2002): *Ordering and growth of Langmuir-Blodgett films: X-ray scattering studies.*

[167] J.-P. Hansen and I. R. McDonald, *Theory of Simple Liquids* (2006).

[168] A. Guinier, *X-Ray Diffraction* (1994).

[169] C. E. Shannon, Bell Syst. Tech. J. **27**, 379 (1948): *A Mathematical Theory of Communication.*

[170] A. J. S. Hamilton, Mon. Not. R. Astron. Soc. **312**, 257 (2000): *Uncorrelated modes of the non-linear power spectrum.*

[171] V. Boţan, F. Pesth, T. Schilling, and M. Oettel, Phys. Rev. E **79**, 061402 (2009): *Hard-sphere fluids in annular wedges: Density distributions and depletion potentials.*

[172] MATLAB, *version 8.0.0.783 (R2012b)* (2012).

[173] Mfit, *version 4.3.3* (2005).

[174] J. A. Nelder and R. Mead, Comput. J. **7**, 308 (1965): *A simplex method for function minimization.*

[175] G. Hlawacek, P. Puschnig, P. Frank, A. Winkler, C. Ambrosch-Draxl, and C. Teichert, Science **321**, 108 (2008): *Characterization of Step-Edge Barriers in Organic Thin-Film Growth.*

[176] J. E. Goose, E. L. First, and P. Clancy, Phys. Rev. B **81**, 205310 (2010): *Nature of step-edge barriers for small organic molecules.*

[177] S. Kowarik, A. Gerlach, and F. Schreiber, J. Phys.: Condens. Matter **20**, 184005 (2008): *Organic molecular beam deposition: fundamentals, growth dynamics, and in situ studies.*

[178] S. Hong, A. Amassian, A. R. Woll, S. Bhargava, J. D. Ferguson, G. G. Malliaras, J. D. Brock, and J. R. Engstrom, Appl. Phys. Lett. **92**, 253304 (2008): *Real time monitoring of pentacene growth on SiO_2 from a supersonic source.*

[179] R. Ruiz, B. Nickel, N. Koch, L. C. Feldman, R. F. Haglund, A. Kahn, F. Family, and G. Scoles, Phys. Rev. Lett. **91**, 136102 (2003): *Dynamic Scaling, Island Size Distribution, and Morphology in the Aggregation Regime of Submonolayer Pentacene Films.*

[180] J. D. Ferguson, G. Arikan, D. S. Dale, A. R. Woll, and J. D. Brock, Phys. Rev. Lett. **103**, 256103 (2009): *Measurements of Surface Diffusivity and Coarsening during Pulsed Laser Deposition.*

[181] A. Amassian, T. V. Desai, S. Kowarik, S. Hong, A. R. Woll, G. G. Malliaras, F. Schreiber, and J. R. Engstrom, J. Chem. Phys. **130**, 124701 (2009): *Coverage dependent adsorption dynamics in hyperthermal organic thin film growth.*

[182] Y. L. Huang, W. Chen, H. Huang, D. C. Qi, S. Chen, X. Y. Gao, J. Pflaum, and A. T. S. Wee, J. Phys. Chem. C **113**, 9251 (2009): *Ultrathin Films of Diindenoperylene on Graphite and SiO_2.*

[183] V. I. Trofimov and V. G. Mokerov, Thin Solid Films **428**, 66 (2003): *Rate equations model for layer epitaxial growth kinetics.*

[184] X. N. Zhang, E. Barrena, D. G. de Oteyza, and H. Dosch, Surf. Sci. **601**, 2420 (2007): *Transition from layer-by-layer to rapid roughening in the growth of DIP on SiO_2.*

[185] J. Krug, EPJ B **18**, 713 (2000): *Scaling regimes for second layer nucleation.*

[186] J. Krug, P. Politi, and T. Michely, Phys. Rev. B **61**, 14037 (2000): *Island nucleation in the presence of step-edge barriers: Theory and applications.*

[187] T. R. Linderoth, S. Horch, L. Petersen, S. Helveg, M. Schønning, E. Lægsgaard, I. Stensgaard, and F. Besenbacher, Phys. Rev. B **61**, R2448 (2000): *Energetics and dynamics of Pt dimers on Pt(110)-(1x2).*

[188] P. J. Feibelman, Phys. Rev. B **61**, R2452 (2000): *Ordering of self-diffusion barrier energies on Pt(110)-(1x2).*

[189] W. R. Salaneck, K. Seki, A. Kahn, and J.-J. Pireaux, *Conjugated Polymer and Molecular Interfaces* (2001).

[190] S. R. Forrest, Chem. Rev. **97**, 1793 (1997): *Ultrathin Organic Films Grown by Organic Molecular Beam Deposition and Related Techniques.*

[191] C. Deibel and V. Dyakonov, Rep. Prog. Phys. **73**, 096401 (2010): *Polymer-fullerene bulk heterojunction solar cells.*

[192] G. Dennler, M. C. Scharber, and C. J. Brabec, Adv. Mater. **21**, 1323 (2009): *Polymer-Fullerene Bulk-Heterojunction Solar Cells.*

[193] P. Peumans, A. Yakimov, and S. R. Forrest, J. Appl. Phys. **93**, 3693 (2003): *Small molecular weight organic thin-film photodetectors and solar cells.*

[194] C. Schünemann, D. Wynands, L. Wilde, M. P. Hein, S. Pfützner, C. Elschner, K.-J. Eichhorn, K. Leo, and M. Riede, Phys. Rev. B **85**, 245314 (2012): *Phase separation analysis of bulk heterojunctions in small-molecule organic solar cells using zinc-phthalocyanine and* C_{60}.

[195] H. J. Kim, J. W. Kim, H. H. Lee, B. Lee, and J.-J. Kim, Adv. Funct. Mater. **22**, 4244 (2012): *Initial Growth Mode, Nanostructure, and Molecular Stacking of a ZnPc:C60 Bulk Heterojunction.*

[196] C. W. Tang, Appl. Phys. Lett. **48**, 183 (1986): *Two-layer organic photovoltaic cell.*

[197] M. Zhang, H. Wang, H. Tian, Y. Geng, and C. W. Tang, Adv. Mater. **23**, 4960 (2011): *Bulk Heterojunction Photovoltaic Cells with Low Donor Concentration.*

[198] H. Dosch, *Critical Phenomena at Surfaces and Interfaces* (1992).

[199] A. I. Kitaigorodsky, *Mixed Crystals* (1984).

[200] A. Hinderhofer, A. Gerlach, K. Broch, T. Hosokai, K. Yonezawa, K. Kato, S. Kera, N. Ueno, and F. Schreiber, J. Phys. Chem. C **117**, 1053 (2013): *Geometric and Electronic Structure of Templated* C_{60} *on Diindenoperylene Thin Films.*

[201] S. Bommel, N. Kleppmann, C. Weber, H. Spranger, P. Schäfer, J. Novák, S. V. Roth, F. Schreiber, S. H. L. Klapp, and S. Kowarik, Nat. Commun. **submitted**, : *Unravelling the multilayer growth of the fullerene* C_{60} *in real-time.*

[202] P. Wochner, C. Gutt, T. Autenrieth, T. Demmer, V. Bugaev, A. D. Ortiz, A. Duri, F. Zontone, G. Grübel, and H. Dosch, PNAS **106**, 11511 (2009): *X-ray cross correlation analysis uncovers hidden local symmetries in disordered matter.*

[203] R. P. Kurta, L. Grodd, E. Mikayelyan, O. Y. Gorobtsov, I. Fratoddi, I. Venditti, M. Sprung, S. Grigorian, and I. A. Vartanyants, J. Phys.: Conf. Ser. **499**, 012021 (2014): *Structural properties of* π-π *conjugated network in polymer thin films studied by x-ray cross-correlation analysis.*

[204] A. Yamamoto, Acta Crystallogr. **A52**, 509 (1996): *Crystallography of quasiperiodic crystals.*

[205] M. Klopotek, Diploma thesis, Eberhard Karls Universiät Tübingen, in prep.

[206] I. N. Bronstein, K. A. Semendjajew, G. Musiol, and H. Mühlig, *Taschenbuch der Mathematik* (2008).

LIST OF PUBLICATIONS

- C. Frank, R. Banerjee, M. Oettel, A. Gerlach, J. Novák, G. Santoro, and F. Schreiber, Phys. Rev. B, **90**, 205401 (2014): *Analysis of island shape evolution from diffuse x-ray scattering of organic thin films and implications for growth.*

- C. Frank, J. Novák, R. Banerjee, A. Gerlach, F. Schreiber, A. Vorobiev, and S. Kowarik, Phys. Rev. B **90**, 045410 (2014): *Island size evolution and molecular diffusion during growth of organic thin films followed by time-resolved specular and off-specular scattering.*

- K. Vasseur, K. Broch, A. L. Ayzner, B. P. Rand, D. Cheyns, C. Frank, F. Schreiber, M. F. Toney, L. Froyen, and P. Heremans, ACS Appl. Mater. Interfaces **5**, 8505 (2013): *Controlling the Texture and Crystallinity of Evaporated Lead Phthalocyanine Thin Films for Near-Infrared Sensitive Solar Cells.*

- C. Frank, J. Novák, A. Gerlach, G. Ligorio, K. Broch, A. Hinderhofer, A. Aufderheide, R. Banerjee, R. Nervo, and F. Schreiber, J. Appl. Phys. **114**, 043515 (2013): *Real-time X-ray scattering studies on temperature dependence of perfluoropentacene thin film growth.*

- R. Banerjee, J. Novák, C. Frank, C. Lorch, A. Hinderhofer, A. Gerlach, and F. Schreiber, Phys. Rev. Lett. **110**, 185506 (2013): *Evidence for Kinetically Limited Thickness Dependent Phase Separation in Organic Thin Film Blends.*

- F. Liscio, C. Albonetti, K. Broch, A. Shehu, S. D. Quiroga, L. Ferlauto, C. Frank, S. Kowarik, R. Nervo, A. Gerlach, S. Milita, F. Schreiber, and F. Biscarini, ACS Nano **7**, 1257 (2013): *Molecular Reorganization in Organic Field-Effect Transistors and Its Effect on Two-Dimensional Charge Transport Pathways.*

- A. Hinderhofer, T. Hosokai, K. Yonezawa, A. Gerlach, K. Kato, K. Broch, C. Frank, J. Novák, S. Kera, N. Ueno, and F. Schreiber, Appl. Phys. Lett. **101**, 033307 (2012): *Post-growth surface smoothing of thin films of diindenoperylene.*

- C. Weber, C. Frank, S. Bommel, T. Rukat, W. Leitenberger, P. Schäfer, F. Schreiber, and S. Kowarik, J. Chem. Phys. **136**, 204709 (2012): *Chain-length dependent growth dynamics of n-alkanes on silica investigated by energy-dispersive x-ray reflectivity in situ and in real-time.*

- A. Hinderhofer, T. Hosokai, C. Frank, J. Novák, A. Gerlach, and F. Schreiber, J. Phys. Chem. C **115**, 16155 (2011): *Templating Effect for Organic Heterostructure Film Growth: Perfluoropentacene on Diindenoperylene.*

- A. Hinderhofer, C. Frank, T. Hosokai, A. Resta, A. Gerlach, and F. Schreiber, J. Chem. Phys **134**, 104702 (2011): *Structure and morphology of coevaporated pentacene-perfluoropentacene thin films.*

- T. Hosokai, A. Gerlach, A. Hinderhofer, C. Frank, G. Ligorio, U. Heinemeyer, A. Vorobiev, and F. Schreiber, Appl. Phys. Lett. **97**, 063301 (2010): *Simultaneous in situ measurements of X-ray reflectivity and optical spectroscopy during organic semiconductor thin film growth.*

DANKSAGUNG

Ich möchte mich vorrangig und in erster Linie bei meinem Doktorvater Prof. Dr. Frank Schreiber bedanken. Zum einen gilt dies der Ermöglichung meiner Promotion, zum anderen aber auch einer exzellenten Betreuung sowie den zahlreichen wissenschaftlichen Diskussionen und Anregungen, von denen ich in den letzten Jahren profitieren und lernen durfte.

Prof. Dr. Martin Oettel danke ich ebenfalls für die engagierte Hilfe bei vielen wissenschaftlichen Problemen und Fragestellungen sowie für die Bereitschaft diese Dissertation als Zweitgutachter zu bewerten.

Meinen speziellen Dank möchte ich an dieser Stelle an Dr. Rupak Banerjee und Dr. Alexander Gerlach richten, und besonders auf die gute Zusammenarbeit bei der Vorbereitung und Durchführung der verschiedenen Strahlzeitexperimente, und damit verbunden, die vielen guten Ratschläge, zahlreichen anregenden und interessanten Diskussionen sowie auf die allgemein sehr produktive und kameradschaftliche Teamarbeit während der vergangenen Jahre verweisen.

Dr. Jiri Novák und Prof. Dr. Stefan Kowarik danke ich für die Unterstützung bei Synchrotronexperimenten und ihrer wissenschaftlichen Expertise, welche ebenfalls einen erheblichen Anteil am Gelingen dieser Arbeit hatten.

Ergänzend möchte ich mich bei Christopher Lorch, Dr. Jaita Banerjee, Christopher Weber, Sebastian Bommel, Dr. Alexander Hinderhofer, Karolien Vasseur, Dr. Fabiola Liscio und Dr. Takuya Hosokai für eine erfolgreiche Kollaboration, Unterstützung bei Experimenten und einer Vielzahl an interessanten wissenschaftlichen Debatten bedanken.

Für das Korrekturlesen dieser Arbeit danke ich zusätzlich Dr. Alexander Gerlach, Dr. Rupak Banerjee, Dr. Jiri Novák, Miriam Klopotek und Heiko Frank.

Dem Personal an den verschiedenen Synchrotroneinrichtungen danke ich für die erstklassige Betreuung und die kompetente Unterstützung bei unseren Experimenten. Insbesondere betrifft dies Dr. Alexei Vorobiev, Dr. Roberto Nervo, Dr. Oleg Konovalov, Dr. Jakub Drnec und Dr. Roberto Felici an der European Synchrotron Radiation Facility (ESRF), Dr. Gonzalo Santoro und Dr. Stefan V. Roth an dem Deutschen Elektronen Synchrotron (DESY) sowie Dr. Steven Leak und Prof. Dr. Philip Willmott an der Swiss Light Source (SLS).

Für die Unterstützung und Beratung in vielen technischen Angelegenheiten möchte ich mich bei Bernd Hofferberth und Klaus Hagdorn-Wittern bedanken.

Den Sekretärinnen Aleksandra Rötschke, Hanna Maurer und Sabine Ehrlich gilt mein Dank besonders für die kompetente Hilfe in vielen bürokratischen und organisatorischen Angelegenheiten.

Insgesamt danke ich ausnahmslos der ganzen Arbeitsgruppe von Prof. Schreiber für eine harmonische Arbeitsatmosphäre und gute Zusammenarbeit.

Zu guter Letzt möchte ich mich bei meinen Eltern, meinen beiden Geschwistern und meiner Verlobten für den mir entgegengebrachten moralischen Rückhalt und die wunderbare und sehr inspirierende Zeit bedanken, die ich mit ihnen bisher verbringen durfte.